Community Ocean Vertical Mixing (CVMix) Parameterizations: theory and numerics
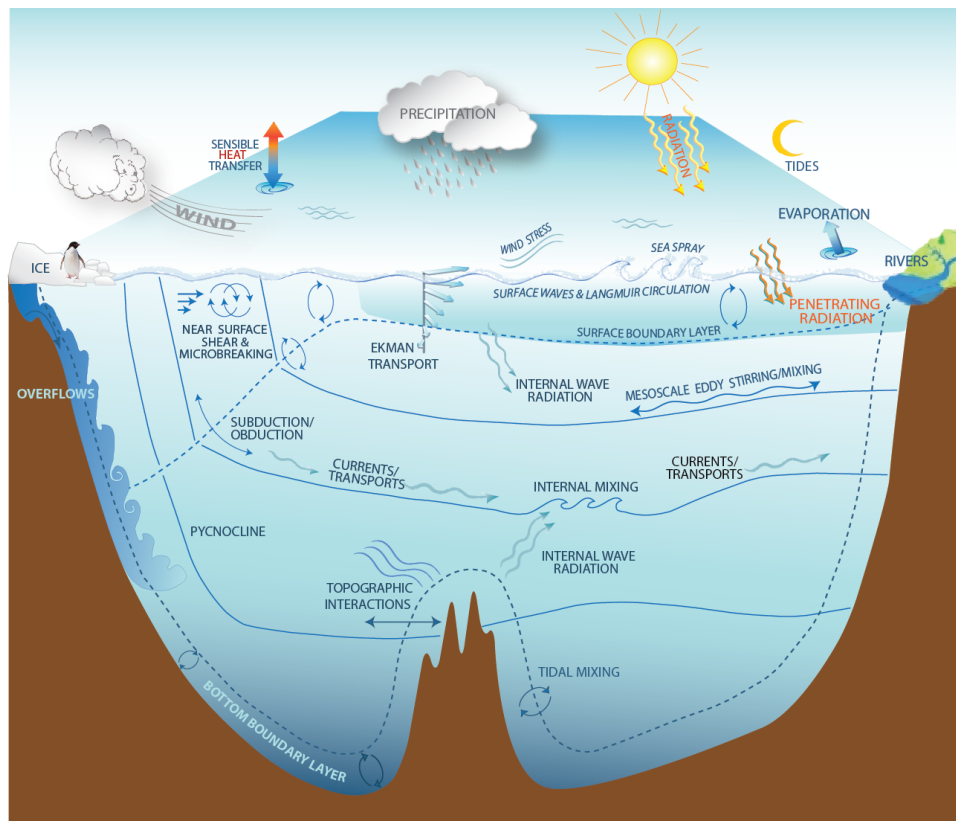
Stephen Griffies, Alistair Adcroft, Robert Hallberg
NOAA/GFDL
Princeton, USA

Gokhan Danabasoglu, William Large, Michael Levy
NCAR
Boulder, USA

Doug Jacobsen, Phil Jones, Mark Peterson, Todd Ringler
LANL
Los Alamos, USA

Many others...as the project evolves

Draft from January 21, 2013

The CVMix Parameterizations Project

Community Ocean Vertical Mixing (CVMix) Parameterizations is a software package that aims to provide transparent, robust, flexible, well documented, shared Fortran source code for use in parameterizing vertical mixing processes in numerical ocean models. The project is focused on developing software for a consensus of first-order closures that return a vertical diffusivity, viscosity, and possibly a non-local transport, with each quantity dependent on the tracer or velocity being mixed. CVMix modules are written as kernals designed for use in a variety of Fortran ocean model codes such as MPAS-ocean, MOM, and POP. CVMix modules use MKS units and expect the same for input and output. Code development occurs within a community of scientists and engineers who make use of CVMix modules for a variety of ocean codes. When mature, CVMix modules will be freely distributed to the open source community under GPLv2 using an open source methodology.

As of January 2013, the CVMix project remains in a very early stage, with most of the algorithms listed in this document uncoded. Hence, this document largely summarizes aspirations of its authors, and it serves to help develop software design documents.

This document is freely distributed and should be referenced as the following.

Community Ocean Vertical Mixing (CVMix) Parameterizations
Many authors...
75 + v pages

Information about how to download the source code can be found at...

This document was prepared using LaTeX as described by Lamport (1994) and Goosens et al. (1994).

Contents

Contents

List of Figures

Chapter 1

CVMix Parameterizations

Contents

We provide here an overview to the various parameterized vertical mixing schemes available with Community Ocean Vertical Mixing (CVMix) Parameterizations.

1.1   Vertical mixing parameterizations in CVMix

The CVMix Project aims to address the needs of various ocean modeling groups to code, test, tune, and document parameterizations of oceanic vertical mixing for numerical ocean simulations. The project focuses on first-order turbulence closures for vertical mixing processes.[1] CVMix does *not* determine time stepping for the model prognostic fields. Instead, time stepping is the responsibility of the calling model code. The following schemes are targets for the CVMix parameterizations during phase I of the development.

- STATIC BACKGROUND MIXING (Chapter 3): Certain turbulent processes, in particular the ambient background gravity wave "noise", constitute a background level of mixing that is largely steady in time from the pespective of large-scaling ocean modeling. Though assumed to be time independent, these processes generally have a nontrivial space dependence. CVMix provides options for various of these time independent schemes:

  - the vertical profile from Bryan and Lewis (1979);
  - the profile from Henyey et al. (1986) in which mixing near the equator is very small, as measured by Gregg et al. (2003);
  - the approaches from Jochum (2009), in which enhanced mixing from parametric subharmonic mixing is included.

- SHEAR INDUCED MIXING (Chapter 4): The following schemes are available for shear mixing:

  - Pacanowski and Philander (1981), applicable largely for tropical circulation;
  - Large et al. (1994) and Large and Gent (1999), which builds on the Pacanowski and Philander (1981) scheme;

---

[1]Those interested in higher order turbulence closure schemes for oceanm odeling may find the General Ocean Turbulence Model (GOTM) from Umlauf et al. (2005) to be suitable.

- Jackson et al. (2008), which employs a vertically non-local method to determine shear mixing throughout the World Ocean.

- TIDALLY INDUCED MIXING (Chapter 5): The following schemes are available for parameterizing mixing induced by ocean tides.

  - Simmons et al. (2004)
  - Melet et al. (2013)
  - the bottom boundary mixing scheme from Legg et al. (2006), including bottom mixing from barotropic tides.

- DOUBLE DIFFUSIVE PROCESSES (Chapter 6): Double diffusive processes arise from the distinct mixing properties of temperature and salinity.

- KPP SURFACE BOUNDARY LAYER (Chapter 7): The K-profile parameterization (KPP) scheme from Large et al. (1994) provides for a diffusivity as well as a non-local transport, each within the surface planetary boundary layer.

- VERTICAL CONVECTIVE MIXING: Vertical profiles can become gravitationally unstable, such as when the ocean is forced with a negative buoyancy flux. Older approaches such as Cox (1984) and Rahmstorf (1993) considered a convective *adjustment* algorithm, in which vertical pairs of grid cells were adjusted towards a profile of static stability. In effect, the vertical diffusivity is infinite when using adjustment schemes. CVMix does *not* provide options for convective adjustment. Instead, CVMix allows for the specification of a diffusivity that is large in regions of gravitational instability, thus enabling vertical convective *mixing* rather than *adjustment*. Notably, when using the KPP surface boundary layer scheme, convective mixing is *not* computed inside the KPP boundary layer. Instead, it is only computed beneath the boundary layer, and it is done so *after* the KPP boundary layer matching has occurred (see Section 1.3).

1.2 The general form of CVMix parameterizations

All schemes considered in CVMix can be formulated in terms of a diffusivity and a non-local transport. That is, the vertical turbulent flux of a scalar or velocity component is written in the form

$$\overline{w'\lambda'} = -K_\lambda \left(\frac{\partial \overline{\lambda}}{\partial z} - \gamma_\lambda \right), \tag{1.1}$$

where w' is the turbulent or fluctuating portion of the vertical velocity component

$$w = w' + \overline{w}, \tag{1.2}$$

λ' is a turbulent scalar or velocity component, and the overline denotes an Eulerian ensemble or time average that separates the mean flow from the turbulent flow.[2] The first term on the right hand side of equation (1.1) provides for the familiar downgradient vertical diffusion determined by a non-negative vertical diffusivity, $K_\lambda \geq 0$, and the local vertical derivative of the model's resolved mean field, $\partial \overline{\lambda}/\partial z$. This term is referred to as the local portion of the vertical mixing parameterization

$$\overline{w'\lambda'}^{\text{local}} = -K_\lambda \left(\frac{\partial \overline{\lambda}}{\partial z} \right). \tag{1.3}$$

Note that the term "local" is used for this portion of the parameterized flux (1.1) since it is determined by the local derivative of the mean field, $\overline{\lambda}$. However, the diffusivity can generally be determined as a non-local function of boundary layer properties, with such being the case for the KPP scheme (Chapter 7). The

---

[2]In Chapter 7, we follow the notation of Large et al. (1994) by writing the mean quantities with an uppercase, W and Λ, and turbulent fluctuations with a lowercase, w and λ. For the present chapter, we follow the more standard notation of equation (1.2).

second term in equation (1.1), γ_λ, accounts for non-local transport that is not directly associated with local vertical gradients of λ, in which we have

$$\overline{w'\lambda'}^{\text{non-local}} = K_\lambda\,\gamma_\lambda. \tag{1.4}$$

KPP is the only scheme available with CVMix that prescribes a nonzero value for γ_λ. Other schemes return zero for this term.

Every scheme available in CVMix returns a value, possibly the null value, for the diffusivity, K_λ, and the non-local transport, γ_λ. It does so based on a standard suite of inputs taken from the calling model, such as the surface buoyancy and momentum fluxes, the vertical stratification, and the vertical shear. Besides the diffusivity and non-local transport, various diagnostic fields are available to help those interested in studying or modifying elements of the parameterizations.

1.3   Ordering the calculations of CVMix parameterizations

Certain of the CVMix schemes are independent, with their resulting diffusivities and viscosities merely added to the total mixing coefficients. Other schemes, however, must be called in a certain order given the underlying assumptions built into the scheme. The main issue concerns the KPP scheme, and there are two points to consider.

- KPP AFTER INTERIOR NON-CONVECTIVE MIXING: Since the KPP scheme matches diffusivities at the base of the boundary layer to values computed beneath the boundary layer (Section 7.5.3), KPP must be called subsequent to those schemes determining non-convective mixing coefficients in the ocean interior.

- KPP BEFORE INTERIOR CONVECTIVE MIXING: The matching of diffusivities at the base of the KPP boundary layer intrinsically assumes there to be a transition from typically larger diffusivities in the boundary layer to typically smaller diffusivities in the interior. However, this sort of transition cannot always be ensured, since gravitationally unstable water can appear beneath the boundary layer in which case the interior diffusivities can be quite large. Problems with the diffusivity matching occur if insisting that KPP match its boundary layer diffusivity to a potentially large interior diffusivity arising from convective mixing. To eliminate these problems, convective mixing must be called *after* the KPP boundary layer scheme.

These considerations lead to the recommended flow diagram shown in Figure 1.1 for use of the CVMix schemes.
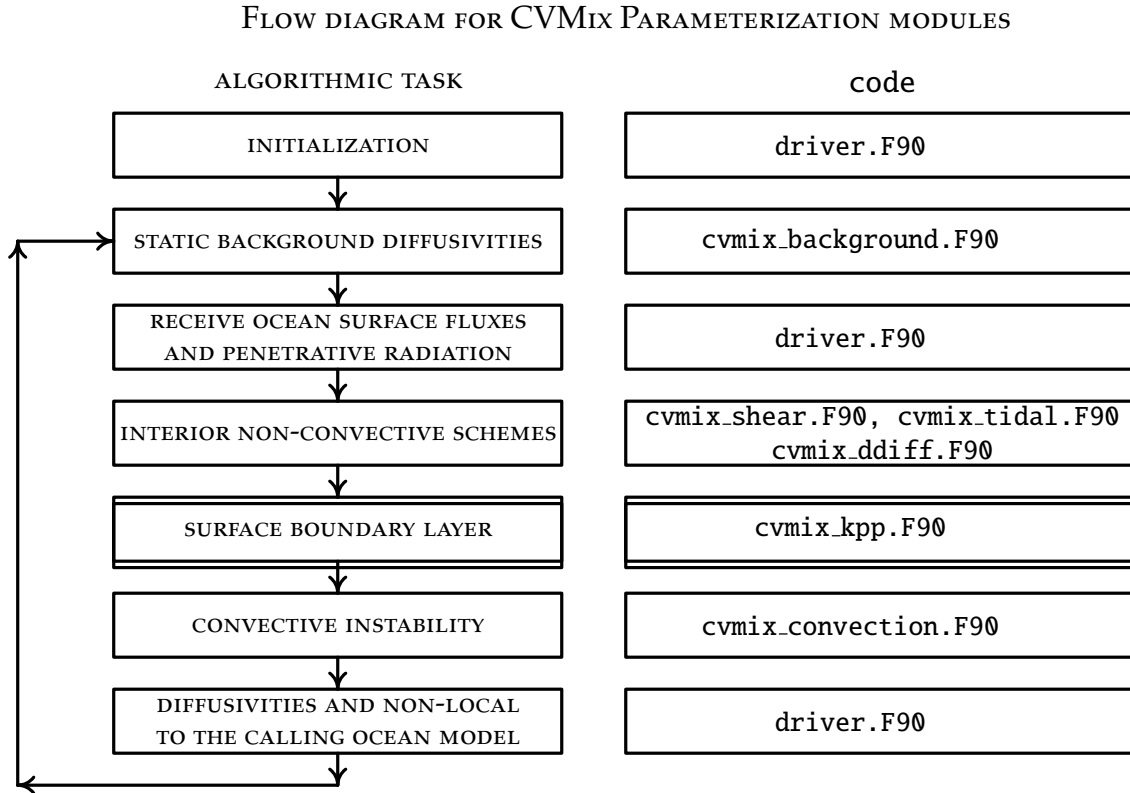
Figure 1.1: This flow diagram depicts the general algorithmic steps required to utilize the CVMix parameterization modules. The initialization step occurs in one of the CVMix drivers that exercises a chosen mixing scheme `driver.F90` if running CVMix code as a stand-alone one-dimensional model. Otherwise it occurs via the ocean model if running CVMix modules as part of an ocean model such as MPAS-ocean, MOM, or POP. This initialization serves to set up arrays and derived type structures, all as a function of the input that it receives from the calling ocean model code. The next step during initialization is to call the module `CVmix_background.F90` to fill chosen static background diffusivities. Upon entering the time dependent portion of the ocean model integration, the driver receives surface fluxes and penetrative radiative fluxes. Calls are made to chosen interior non-convective mixing schemes, such as shear mixing, tide mixing, and double diffusion. Thereafter, the surface boundary layer scheme is called, with KPP the scheme targetted for CVMix. The boundary layer calculation is key to the whole process, as it must come after the interior non-convective portion, and before the convective portion. After the boundary layer, then convective mixing is called, with regions of gravitationally unstable water given a large diffusivity. Notably, if KPP is used for the surface boundary layer, convective mixing is performed only beneath the KPP boundary layer. The final step returns the diffusivity K_λ, viscosity, and non-local transport γ_λ, arrays to the calling ocean model code. A new time step starts by reinitializing the diffusivities to their static background values.

Chapter 2

ELEMENTS OF VERTICAL MIXING SCHEMES

Contents

This chapter presents certain of the elements required for computing various CVMix parameterization schemes. Details specific to particular schemes are provided in later chapters.

2.1 Discrete vertical grid

As part of the numerical discretizations used by CVMix modules, we have need to describe how discrete fields are placed on a vertical grid, and how finite difference operations are performed. A vertical column generally has time dependent positions of the discrete fields, distances between the positions, and thicknesses of the cells over which the discrete fields are defined. Generality is necessary for models where grid cell thicknesses are functions of time, and CVMix allows for such freedom.

Figure 2.1 provides a schematic of the conventions for a tracer column used by CVMix modules. The conventions are motivated by those used in MOM and POP, yet some details may differ slightly. A summary of the choices made in developing this figure are as follows.

- VERTICAL COORDINATE: The vertical coordinate z increases upward and extends from the ocean bottom at $z = -H(x, y)$ to the sea surface at $z = \eta(x, y, t)$.

- TRACER CELL ARRAYS: Tracer cell arrays are labelled with the discrete index kt, and have dimensions nlevs. The index kt increases downward starting from $kt=1$ for the top model grid cell. The number of levels, nlevs, is a function of the column, with only wet points included in a CVMix column. Examples of tracer cell arrays include temperature, salinity, pressure, density, thermal expansion coefficient, and haline contraction coefficient.

- W-CELL OR INTERFACE ARRAYS: W-cell or interface arrays are labelled with the discrete index kw, and have dimensions nlevs+1. The index kw increases downward starting from $kw=1$ at the top ocean interface. The notation "w-cell" originates from the continuity equation, in which the vertical velocity component, w, transfers mass across the vertical interfaces of tracer cells. Examples of w-cell or interface arrays are diffusivity, viscosity, vertical tracer derivatives, buoyancy frequency, and Richardson number. For most w-cell arrays, both the top interface at $kw=1$ and bottom interface at $kw=nlevs+1$ have zero values.

  One argument for using nlevs+1 interfaces is that we avoid ambiguity of where the data resides. Interface arrays of size nlevs could start at either the top or bottom of the first level and, despite documentation, the ambiguity will increase the potential for code errors. It does not matter so much whether interface arrays are dimensioned 0:nlevs or 1:nlevs+1; there is only one way the data could be laid out relative to the tracer arrays which have dimensions 1:nlevs. Yet the reason to prefer 1:nlevs+1 is that this dimensioning simplifies declarations and argument passing, given the standard assumptions made by Fortran in laying out memory for arrays.

- TRACER CELL THICKNESS: The rectangular boxes in Figure 2.1 represent tracer cells whose thickness is measured by the array element dzt(kt) with units of meter. This array has dimensions dzt(nlevs). These thicknesses are generally time dependent. The array dzt is an input to CVMix, passed from the ocean model each time step.

- W-CELL THICKNESS OR TRACER POINT SEPARATION: The array dzw has dimensions dzw(nlevs+1). The array element dzw($kw=1$) measures distance (in meters) from the top of the top tracer cell to the tracer point T($kt=1$), and array element dzw($kw=nlevs+1$) measures the distance from the bottom tracer point T($kt=nlevs$) to the bottom of the bottom tracer cell. Intermediate elements of dzw measure the distance between tracer points, or equivalently the thickness of a w-cell. These distances are generally time dependent. The array dzw is an input to CVMix, passed from the ocean model each time step.

- DISTANCE FROM OCEAN SURFACE TO TRACER CELL POINT: The distance (in meters) from the tracer cell point to the ocean surface is given by the array element zt(kt). This array has dimensions zt(nlevs). If needed, the array zt is constructed inside CVMix code based on the values of dzt and dzw.

- DISTANCE FROM OCEAN SURFACE TO INTERFACE: The distance from the tracer cell interface, or the w-point, to the ocean surface is given by the array element zw(kw). This array has dimensions zw(nlevs+1). If needed, the array zw is constructed inside CVMix code based on the values of dzt and dzw.

2.2   Gravitational stability

Buoyancy stratification plays a key role in ocean physical proceses. We have need to quantify stratification, and the associated gravitational stability of a water column. For this purpose, we introduce the notion of an adiabatic and isohaline parcel displacement, from which we develop an algorithm for computing the buoyancy frequency used to measure vertical stratification. The notions detailed here should be respected by the calling ocean model in order for the CVMix modules to produce physically relevant results.

The squared buoyancy frequency, N^2, is an input to CVMix modules.

2.2.1   Infinitesimal displacements

Consider an infinitesimal displacement $d\mathbf{x}$ of a fluid parcel. The *in situ* density at the new point is related to the reference density by

$$\rho(\mathbf{x} + d\mathbf{x}) = \rho(\mathbf{x}) + d\rho(\mathbf{x}). \tag{2.1}$$
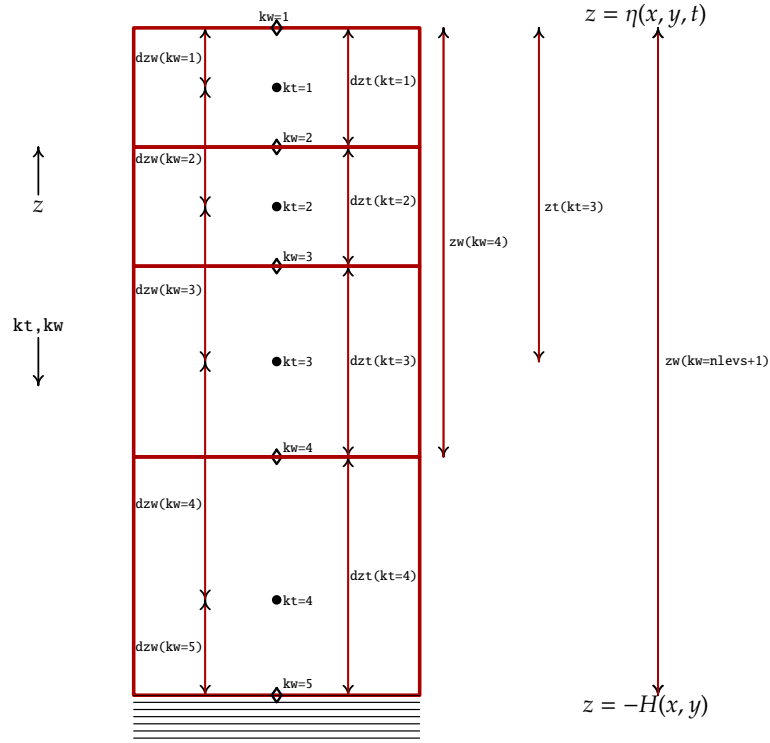
Figure 2.1: Schematic of a discrete vertical column used in CVMix modules, with the surface at $z = \eta(x, y, t)$ and bottom at $z = -H(x, y)$. The vertical coordinate z increases upward, whereas the discrete vertical indices kt and kw increase downward. CVMix code assumes distances and thicknesses are in units of meters. The rectangular boxes represent tracer cells in the ocean model. The array element dzt(kt) measures the thickness of a tracer cell. This array has dimensions dzt(nlevs), where nlevs is the number of wet cells in a particular column. For this particular example, nlevs = 4. The array dzw has dimensions dzw(nlevs+1). The array element dzw(kw=1) measures the distance from the top of the top tracer cell to the tracer point T(kt=1), and array element zw(kw=nlevs+1) measures the distance from the bottom tracer point T(kt=nlevs) to the bottom of the bottom tracer cell. Intermediate elements of dzw measure the distance between tracer points, or equivalently the thickness of w-cells. The distance from the ocean surface to a tracer point is measured by the array element zt(kt), and the distance to the interface is measured by zw(kw). The total thickness of a column is zw(nlevs+1), and it is generally time dependent, as are all of the grid distances dzt and dzw. Arrays that are defined at the interface, such as buoyancy frequency, Richardson number, diffusivity, viscosity, have vertical indices kw. Arrays defined at the tracer cell point, such as temperature, salinity, and density, have vertical indices kt.

Using a Taylor series expansion, the density increment can be approximated by

$$
\begin{aligned}
\mathrm{d}\rho &= \mathrm{d}\mathbf{x} \cdot \nabla\rho \\
&= \rho \, \mathrm{d}\mathbf{x} \cdot \rho^{-1} \, \nabla\rho \\
&= \rho \, \mathrm{d}\mathbf{x} \cdot \left(-\alpha \, \nabla\Theta + \beta \, \nabla S + \frac{\nabla p}{\rho \, c_{\text{sound}}^2} \right),
\end{aligned}
\tag{2.2}
$$

where all terms on the right hand side are evaluated at the reference point $\mathbf{x}$. To reach this expression, we introduced the thermal expansion coefficient

$$
\alpha = -\frac{1}{\rho} \left(\frac{\partial \rho}{\partial \Theta} \right),
\tag{2.3}
$$

the haline contraction coefficient

$$\beta = \frac{1}{\rho}\left(\frac{\partial \rho}{\partial S}\right), \tag{2.4}$$

and the squared sound speed

$$c^2_{\text{sound}} = \left(\frac{\partial p}{\partial \rho}\right). \tag{2.5}$$

The ambient density at the new point, $\rho(\mathbf{x} + \mathrm{d}\mathbf{x})$, thus differs from density at the reference point, $\rho(\mathbf{x})$, by an amount $\mathrm{d}\rho(\mathbf{x})$ according to

$$\rho(\mathbf{x} + \mathrm{d}\mathbf{x}) - \rho(\mathbf{x}) = \rho(\mathbf{x})\,\mathrm{d}\mathbf{x} \cdot \left(-\alpha\,\nabla\Theta + \beta\,\nabla S + \frac{\nabla p}{\rho\,c^2_{\text{sound}}}\right). \tag{2.6}$$

2.2.2 Neutral directions

Displacements that allow for temperature and salinity to change require energy for mixing to occur. Such energy can arise from various sources, such as astronomical tides (Munk and Wunsch, 1998). We are not concerned here with such energy sources. Instead, we wish to know if through buoyancy forces alone a particular parcel displacement is favored, resisted, or neutral. For this purpose, we introduce the notion of a displacment restricted to adiabatic and isohaline conditions (i.e., no heat or salt exchanged during the parcel displacement). Such fictitious displacements occur in the absence of energy needed for mixing, and so they are useful to explore where parcel motions may signal a fluid instability associated with buoyancy forces.

The density change associated with an adiabatic and isohaline displacement is determined just by pressure changes arising from the displacement, so that

$$\rho(\mathbf{x} + \mathrm{d}\mathbf{x})_{\text{adiabatic/isohaline}} - \rho(\mathbf{x}) = \rho\,\mathrm{d}\mathbf{x} \cdot \left(\frac{\nabla p}{\rho\,c^2_{\text{sound}}}\right). \tag{2.7}$$

This density change occurs merely through the pressure dependence of *in situ* density. Operationally, to compute $\rho(\mathbf{x} + \mathrm{d}\mathbf{x})_{\text{adiabatic/isohaline}}$, we may choose to evaluate the right hand side of equation (2.7), or we may evaluate the equation of state at the temperature and salinity of the reference point, $\mathbf{x}$, but with pressure at the displaced point, $\mathbf{x} + \mathrm{d}\mathbf{x}$

$$\rho(\mathbf{x} + \mathrm{d}\mathbf{x})_{\text{adiabatic/isohaline}} = \rho[\Theta(\mathbf{x}), S(\mathbf{x}), p(\mathbf{x} + \mathrm{d}\mathbf{x})]. \tag{2.8}$$

The difference in density between a parcel undergoing an adiabatic and isohaline displacement, $\rho(\mathbf{x} + \mathrm{d}\mathbf{x})_{\text{adiabatic/isohaline}}$, and the density of the ambient environment, $\rho(\mathbf{x} + \mathrm{d}\mathbf{x})$, is thus given by

$$\begin{aligned}\rho(\mathbf{x} + \mathrm{d}\mathbf{x}) - \rho(\mathbf{x} + \mathrm{d}\mathbf{x})_{\text{adiabatic/isohaline}} &= \rho[\Theta(\mathbf{x} + \mathrm{d}\mathbf{x}), S(\mathbf{x} + \mathrm{d}\mathbf{x}), p(\mathbf{x} + \mathrm{d}\mathbf{x})] - \rho[\Theta(\mathbf{x}), S(\mathbf{x}), p(\mathbf{x} + \mathrm{d}\mathbf{x})]\\ &= \rho\,\mathrm{d}\mathbf{x} \cdot (-\alpha\,\nabla\Theta + \beta\,\nabla S).\end{aligned} \tag{2.9}$$

If a parcel makes an adiabatic and isohaline excursion and finds itself in a region where the ambient density is unchanged, then there are no buoyancy forces to resist that displacement. Directions defined by such displacements are termed *neutral directions* (McDougall, 1987). By definition, neutral directions are orthogonal to the local dia-neutral unit vector

$$\hat{\gamma} = \left(\frac{-\alpha\,\nabla\Theta + \beta\,\nabla S}{|-\alpha\,\nabla\Theta + \beta\,\nabla S|}\right), \tag{2.10}$$

so that

$$\rho(\mathbf{x} + \mathrm{d}\mathbf{x}) - \rho(\mathbf{x} + \mathrm{d}\mathbf{x})_{\text{adiabatic/isohaline}} = (\rho\,\mathrm{d}\mathbf{x} \cdot \hat{\gamma})\,|-\alpha\,\nabla\Theta + \beta\,\nabla S|. \tag{2.11}$$

2.2.3 Squared buoyancy frequency

When measuring the gravitational stability of a fluid column, we are concerned with vertical displacements and the resistence from buoyancy stratification to such displacements. To anticipate the needs of the discrete calculation, we assume knowledge of the density, tracer concentration, and pressure at depths z and $z + \mathrm{d}z$ (see Figure 2.2).

2.2.3.1 Stability to upward displacements from a deeper reference point

Consider first an upward displacement starting from the reference depth z and going to $z + dz$. Following the notation of Figure 2.2, we have

$$\rho(z + dz) - \rho(z + dz)_{\text{adiabatic/isohaline}} = \rho[\Theta(z + dz), S(z + dz), p(z + dz)] - \rho[\Theta(z), S(z), p(z + dz)]. \qquad (2.12)$$

As for the case of a general displacement considered in Section 2.2.2, we perform a Taylor series expansion about the reference depth at z to render the leading order identity

$$\rho(z + dz) - \rho(z + dz)_{\text{adiabatic/isohaline}} \approx \rho(z)\, dz \left[-\alpha(z) \left(\frac{\partial \Theta}{\partial z} \right) + \beta(z) \left(\frac{\partial S}{\partial z} \right) \right]$$
$$= -\left(\frac{\rho\, dz}{g} \right) N^2. \qquad (2.13)$$

The final equality in equation (2.15) introduced the squared buoyancy frequency

$$N_{\text{linear}}^2 = g \left(\alpha\, \frac{\partial \Theta}{\partial z} - \beta\, \frac{\partial S}{\partial z} \right), \qquad (2.14)$$

where the vertical derivatives and expansion coefficients are evaluated at the deep reference point z. Calculating gravitational stability according to the linear approximate expresson (2.14) is accurate so long as all higher order terms in the Taylor series approximation can be neglected. It is for this reason we denote this a linear approximation to the buoyancy frequency. The higher order terms are potentially important in regions where the equation of state becomes quite nonlinear, such as the high latitudes of the Southern Ocean. So we do not generally recommend this approximation for global modeling. Instead, we recommend use of the full squared buoyancy frequency

$$N_{\text{full}}^2(z \to z + dz) \equiv -\left(\frac{g\left[\rho(z + dz) - \rho(z + dz)_{\text{adiabatic/isohaline}} \right]}{\rho(z)\, dz} \right) \qquad (2.15)$$

Again, the calculation (2.15) will determine gravitational stability of an upward parcel displacement from depth z to $z + dz$. To further expose the physics of this calculation, consider two vertical stratifications.

- GRAVITATIONALLY STABLE STRATIFICATION: $N_{\text{FULL}}^2(z \to z + dz) > 0$: In this case, a vertically upward displacement occurring without heat or salt exchange will produce a parcel density that is more than the ambient density: $\rho(z + dz) - \rho(z + dz)_{\text{adiabatic/isohaline}} < 0$. This particular adiabatic and isohaline displacement is resisted by buoyancy forces. The vertical density profile is thus gravitationally stable.

- GRAVITATIONALLY UNSTABLE STRATIFICATION: $N_{\text{FULL}}^2(z \to z + dz) < 0$: Now the upward adiabatic and isohaline displacement leads to a lesser density than the ambient environment: $\rho(z + dz) - \rho(z + dz)_{\text{adiabatic/isohaline}} > 0$. This particular adiabatic and isohaline displacement is encouraged by buoyancy forces to rise even further. The vertical density profile is thus gravitationally unstable.

2.2.3.2 Stability to downward displacements from a shallower reference point

We now determine the gravitational stability of fluid to displacements from a shallow reference point $z^* = z + dz$ downward to z, which requires the calculation

$$\rho(z) - \rho(z)_{\text{adiabatic/isohaline}} = \rho[\Theta(z), S(z), p(z)] - \rho[\Theta(z + dz), S(z + dz), p(z)]$$
$$= \rho[\Theta(z^* - dz), S(z^* - dz), p(z)] - \rho[\Theta(z^*), S(z^*), p(z)]$$
$$\approx -\rho\, dz \left[-\alpha \left(\frac{\partial \Theta}{\partial z} \right) + \beta \left(\frac{\partial S}{\partial z} \right) \right]$$
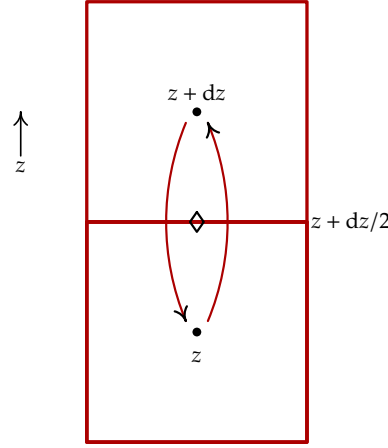$$= \left(\frac{\rho\, dz}{g} \right) N^2, \qquad (2.16)$$

Figure 2.2: Illustration of how parcels are displaced when checking for the gravitational stability. As for the discrete column shown in Figure 2.1, we assume knowledge of the tracer and pressure values at the tracer points z and $z + dz$. Two displacements are considered: one vertically up and one vertically down. The notation corresponds on the discrete grid of Figure 2.1, where $z + dz$ in the present figure corresponds to an interface depth $zw(kw)$; the deeper point at z corresponds to the tracer point $zt(kt+1)$; and the shallower point $z + dz$ corresponds to the tracer point $zt(kt)$.

where terms in the final two equalities are evaluated at the shallow reference point $z^* = z + dz$. Following equation (2.15), we introduce the full squared buoyancy frequency

$$N^2_{\text{full}}(z + dz \to z) \equiv \left(\frac{g \left[\rho(z) - \rho(z)_{\text{adiabatic/isohaline}} \right]}{\rho(z + dz)\, dz} \right). \tag{2.17}$$

2.2.3.3   Combined displacements to approximate gravitational stability at interface depth

Let us summarize the two previous results. Again, we have two tracer points at depths z and $z + dz$. Gravitational stability can be probed in two separate ways. First we consider the deeper depth z as a reference point and displace parcels vertically upward to $z + dz$. This calculation leads to the squared buoyancy frequency at the reference point z

$$
\begin{aligned}
N^2_{\text{full}}(z \to z + dz) &= -\left(\frac{g \left[\rho(z + dz) - \rho(z + dz)_{\text{adiabatic/isohaline}} \right]}{\rho(z)\, dz} \right) \\
&= -\frac{g}{\rho(z)} \left(\frac{\rho[\Theta(z + dz), S(z + dz), p(z + dz)] - \rho[\Theta(z), S(z), p(z + dz)]}{dz} \right).
\end{aligned}
\tag{2.18}
$$

We next the shallower depth $z + dz$ as a reference point and displace parcels vertically downward to z. This calculation leads to the squared buoyancy frequency at the reference point $z + dz$

$$
\begin{aligned}
N^2_{\text{full}}(z + dz \to z) &= \left(\frac{g \left[\rho(z) - \rho(z)_{\text{adiabatic/isohaline}} \right]}{\rho(z + dz)\, dz} \right) \\
&= \frac{g}{\rho(z + dz)} \left(\frac{\rho[\Theta(z), S(z), p(z)] - \rho[\Theta(z + dz), S(z + dz), p(z)]}{dz} \right).
\end{aligned}
\tag{2.19}
$$

We now use these two results to render an approximation to the squared buoyancy frequency at the interface point $z + dz/2$, which is where the discrete calculation requires the stability to be estimated (Section

2.2.3.5). For this purpose, we take the average to yield an expression in terms of density differences

$$
\begin{aligned}
N_{\text{full}}^2(z+\text{d}z/2) &\equiv \frac{N_{\text{full}}^2(z \to z+\text{d}z) + N_{\text{full}}^2(z+\text{d}z \to z)}{2} \\
&= \frac{g}{2}\left(-\frac{\rho[\Theta(z+\text{d}z),S(z+\text{d}z),p(z+\text{d}z)] - \rho[\Theta(z),S(z),p(z+\text{d}z)]}{\rho(z)\,\text{d}z} + \frac{\rho[\Theta(z),S(z),p(z)] - \rho[\Theta(z+\text{d}z),S(z+\text{d}z),p(z)]}{\rho(z+\text{d}z)\,\text{d}z}\right).
\end{aligned}
\tag{2.20}
$$

As a sanity check, note that if the density is independent of pressure, and we replace densities in the denominator with the constant reference density ρ_o, we have the familiar simplified result

$$
N^2(z+\text{d}z/2) = -\frac{g}{\rho_o}\left(\frac{\rho[\Theta(z+\text{d}z),S(z+\text{d}z)] - \rho[\Theta(z),S(z)]}{\text{d}z}\right) \qquad \text{density independent of pressure.} \tag{2.21}
$$

2.2.3.4   Linear approximation: not recommended in general

Instead of computing the full buoyancy frequency in terms of density differences, one may choose to make a linearization of the expansion following equation (2.14), in which we write

$$
\begin{aligned}
N_{\text{linear}}^2(z+\text{d}z/2) &\equiv \frac{N_{\text{linear}}^2(z) + N_{\text{linear}}^2(z+\text{d}z)}{2} \\
&= g\left(\overline{\alpha}^z\,\frac{\partial\Theta}{\partial z} - \overline{\beta}^z\,\frac{\partial S}{\partial z}\right),
\end{aligned}
\tag{2.22}
$$

where we introduced the vertical averaging operator to bring the expansion coefficients from the tracer point to the interface

$$
\overline{\alpha}(z+\text{d}z/2) = \frac{\alpha(z) + \alpha(z+\text{d}z)}{2}. \tag{2.23}
$$

The vertical tracer derivatives are naturally placed on the vertical cell interface. Contrary to the density difference approach of equation (2.20), the expression (2.22) requires no non-standard calculations of the equation of state. What it does require is calculation of the thermal expansion coefficients, with that calculation also used for neutral physics. So the expression (2.22) may be somewhat more efficient. Nonetheless, when used as a measure of gravitational stability, the expression (2.20) makes less assumptions about our ability to truncate the Taylor series at the leading order. This truncation may become problematic particularly in high latitudes where the equation of state can become quite nonlinear. Hence, we generally do not recommend use of the expression (2.22).

2.2.3.5   Discrete calculation of the squared buoyancy frequency

CVMix modules do *not* compute the buoyancy frequency. Rather, the calling model does and then passes N^2 to CVMix. Nonetheless, CVMix modules must assume a placement for the buoyancy frequency, with the following choice made:

> CVMix modules assume the squared buoyancy frequency, N^2, lives at the vertical interface of tracer cells, following the convention given by Figure 2.1.

We now write the buoyancy frequency expression (2.20) in terms of discrete indices for ready incorporation into a numerical model, in which we have

$$
N^2(\text{kw}) = \frac{g}{2}\left(-\frac{\rho[\Theta(\text{kt}),S(\text{kt}),p(\text{kt})] - \rho[\Theta(\text{kt}+1),S(\text{kt}+1),p(\text{kt})]}{\rho(\text{kt}+1)\,\text{dzw}(\text{kw})} + \frac{\rho[\Theta(\text{kt}+1),S(\text{kt}+1),p(\text{kt}+1)] - \rho[\Theta(\text{kt}),S(\text{kt}),p(\text{kt}+1)]}{\rho(\text{kt})\,\text{dzw}(\text{kw})}\right).
\tag{2.24}
$$

Note that by referring to Figures 2.1 and 2.2, we see that the discrete label kt corresponds to the shallower point $z+\text{d}z$, whereas $\text{kt}+1$ corresponds to the deeper point z. This correspondence is made when converting equation (2.20) to equation (2.24).

2.3   Gradient Richardson number

The gradient Richardson number measures the ratio of the stabilizing effects from buoyancy stratification to the destabilizing effects from vertical shear

$$\text{Ri} = \frac{N^2}{|\partial_z \mathbf{u}|^2}. \tag{2.25}$$

In this equation, N^2 is the squared buoyancy frequency, whose discrete calculation was detailed in Section 2.2.3.5. The denominator contains the squared vertical shear of the horizontal velocity, $|\partial_z \mathbf{u}|^2$. When the Richardson number is small, say below 1/4 as in Miles (1961), the flow tends toward a turbulent state via production of Kelvin-Helmholz instabilities.[1] Consequently, many vertical mixing schemes make use of the Richardson number, such as the shear mixing schemes presented in Chapter 4. Additionally, the KPP boundary layer scheme (Chapter 7) makes use of a bulk Richardson number used to define properties of the surface planetary boundary layer (Section 7.5.5).

   As for the squared buoyancy frequency N^2, the CVMix modules do *not* compute a Richardson number, since details of this calculation depend on choices regarding the grid layout in the ocean model. Rather, the Richardson number is an input to CVMix modules. CVMix modules assume a placement for the Richardson number, with the following choice made:

> The gradient Richardson number, Ri, is an input to CVMix modules. CVMix modules assume the gradient Richardson number lives at the vertical interface of tracer cells, following the convention given by Figure 2.1.

   Staggering of tracer and velocity fields on a discrete grid leads to ambiguity for how to compute a discrete Richardson number. The issue is the squared buoyancy frequency in the numerator naturally lives at the vertical interface between tracer grids (Section 2.2.3.5), whereas the horizontal positioning for the denominator depends on the chosen horizontal staggering of velocity. We detail here some possible methods for the B-grid and C-grid. Unstructured grids used by MPAS-ocean require further considerations. Each grid involves averaging operations specific to the grid in order to compute the shear. There are even further methods available if we choose a different discrete placement of N^2 beyond that discussed in Section 2.2.3.5.

2.3.1   Considerations for the B-grid

Figure 2.3 illustrates the horizontal arrangement of prognostic model fields used with the B-grid. The B-grid places both horizontal prognostic velocity components at the same point, the corner of the tracer cell. This placement is natural when computing the Coriolis Force. However, it is unnatural for computation of advective tracer transport or the horizontal pressure gradient force acting on velocity. The need to perform an averaging operation when computing the horizontal pressure gradient leads to the computational mode associated with gravity waves on the B-grid (Mesinger (1973), Killworth et al. (1991), Pacanowski and Griffies (1999), Griffies et al. (2001), and Section 12.9 of Griffies (2004)).

   We present here some methods for computing the squared vertical shear of the horizontal velocity on the B-grid, and thus methods for computing the Richardson number.

- T-GRID AVERAGE OF U-GRID VELOCITY: The first approach computes a horizontal average of the velocity field to place it onto the T-grid, and then computes the vertical derivative and its square. The 4-point horizontal average to compute a T-grid velocity is written

$$\mathbf{u}^{\mathrm{T}} = \overline{\mathbf{u}}^{x,y}. \tag{2.26}$$

---

[1]The critical Richardson number, below which instabilities are enabled, may need to be artificially set larger than the canonical 1/4 when considering discrete approximations to the velocity shear. The reason is that we are unable to precisely compute the vertical shear on a finite grid.
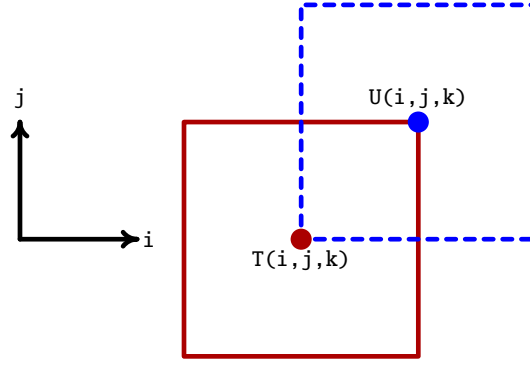
Figure 2.3: Illustration of how fields are placed on the horizontal B-grid using a *northeast convention*. Velocity points U(i,j,k) are placed to the northeast of tracer points T(i,j,k). Both horizontal velocity components $u_{i,j,k}$ and $v_{i,j,k}$ are placed at the velocity point U(i,j,k). Both the tracer point and velocity point have a corresponding grid cell region, denoted by the solid and dashed squares.

Note that this, and all, four point averages do *not* include land points. We next compute the squared vertical shear with the T-grid horizontal velocity for use in the Richardson number calculation

$$\text{Ri}^{\text{(Ba)}} = \frac{N^2}{\left|\frac{\partial \mathbf{u}^{\text{T}}}{\partial z}\right|^2}. \tag{2.27}$$

- T-GRID AVERAGE OF U-GRID SHEAR: A slight modification of the $\text{Ri}^{\text{(Ba)}}$ calculation takes the T-grid horizontal average of the U-grid shear

$$\left(\frac{\partial \mathbf{u}}{\partial z}\right)^{\text{T}} = \overline{\left(\frac{\partial \mathbf{u}}{\partial z}\right)}^{x,y}, \tag{2.28}$$

and then computes the square so that

$$\text{Ri}^{\text{(Bb)}} = \frac{N^2}{\left|\left(\frac{\partial \mathbf{u}}{\partial z}\right)^{\text{T}}\right|^2}. \tag{2.29}$$

With uniform vertical grid spacing, the two Richardson number calculations are the same

$$\text{Ri}^{\text{(Ba)}} = \text{Ri}^{\text{(Bb)}} \qquad \text{uniform vertical grid spacing.} \tag{2.30}$$

- T-GRID AVERAGE OF SQUARED U-GRID SHEAR: The third method computes the squared shear on the original U-grid, and then averages the squared shears onto the T-grid

$$\left(\left|\frac{\partial \mathbf{u}}{\partial z}\right|^2\right)^{\text{T}} = \overline{\left(\left|\frac{\partial u}{\partial z}\right|^2 + \left|\frac{\partial v}{\partial z}\right|^2\right)}^{x,y}, \tag{2.31}$$

so that

$$\text{Ri}^{\text{(Bc)}} = \frac{N^2}{\left(\left|\frac{\partial \mathbf{u}}{\partial z}\right|^2\right)^{\text{T}}}. \tag{2.32}$$

2.3.2 Considerations for the C-grid

Figure 2.4 illustrates the horizontal arrangement of prognostic model fields used with the C-grid. The C-grid places the zonal velocity component on the zonal tracer cell face, and meridional velocity component on the meridional tracer cell face. This placement is suited for computation of advective tracer transport. It
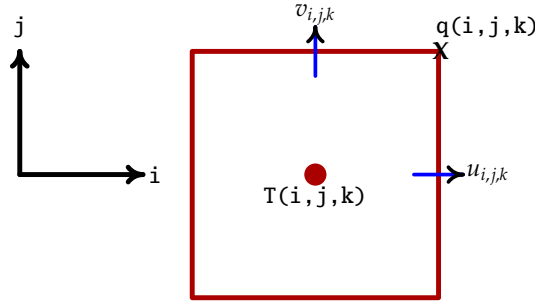
Figure 2.4: Illustration of how fields are placed on the horizontal C-grid. We illustrate here the convention that the zonal velocity component $u_{i,j,k}$ sits at the east face of the tracer cell $\mathsf{T(i,j)}$, and the meridional velocity component $v_{i,j,k}$ sits at the north face of the tracer cell $\mathsf{T(i,j,k)}$. This convention follows the *northeast* convention also used for the B-grid.

is also suited for computing the stress tensor and the horizontal pressure gradient force acting on velocity components. However, it is not natural for computation of the Coriolis Force. The need to perform an averaging operation to compute the Coriolis Force leads to the presence of a computational null mode associated with geostrophically balanced flow (Adcroft et al., 1999).

We present here some methods for computing the squared vertical shear of the horizontal velocity on the C-grid, and thus methods for computing the Richardson number.

- T-GRID AVERAGE OF U,V-GRID VELOCITY COMPONENTS: The first approach considered computes a horizontal average of the u,v velocity components to place both onto the T-grid, and then computes the vertical derivative and its square. The horizontal averaging requires a two-point average so that

$$(u^{\mathrm{T}}, v^{\mathrm{T}}) = (\overline{u}^{x}, \overline{v}^{y}). \tag{2.33}$$

  As for the B-grid averaging considered in Section 2.3.1, all averages considered here do *not* include land points. The squared vertical shear with the T-grid horizontal velocity is then used for the Richardson number calculation

$$\left|\frac{\partial \mathbf{u}^{\mathrm{T}}}{\partial z}\right|^{2} = \left(\frac{\partial \overline{u}^{x}}{\partial z}\right)^{2} + \left(\frac{\partial \overline{v}^{y}}{\partial z}\right)^{2} \tag{2.34}$$

$$\mathrm{Ri}^{(\mathrm{Ca})} = \frac{N^{2}}{\left|\frac{\partial \mathbf{u}^{\mathrm{T}}}{\partial z}\right|^{2}}. \tag{2.35}$$

- T-GRID AVERAGE OF U,V-GRID SHEAR: A slight modification of the $\mathrm{Ri}^{(\mathrm{Ca})}$ calculation takes the T-grid horizontal average of the u,v-grid shear

$$\left(\frac{\partial \mathbf{u}}{\partial z}\right)^{\mathrm{T}} = \left[\overline{\left(\frac{\partial u}{\partial z}\right)}^{x}, \overline{\left(\frac{\partial v}{\partial z}\right)}^{y}\right], \tag{2.36}$$

  and then computes the square so that

$$\mathrm{Ri}^{(\mathrm{Cb})} = \frac{N^{2}}{\left|\left(\frac{\partial \mathbf{u}}{\partial z}\right)^{\mathrm{T}}\right|^{2}}. \tag{2.37}$$

  With uniform vertical grid spacing, the two Richardson number calculations are the same

$$\mathrm{Ri}^{(\mathrm{Ca})} = \mathrm{Ri}^{(\mathrm{Cb})} \qquad \text{uniform vertical grid spacing.} \tag{2.38}$$

- T-GRID AVERAGE OF SQUARED U,V-GRID SHEAR: The third method computes the squared shear on the original u,v-grid, and then averages the squared shears onto the T-grid

$$\left(\left|\frac{\partial \mathbf{u}}{\partial z}\right|^2\right)^{\text{T}} = \overline{\left|\frac{\partial u}{\partial z}\right|^2}^x + \overline{\left|\frac{\partial v}{\partial z}\right|^2}^y \tag{2.39}$$

so that

$$\text{Ri}^{(\text{Bc})} = \frac{N^2}{\left(\left|\frac{\partial \mathbf{u}}{\partial z}\right|^2\right)^{\text{T}}}. \tag{2.40}$$

2.3.3 Considerations for unstructured grids used by MPAS-ocean

To be completed.

Chapter 3

STATIC BACKGROUND SCHEMES

Contents

This chapter presents options in CVMix code for prescribing static (time independent) background diffusivities and viscosities. The following CVMix Fortran module is directly connected to the material in this chapter:

cvmix_background.F90

3.1 Options for static background mixing coefficients

Jochum (2009) describes the large sensitivities found in climate model simulations to the choice of background vertical diffusivities. There are various options in CVMix code for specifying a static background diffusivity and viscosity. These mixing coefficients are generally a function of space but remain the same value throughout the simulation, and so are independent of the flow state. These static values are primarily determined for tracer diffusivity, with a Prandtl number (ratio of diffusivity to viscosity) used to determine the background viscosity. A common choice for Prandtl number is 10, although for some background diffusivities there is no corresponding background viscosity (i.e., zero Prandtl number).

3.2 The profile from Bryan-Lewis (1979)

A classic choice for background diffusivity is that proposed by Bryan and Lewis (1979), which has an arctangent form with smaller values in the upper ocean and larger values beneath a pivot depth, originally set to 1500 m

$$\kappa_{\text{Bryan-Lewis}} = \text{vdc1} + \text{vdc2} \arctan\left[(|z| - \text{dpth})\,\text{linv}\right]. \qquad (3.1)$$

This is the form appearing in POP, where the parameters are defined as follows.

- vdc1 is the diffusivity (squared length per time) at $|z| = \text{dpth}$,

- vdc2 = amplitude of variation for the diffusivity (squared length per time)

- linv is an inverse length scale

- dpth is the vertical depth where the diffusivity equals vdc1.

All lengths and diffusivities should be in MKS units. In many implementations, such as for GFDL-CM2.1, there is no corresponding Bryan-Lewis viscosity, so the corresponding Bryan-Lewis Prandtl number is zero. But more generally, the viscosity is computed according to a chosen Prandtl number.

In MOM5 and earlier versions of MOM, the form (3.1) is written in the somewhat more cumbersome manner for historical reasons

$$\kappa_{\text{Bryan-Lewis}} = \text{convert}\left(\text{afkph} + (\text{dfkph}/\pi)\arctan\left[\text{sfkph}(100|z| - \text{zfkph})\right]\right), \tag{3.2}$$

where afkph, dfkph, sfkph, and zfkph are tunable constants, and $\text{convert} = 1 \times 10^{-4}$ m^{2}s^{-1} converts from the original CGS to MKS. The mapping between the MOM and POP forms (3.1) is given by the following

$$\text{vdc1} = \kappa_o\,\text{afkph} \tag{3.3}$$
$$\text{vdc2} = \kappa_o\,\text{dfkph}/\pi \tag{3.4}$$
$$\text{linv} = 100\,\text{sfkph} \tag{3.5}$$
$$\text{dpth} = 100\,\text{zfkph}. \tag{3.6}$$

We provide this mapping since Figure 3.1 was constructed using the original MOM-based form. Shown are two examples of vertical diffusivity profiles used in the GFDL-CM2.1 simulations (see Griffies et al., 2005, for discussion), with the values given by

$$\text{afkph} = 0.75 \tag{3.7}$$
$$\text{dfkph} = 0.95 \tag{3.8}$$
$$\text{sfkph} = 4.5 \times 10^{-5} \tag{3.9}$$
$$\text{zfkph} = 2500 \tag{3.10}$$

and for the equatorial region they are

$$\text{afkph} = 0.65 \tag{3.11}$$
$$\text{dfkph} = 1.15 \tag{3.12}$$
$$\text{sfkph} = 4.5 \times 10^{-5} \tag{3.13}$$
$$\text{zfkph} = 2500. \tag{3.14}$$

The original implementation from Bryan and Lewis (1979) chose the background as a function only of depth. However, the CM2.1 implementation shown in Figure 3.2 provides an exponential transition from the lower latitude form to the higher latitude form, with the transition latitude taken as 35°. In this way, the background diffusivity is a function of both latitude and depth. The resulting diffusivity is shown in Figure 3.2.

3.3 The profile from Henyey et al. (1986)

To be completed.
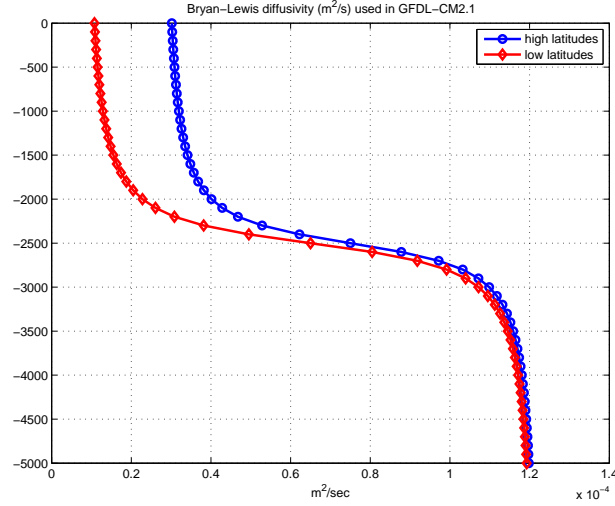
Figure 3.1: Sample vertical profiles for background diffusivities (in units of $m^2 s^{-1}$) given by the Bryan and Lewis (1979) functional form, as used by the OM3 ocean component of the GFDL-CM2.1 climate model (Griffies et al., 2005). The surface values in the tropics are $0.1 \times 10^{-4} m^2 s^{-1}$, whereas they are increased in the high latitudes to $0.3 \times 10^{-4} m^2 s^{-1}$. The Bryan-Lewis coefficients from equation (3.2) for the high latitudes are given by $\mathtt{afkph} = 0.75$, $\mathtt{dfkph} = 0.95$, $\mathtt{sfkph} = 4.5 \times 10^{-5}$, $\mathtt{zfkph} = 2500$, and for the equatorial region they are $\mathtt{afkph} = 0.65$, $\mathtt{dfkph} = 1.15$, $\mathtt{sfkph} = 4.5 \times 10^{-5}$, $\mathtt{zfkph} = 2500$.
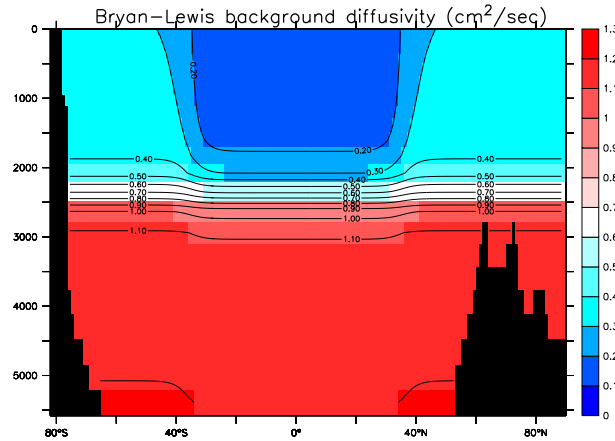
Figure 3.2: Shown here is the latitude dependent Bryan-Lewis diffusivity ($cm^2 s^{-1}$) based on values used in GFDL-CM2.1 configuration discussed in Griffies et al. (2005). The diffusivity is composed of the two profiles shown in Figure 3.1, with an exponential transition at $35°$ from the lower values in the tropics to the larger values in the high latitudes.

Chapter 4

PARAMETERIZED SHEAR INDUCED MIXING

**Contents**

In this chapter we detail the CVMix implementations of parameterizations arising from shear induced mixing in stratified flows. The following CVMix Fortran module is directly connected to the material in this chapter:

$$\texttt{cvmix\_shear.F90}$$

4.1 Mixing from shear instability

Shear induced mixing occurs when vertical shears in the horizontal velocity overcome the stabilizing effects from vertical buoyancy stratification. Shear instability is governed by the local or gradient Richardson number discussed in Section 2.3

$$\mathrm{Ri} = \frac{N^2}{|\partial_z \mathbf{u}|^2}. \tag{4.1}$$

In this expression, N^2 is the squared buoyancy frequency (Section 2.2), with a linear approximation given by

$$N_{\mathrm{linear}}^2 = g \left(\alpha \, \frac{\partial \Theta}{\partial z} - \beta \, \frac{\partial S}{\partial z} \right). \tag{4.2}$$

We assume throughout that the water is stably stratified, so that $N^2 > 0$. With $N^2 < 0$, one should set the diffusivity and viscosity to a large value to parameterize mixing associated with the gravitational instability (see Chapter 8).

The denominator in the Richardson number in equation (4.1) is the squared vertical shear of the horizontal velocity vector resolved by the model grid

$$|\partial_z \mathbf{u}|^2 = \left(\frac{\partial u}{\partial z} \right)^2 + \left(\frac{\partial V}{\partial z} \right)^2. \tag{4.3}$$

When the Richardson number is below a critical value, $\mathrm{Ri} < \mathrm{Ri}_c$, shear instabilities can grow to initiate turbulence, which in turn leads to enhanced mixing.

The canonical value of the critical gradient Richardson number is

$$\text{Ri}_c = 1/4 \qquad \text{analytical value from shear layer instability.} \tag{4.4}$$

This value corresponds to the critical value for initiation of a Kelvin-Helmholz instability in a shear layer (Miles, 1961). However, as reviewed in Section 4b of Jackson et al. (2008), there are many reasons that $1/4$ is not always the optimal value to use in numerical simulations. Thus, most schemes choose noticeably larger values, which allows for shear-induced mixing to be intiated in less unstable regions of the model's resolved flow.

4.2   Richardson number mixing from Pacanowski and Philander (1981)

An early form for parameterized shear mixing is that proposed by Pacanowski and Philander (1981), where their application focused on equatorial dynamics. They used a different viscosity, $\nu_{\text{pp shear}}$, and diffusivity, $\kappa_{\text{pp shear}}$. For gravitationally stable profiles (i.e., $N^2 > 0$), they chose

$$\nu_{\text{pp shear}} = \frac{\nu_0}{(1 + a\,\text{Ri})^n} \tag{4.5}$$

$$\kappa_{\text{pp shear}} = \frac{\nu_0}{(1 + a\,\text{Ri})^{n+1}}, \tag{4.6}$$

where ν_0, a and n are adjustable parameters. Common settings used in POP are $a = 5$ and $n = 2$. Note that the Prandtl number is not constant using this prescription

$$\text{Pr}_{\text{pp}} = \frac{\nu_{\text{pp shear}}}{\kappa_{\text{pp shear}}} \tag{4.7a}$$

$$= 1 + a\,\text{Ri}. \tag{4.7b}$$

4.3   Richardson number mixing from Large et al. (1994)

For regions beneath the KPP boundary layer (see Figure 7.1), Large et al. (1994) and Large and Gent (1999) parameterized shear induced mixing using the following diffusivities

$$\kappa_{\text{kpp shear}} = \begin{cases} \kappa_0 & \text{Ri} < 0 & \text{gravitational instability regime} \\ \kappa_0 \left[1 - \left(\dfrac{\text{Ri}}{\text{Ri}_0} \right)^2 \right]^3 & 0 < \text{Ri} < \text{Ri}_0 & \text{shear instability regime} \\ 0 & \text{Ri} \geq \text{Ri}_0 & \text{stable regime.} \end{cases} \tag{4.8}$$

The form in the shear instability regime falls most rapidly near $\text{Ri} = 0.4\,\text{Ri}_0$, which aims to parameterize the onset of shear instability. In this neighborhood, rapid changes in Ri can cause gravitational instabilities to develop in the vertical, but these are largely controlled by vertically smoothing Ri profiles with a $1-2-1$ smoother. Unlike Pacanowski and Philander (1981), Large et al. (1994) chose a unit Prandtl number for shear induced mixing; i.e., the shear induced viscosity is the same as the shear induced diffusivity

$$\text{Pr}_{\text{kpp}} = \frac{\nu_{\text{kpp shear}}}{\kappa_{\text{kpp shear}}} \tag{4.9a}$$

$$= 1. \tag{4.9b}$$

4.4   Richardson number mixing from Jackson et al. (2008)

To be completed.

Chapter 5

ENERGETICALLY BASED MIXING SCHEMES FROM TIDAL DISSIPATION

Contents

This chapter summarizes the CVMix implementation of the parameterized vertical mixing associated with tidal dissipation in both the ocean interior and near the bottom. The following CVMix Fortran module is directly connected to the material in this chapter:

<div align="center">

`cvmix_tidal.F90`

</div>

5.1 Introduction to tidal induced mixing

Mixing arises when energy dissipates at the small scales in the presence of a nonzero gradient of tracer and/or momentum. There are two sources of energy dissipation considered in this chapter.

- INTERNAL WAVES IN OCEAN INTERIOR: Breaking internal gravity waves arise when barotropic tidal flow is scattered into internal tidal energy. This process occurs when astronomical tides interact with rough bottom topography,

- TIDAL WAVES INTERACTING WITH CONTINENTAL SHELVES: Frictional bottom drag is enhanced as tides encounter continental shelves (whose depths are generally 500 m or less). There is an associated mixing of water masses due to this dissipation.

To resolve both of these dissipation processes explicitly in a numerical model requires grid resolution no coarser than meters in the vertical (throughout the water column), and 1-10 kilometers in the horizontal. This very fine resolution is not generally accessible to global climate models, so it is necessary to consider a parameterization.

CVMix has implementations for the following tide mixing parameterizations.

- BAROCLINIC OR INTERNAL WAVE MIXING: Simmons et al. (2004) presented the first implementation in an ocean climate model of an internal tide mixing parameterization. Jayne (2009) followed with an updated implementation. A more recent study by Melet et al. (2013) implemented the ideas from Polzin (2009) to remove the arbitrariness of the vertical deposition function used by Simmons et al. (2004) and Jayne (2009). Any of these schemes aim to provide a physically based replacement for the static vertical diffusivity of Bryan and Lewis (1979) (Chapter 3).

- BOTTOM DRAG INDUCED MIXING: Legg et al. (2006), in their appendix, present a method to account for the mixing associated with bottom drag dissipation.

Although CVMix provides an optional Prandtl number, it is general practice to assume a unit Prandtl number for each of the tide parameterization schemes.[1]

5.2 Energetic elements of tide mixing parameterizations

We now consider some elements of how various of the energetic based tide mixing parameterizations are formulated.

5.2.1 Bottom drag

Frictional bottom drag is typically parameterized as

$$\mathbf{D}_{\text{bottom drag}} = C_D \, \mathbf{u} \, |\mathbf{u}| \qquad \text{(units of m}^2 \text{ s}^{-2}\text{)}, \tag{5.1}$$

where C_D is a dimensionless drag coefficient with a value on the order of

$$C_D \approx 2 \times 10^{-3}. \tag{5.2}$$

Energy dissipation associated with this bottom drag is given by

$$E_{\text{bottom drag}} = \rho_o \, \mathbf{u} \cdot \mathbf{D}_{\text{bottom drag}} = \rho_o \, |\mathbf{u}|^3 \qquad \text{(units of W m}^{-2}\text{)}, \tag{5.3}$$

where ρ_o is a reference ocean density.

A component to the energy dissipation (5.3) is associated with barotropic tides as they encounter the ocean bottom, particularly continental shelves and other shallow ocean regions. In an ocean model that does not represent the astronomical tides, we may choose to enhance the model's bottom velocity through a root-mean-square tidal speed, U_{tide}, so that the bottom drag takes the form

$$\mathbf{D}_{\text{bottom drag}} = C_D \, \mathbf{u} \left(\mathbf{u}^2 + U_{\text{tide}}^2 \right)^{1/2}, \tag{5.4}$$

where now the velocity $\mathbf{u}$ refers to the model's resolved bottom velocity field. The modified energy dissipation from bottom drag thus takes the form

$$E_{\text{bottom drag}} = \rho_o \, C_D \, \mathbf{u}^2 \left(\mathbf{u}^2 + U_{\text{tide}}^2 \right)^{1/2}. \tag{5.5}$$

Note that the tidal speed U_{tide} may be a prescribed global constant, as in the OCCAM simulations from Webb et al. (1998). It may instead be a map determined by an offline tide model, as in Jayne and St.Laurent (2001). Or, it may be computed online by periodically running a tide model during the update of the primitive equation ocean model.

---

[1] The Prandlt number is the ratio of viscosity to diffusivity.

5.2.2   Wave drag from breaking internal gravity waves

A drag associated with breaking internal gravity waves was written by Jayne and St.Laurent (2001) as

$$\mathbf{D}_{\text{wave drag}} = (1/2)\, N_{\text{bott}}\, \kappa_{\text{topo}}\, h_{\text{topo}}^2\, \mathbf{u} \qquad \text{(units of m}^2\ \text{s}^{-2}\text{)}, \tag{5.6}$$

where N_{bott} is the buoyancy frequency at the ocean bottom, and $(\kappa_{\text{topo}}, h_{\text{topo}})$ are wavenumber (dimensions of inverse length) and amplitude (dimensions of length) scales for the topography. The product $\kappa_{\text{topo}}\, h_{\text{topo}}^2$ has dimensions of length and defines a *roughness length*

$$L_{\text{rough}} = \kappa_{\text{topo}}\, h_{\text{topo}}^2 \tag{5.7}$$

to be specified according to statistics of the observed ocean bottom topography. The internal wave drag can thus be written as

$$\mathbf{D}_{\text{wave drag}} = (1/2)\, N_{\text{bott}}\, L_{\text{rough}}\, \mathbf{u} \qquad \text{(units of m}^2\ \text{s}^{-2}\text{)}. \tag{5.8}$$

The energy dissipation associated with breaking internal gravity waves is given by

$$\begin{aligned} E_{\text{wave drag}} &= \rho_o \left\langle \mathbf{u} \cdot \mathbf{D}_{\text{wave drag}} \right\rangle \\ &= (\rho_o/2)\, N_{\text{bott}}\, L_{\text{rough}}\, \langle \mathbf{u}^2 \rangle \qquad \text{(units of W m}^{-2}\text{)}. \end{aligned} \tag{5.9}$$

In the Jayne and St.Laurent (2001) paper, they emphasize that κ_{topo}, which sets the roughness length through $L_{\text{rough}} = \kappa_{\text{topo}}\, h_{\text{topo}}^2$, is used as a tuning parameter, with the tide model tuned to give sea level values agreeing with observations. Then, the energy dissipation can be diagnosed from the tide model.

As with the bottom drag (Section 5.2.1), the wave energy dissipation arises from energy removed from the barotropic tides, yet here the is transferred into baroclinic tides. Some of the energy transferred into the baroclinic tides dissipates locally due to local wave breaking, and this then leads to enhanced mixing locally. The remaining baroclinic energy propogates away (i.e., it is non-local). The ratio of local to non-local energy is not well known, and is the focus of research.

5.2.3   Relating dissipation to mixing via Osborn (1980)

Mixing occurs when mechanical energy is dissipated in the presence of stratification. The relation between energy dissipation and mixing is not known from first principles, so we consider dimensional arguments to establish a useful form. Since we are concerned with vertical mixing, we assume that diffusivity is inversely proportional to the vertical stratification, with stratification strength measured by the buoyancy frequency, with a linearized form given by equation (2.14)

$$N^2 = -\frac{g}{\rho}\left(\frac{\partial \rho}{\partial \theta}\frac{\partial \theta}{\partial z} + \frac{\partial \rho}{\partial S}\frac{\partial S}{\partial z}\right), \tag{5.10}$$

and a fully nonlinear form detailed in Section 2.2.3. Mechanical energy per mass has units of m^2 s^{-2} = J kg^{-1}, and the dissipation of this energy, written as ϵ, has units of m^2 s^{-3} = W kg^{-1}

$$\epsilon = \text{mechanical energy dissipation in units of m}^2\ \text{s}^{-3} = \text{W kg}^{-1}. \tag{5.11}$$

Together, the energy dissipation and buoyancy frequency define a diffusivity given through the relation (Osborn, 1980)

$$\kappa_{\text{dissipate}} = \frac{\Gamma\, \epsilon}{N^2}, \tag{5.12}$$

where the dimensionless parameter Γ measures the efficiency that mechanical energy dissipation translates into mixing that can be parameterized by a diffusivity acting on vertical stratification. This relation is used throughout the mixing community for converting measurements of mechanical energy dissipation into diffusivity.

The efficiency parameter in equation (5.12) is often chosen as

$$\Gamma = 0.2 \tag{5.13}$$

based measurements (Osborn, 1980; Ivey and Imberger, 1991). However, in regions of very weak vertical stratification, where $N^2 \to 0$, we suggest following Melet et al. (2013), in which the mixing efficiency tends to zero according to

$$\Gamma = 0.2 \left(\frac{N^2}{N^2 + \Omega^2} \right) \tag{5.14}$$

where

$$\begin{aligned} \Omega &= \left(\frac{2\pi + 2\pi/365.24}{86400\text{s}} \right) \\ &= \left(\frac{\pi}{43082} \right) \text{s}^{-1} \\ &= 7.2921 \times 10^{-5} \text{s}^{-1}. \end{aligned} \tag{5.15}$$

is the angular rotation rate of the earth about its axis and about the sun. This modified mixing efficiency reduces the regions where spuriously large values of diffusivity may occur, especially next to the bottom, where low values of N^2 may appear. There is little physical reason to believe the huge diffusivities diagnosed from regions with $N^2 < \Omega^2$.

5.2.4 Vertical deposition function

We are generally concerned in this chapter with mixing induced by energy dissipation that is largest near the bottom. This bottom intensified dissipation leads to the largest levels of mixing also near the bottom. Yet there are means for dissipation to move upwards into the water column, and it is this mixing that generally has far more impact on the ocean stratification. Details of how dissipation moves upwards into the column remains a topic of research. We present here a formulation followed by the CVMix implementations of the Simmons et al. (2004) and Melet et al. (2013) schemes. In this case, we write the energy dissipation in the form

$$\epsilon = \mathcal{E} F(z), \tag{5.16}$$

where $\mathcal{E}$ is an energy dissipation times a length scale, and $F(z)$ is a vertical deposition function with units of inverse length. Both Simmons et al. (2004) and Melet et al. (2013) chose

$$\mathcal{E} = \frac{q\, E_{\text{wave drag}}(x, y)}{\rho}, \tag{5.17}$$

where $E_{\text{wave drag}}(x, y)$ is the energy input to wave drag originating from the bottom (equation (5.9)), ρ is the *in situ* density, and q is the dimensionless fraction of energy that dissipates locally rather than propagating away to dissipate non-locally. We have more to say on q in Section 5.2.5. The vertical deposition function is assumed to integrate to unity over an ocean column

$$\int_{-H}^{\eta} F(z)\, \mathrm{d}z = 1. \tag{5.18}$$

Simmons et al. (2004) chose an empirical exponential function (equation (5.27)) for $F(z)$, whereas Melet et al. (2013) based their choice on theoretical results from Polzin (2009).

5.2.5 Local versus non-local wave energy dissipation

The dimensionless parameter, q, introduced in equation (5.17) measures the fraction of wave energy dissipated locally, and thus contributes to local mixing. Simmons et al. (2004) and Melet et al. (2013) both chose

$$q = 1/3 \tag{5.19}$$

based on the work of St.Laurent et al. (2002). The remaining 2/3 of the wave energy propagates away and is assumed to dissipate non-locally. The non-local dissipation of internal tidal energy, as well as the

dissipation of internal energy from other sources (e.g., wind energy), are accounted for in an *ad hoc* manner via the background diffusivity κ_0 (and background viscosity). A value within the range

$$\kappa_0 = (0.1 - 0.2) \times 10^{-4} \, \text{m}^2 \, \text{s}^{-1} \tag{5.20}$$

is recommended based on the measurements of Ledwell et al. (1993). Other choices are considered in Chapter 3.

Setting $q = 1/3$ globally is strictly incorrect for internal gravity wave dissipation. The actual value is related to the modal content of the excited internal tide, which is related to the roughness spectrum of topography. The redder the mode/roughness spectrum, the lower q. For example, Hawaii has been modelled as a knife-edge by (St.Laurent et al., 2003). This topography excites predominantly low modes, and these modes are stable, propogate quickly, and have long interaction times. That is, they propagate to the far field. Klymak et al. (2005) argue that $q = 0.1$ for Hawaii from the Hawaiian Ocean Mixing Experiment (HOME) data. For the mid-Atlantic ridge, the use of $q = 1/3$, as in Simmons et al. (2004) and Melet et al. (2013), may be more suitable.

The bottom mixing scheme from Legg et al. (2006) in effect assume

$$q = 1 \qquad \text{bottom mixing scheme}, \tag{5.21}$$

which is sensible given that the mixing considered in their scheme occurs predominantly within a bottom boundary layer.

5.2.6   Prandtl number

The Prandtl number is the ratio of viscosity to diffusivity. Simmons et al. (2004) do not discuss vertical viscosity in their study. If one considers a non-zero Prandtl number, then vertical viscosity is enhanced along with the diffusivity when considering internal wave breaking. The following are examples of the Prandlt number chosen for the tide mixing parameterizations.

- The earth system models of Dunne et al. (2012) assume a unit Prandtl number for mixing related to tide mixing.

- What about Jayne (2009)?

5.2.7   General form of the vertical diffusivity

The previous considerations lead to the following general form for a diffusivity arising from mechanical energy dissipation that originates from the ocean bottom

$$
\begin{aligned}
\kappa_{\text{dissipate}} &= \frac{\Gamma \, \epsilon_{\text{dissipate}}}{N^2} \\
&= \frac{\Gamma \, \mathcal{E}_{\text{dissipate}} \, F(z)}{N^2} \\
&= \frac{q \, \Gamma \, E_{\text{dissipate}}(x, y) \, F_{\text{dissipate}}(z)}{\rho \, N^2}.
\end{aligned}
\tag{5.22}
$$

The energy dissipation at the ocean bottom, $E_{\text{dissipate}}(x, y)$, and the vertical deposition function, $F_{\text{dissipate}}(z)$, distinguish the schemes considered by Simmons et al. (2004) and Melet et al. (2013).

5.2.8   Energetic balances

One of the main reasons to formulate diffusivites based on mechanical energy input is that this energy is exchanged in a conservative manner within the ocean. This conservation then leads to self-consistency tests for the model implementation of various energy-based mixing parameterizations. We consider here in particular the work done against stratification by vertical diffusion with a diffusivity $\kappa_{\text{dissipate}}$, with this work given by

$$\mathcal{P} \equiv \int \kappa_{\text{dissipate}} \, \rho \, N^2 \, \text{d}V. \tag{5.23}$$

Use of equation (5.26) for the vertical diffusivity with a constant mixing efficiency $\Gamma = 0.2$ yields

$$
\begin{aligned}
\mathcal{P} &= \int \kappa_{\text{dissipate}}\, \rho\, N^2 \, \mathrm{d}V \\
&= q\,\Gamma \int E_{\text{dissipate}}(x,y)\, \mathrm{d}x\, \mathrm{d}y,
\end{aligned}
\tag{5.24}
$$

assuming $q\,\Gamma$ constant. Note that to reach this result, we set $\int F_{\text{dissipate}}(z)\,\mathrm{d}z = 1$ (Section 5.2.4), which is a constraint that is maintained by the CVMix implementation of the energetic-based mixing schemes. Equation (5.24) says that the energy from some form of dissipation mechanism is deposited in the ocean interior and works against stratification.

For the more general case of $q\,\Gamma$ spatially dependent, we have the balance

$$
\begin{aligned}
\mathcal{P} &= \int \kappa_{\text{dissipate}}\, \rho\, N^2 \, \mathrm{d}V \\
&= \int q\,\Gamma\, E_{\text{dissipate}}(x,y)\, F_{\text{dissipate}}(z)\, \mathrm{d}V,
\end{aligned}
\tag{5.25}
$$

which again is a statement of energy conservation between wave dissipation and mixing of density. Although equation (5.25) is a trivial identity following from the definition of the closure, it is not trivial to maintain in the ocean model. The main reason is that we work with diffusivities when integrating the tracer equations in an ocean model, and these diffusivities are often subjected to basic numerical consistency criteria, such as the following.

- We may wish to have the diffusivities monotonically decay upwards in the column. Given the N^{-2} dependence of the diffusivity in equation (5.22), monotonicity is not guaranteed. Without an added monotonicity constraint, the simulation can be subject to spurious instabilities in which intermediate depths become weakly stratified through some mixing, which in turn produces even larger diffusivities to further reduce the stratification. Jayne (2009) discovered this behaviour in his simulations with POP.

- The diffusivities should be bounded by a reasonable number, such as $50 - 100\,\text{cm}^2\,\text{sec}^{-1}$.

Imposing constraints such as these on the diffusivity corrupts the identity (5.24). In general, the constraints remove energy from the interior, so that in practice $\int \kappa_{\text{dissipate}}\, \rho\, N^2 \, \mathrm{d}V < \int q\,\Gamma\, E_{\text{dissipate}}(x,y)\, \mathrm{d}V$.

5.3 The Simmons et al. (2004) scheme

To account for mixing associated with energy dissipation from breaking internal gravity waves, Simmons et al. (2004) propose a diffusivity given by

$$
\begin{aligned}
\kappa_{\text{simmons}} &= \frac{\Gamma\, \epsilon_{\text{wave drag}}}{N^2} \\
&= \frac{\Gamma\, \mathcal{E}_{\text{wave drag}}\, F_{\text{simmons}}(z)}{N^2} \\
&= \frac{q\,\Gamma\, E_{\text{wave drag}}(x,y)\, F_{\text{simmons}}(z)}{\rho\, N^2},
\end{aligned}
\tag{5.26}
$$

which again is the general form introduced in Section 5.2.7. To reach this result, we used equation (5.16) to introduce the vertical deposition function F_{simmons}, and equation (5.17) to introduce the wave drag energy dissipation, $E_{\text{wave drag}}$, given by equation (5.9).

5.3.1 Calculation of the wave energy dissipation

The wave energy dissipation, $E_{\text{wave drag}}$, is evaluated as follows.

- N_{bott} is computed from the model's evolving buoyancy frequency at the top face of a bottom boundary layer (often just the bottom-most tracer cell). Note that the buoyancy frequency at the bottom face of the bottom-most cell is zero, by definition.

- The effective roughness length $L_{\mathrm{rough}} = \kappa_{\mathrm{topo}} h_{\mathrm{topo}}^2$ requires an algorithm to compute h_{topo} from observed bottom topography, and tide model to tune κ_{topo}. However, in practice what can be done is to take h_{topo} given some variance of topography within a grid cell, and then tune $E_{\mathrm{wave\,drag}}$ to be roughly 1TW in ocean deeper than 1000m, with κ_{topo} as the tuning paramter.

5.3.2 Deposition function

The bottom intensified vertical profile, or deposition function, is taken as

$$
\begin{aligned}
F_{\mathrm{simmons}}(z) &= \frac{e^{-(D-h)/\zeta}}{\zeta\left(1 - e^{-D/\zeta}\right)} \\
&= \frac{e^{h/\zeta}}{\zeta\left(e^{D/\zeta} - 1\right)}.
\end{aligned}
\tag{5.27}
$$

In this expression,

$$
D = H + \eta
\tag{5.28}
$$

is the time dependent thickness of water between the free surface at $z = \eta$ and the ocean bottom at $z = -H$, and

$$
h = -z + \eta
\tag{5.29}
$$

is the time dependent distance from the free surface to a point within the water column.[2] The chosen form of the deposition function is motivated by the microstructure measurements of St.Laurent et al. (2001) in the abyssal Brazil Basin, and the continental slope measurements of Moum et al. (2002). This profile respects the observation that mixing from breaking internal gravity waves, generated by scattered barotropic tidal energy, is exponentially trapped within a distance ζ from the bottom. An *ad hoc* decay scale of

$$
\zeta = 500\,\mathrm{m}
\tag{5.30}
$$

is suggested by Simmons et al. (2004) for use with internal gravity wave breaking in the abyssal ocean.

5.3.3 Regularization of the diffusivity

The diffusivities resulting from this parameterization can reach levels upwards of the maximum around $20 \times 10^{-4}\,\mathrm{m^2\,s^{-1}}$ seen in the Polzin et al. (1997) results. Due to numerical resolution issues, the scheme can in practice produce even larger values. We need to consider the physical relevance of these large values. The following lists some options that the modeller may wish to exercise.

- We may choose to limit the diffusivity to be no larger than a maximum value, defaulted to $50 \times 10^{-4}\,\mathrm{m^2\,s^{-1}}$ in CVMix.

- Based on observations, the mechanical energy input from wave drag (equation (5.9)) should not exceed roughly $0.1\,\mathrm{W\,m^{-2}}$ at a grid point (Bob Hallberg, personal communication 2008). Depending on details of the bottom roughness and tide velocity amplitude, a typical model implementation may easily exceed this bound. Hence, it may be necessary to cap the mechanical energy input to be no larger than a set bound.

- Use of the stratification dependent mixing efficiency (5.14) provides a physically based means to regularize the regions where N^2 can get extremely small.

---

[2]We emphasize that with a free surface, D and h are generally time dependent. Furthermore, with general vertical coordinates, h is time dependent for all grid cells.

5.3.4   Regarding a shallow depth cutoff

Simmons et al. (2004) do not apply their scheme in waters with ocean bottom shallower than 1000m, whereas Jayne (2009) applies the scheme for all depths. CVMix has a namelist that allows for setting a cutoff depth. In principle, there is nothing wrong with using the Simmons et al. (2004) scheme all the way to shallow waters, and removing the somewhat arbitrary depth cutoff is more satisfying. So one may wish to naively use $q = 1/3$ without a 1000m depth cutoff.

Likewise, $\zeta = 500$m globally may be a reasonable choice. The structure function will properly integrate to unity, whether or not the ocean depth H is greater or less than ζ.

5.3.5   Further comments

Here are some further points to consider when setting some of the namelists for this scheme.

- One means to ensure that the diffusivities are within a reasonable bound, without capping them after their computation, is to artificially restrict the stratification used in the calculation to be no less than a certain number. Simmons et al. (2004) chose the floor value $N^2 \geq 10^{-8}\,\text{s}^{-2}$. There is a great deal of sensitivity to the floor value used. GFDL practice is to keep the floor value quite low so that $N^2_{\min} < \Omega^2$.

- If the maximum diffusivity realized by the scheme is allowed to be very large, say much greater than as $1000\,\text{cm}^2\,\text{sec}^{-1}$, then the near bottom stratification can become very small. In this case, $E_{\text{wave drag}}$ can dip below the canonical 1TW value. This process resembles a negative feedback in some manner, though it has not been explored extensively.

5.4   The Melet et al. (2013) scheme

A limitation of the Simmons et al. (2004) scheme is the arbitrary choice of their empirical vertical deposition function (5.27) and the corresponding exponential decay length, ζ. Melet et al. (2013) build on ideas proposed by Polzin (2004, 2009) to overcome these limitations. In their parameterization, they propose a deposition function corresponding to finescale internal wave shear producing an energy dissipation given by

$$\epsilon_{\text{melet}} = \left(\frac{\epsilon_o}{(1 + z^*/z_p^*)^2}\right)\left(\frac{N^2(z)}{\overline{N^2}^z}\right)\left(\frac{1}{H} + \frac{1}{z_p^*}\right). \tag{5.31}$$

The corresponding diffusivity is given by the general form (5.22), so that

$$\begin{aligned}
\kappa_{\text{melet}} &= \frac{\epsilon_{\text{melet}}\Gamma}{N^2} \\
&= \left(\frac{\mathcal{E}_{\text{wave drag}}}{(1 + z^*/z_p^*)^2}\right)\left(\frac{\Gamma}{\overline{N^2}^z}\right)\left(\frac{1}{H} + \frac{1}{z_p^*}\right) \\
&= \left(\frac{q\,\Gamma\,E_{\text{wave drag}}}{\rho\,\overline{N^2}^z}\right)\left(\frac{1}{(1 + z^*/z_p^*)^2}\right)\left(\frac{1}{H} + \frac{1}{z_p^*}\right),
\end{aligned} \tag{5.32}$$

where we set

$$\mathcal{E}_{\text{wave drag}} = \frac{q\,E_{\text{wave drag}}}{\rho} \tag{5.33}$$

according to equation (5.17).

The vertical deposition function

$$F_{\text{melet}} = \frac{N^2}{\overline{N^2}^z}\left(\frac{1}{(1 + z^*/z_p^*)^2}\right)\left(\frac{1}{H} + \frac{1}{z_p^*}\right) \tag{5.34}$$

is algebraic, rather than the exponential suggested by Simmons et al. (2004) (equation (5.27)). A fundamental element to the deposition function is the scaled vertical distance from the bottom

$$z^*(h_{\mathrm{bott}}) = \frac{1}{\overline{N^2}^z} \int_0^{h_{\mathrm{bott}}} N^2(z')\,\mathrm{d}z', \tag{5.35}$$

where the vertical integral extends from the bottom at $h_{\mathrm{bott}} = 0$ to an arbitrary distance above the bottom. The depth averaged squared buoyancy frequency is given by

$$\overline{N^2}^z = \frac{1}{H+\eta} \int_{-H}^{\eta} N^2(z)\,\mathrm{d}z. \tag{5.36}$$

Note that by definition, the rescaled vertical height from the bottom satisfies

$$0 \le z^* \le H. \tag{5.37}$$

We also introduced the rescaled length scale according to

$$z_p^* = z_p \left(\frac{N_{\mathrm{bott}}^2}{\overline{N^2}^z} \right), \tag{5.38}$$

The bottom buoyancy frequency, N_{bott}^2, is computed according to the discussion in Section 5.3.1.

The length scale z_p is computed according to Polzin (2004, 2009), and needs to be written here...

Chapter 6

DOUBLE DIFFUSION

Contents

This chapter details the parameterization of mixing from double diffusive processes. The following CVMix Fortran module is directly connected to the material in this chapter:

<div align="center">cvmix_ddiff.F90</div>

Elements of this chapter should be rewritten to incorporate the Turner angle as in the presentation of Large (2012) (see his Figure 6.8)

6.1 Introduction to mixing from double diffusive processes

Double diffusion processes (Schmitt, 1994) have the potential to significantly enhance vertical diffusivities. The key stratification parameter of use for double diffusive processes is

$$R_\rho = \frac{\alpha}{\beta}\left(\frac{\partial \Theta/\partial z}{\partial S/\partial z}\right), \tag{6.1}$$

where the thermal expansion coefficient is given by

$$\alpha = -\frac{1}{\rho}\left(\frac{\partial \rho}{\partial \Theta}\right), \tag{6.2}$$

and the haline contraction coefficient is

$$\beta = \frac{1}{\rho}\left(\frac{\partial \rho}{\partial S}\right). \tag{6.3}$$

Note that the effects from double diffusive processes on viscosity are ignored in CVMix for two reasons:

- The effects on viscosity are not well known.

- For most applications, the vertical Prandtl number is larger than unity (often 10) for background viscosities (Chapter 3), so that modifying the vertical viscosity according to double diffusion will not represent a sizable relative impact.

There are two regimes of double diffusive processes, with the parameterization different in the regimes. We now detail how CVMix parameterizes vertical mixing in these two regimes.

6.2 Salt fingering regime

The salt fingering regime occurs when salinity is destabilizing the water column (salty above fresh water) and when the stratification parameter R_ρ is within a particular range:

$$\frac{\partial S}{\partial z} > 0 \tag{6.4}$$

$$1 < R_\rho < R_\rho^0 = 2.55. \tag{6.5}$$

The parameterized vertical diffusivity in this regime is fit to observational estimates given by Laurent and Schmitt (1999), who propose the following form

$$\kappa_d = \kappa_d^0 \left[1 - \frac{R_\rho - 1}{R_\rho^0 - 1} \right]^3. \tag{6.6}$$

The default values for the parameter κ_d^0 are set to

$$\kappa_d^0 = \begin{cases} 1 \times 10^{-4} \text{ m}^2 \text{ s}^{-1} & \text{for salinity and other tracers} \\ 0.7 \times 10^{-4} \text{ m}^2 \text{ s}^{-1} & \text{for temperature.} \end{cases} \tag{6.7}$$

6.3 Diffusive convective regime

Diffusive convective instability occurs where the temperature is destabilizing (cold above warm) and with $0 < R_\rho < 1$

$$\frac{\partial \Theta}{\partial z} < 0 \tag{6.8}$$

$$0 < R_\rho < 1. \tag{6.9}$$

For temperature, the vertical diffusivity used in Large et al. (1994) is given by

$$\kappa_d = \nu_{\text{molecular}} \times 0.909 \exp\left(4.6 \exp\left[-.54 \left(R_\rho^{-1} - 1 \right) \right] \right), \tag{6.10}$$

where

$$\nu_{\text{molecular}} = 1.5 \times 10^{-6} \text{ m}^2 \text{ s}^{-1} \tag{6.11}$$

is the molecular viscosity of water. Multiplying the diffusivity (6.10) by the factor

$$\text{factor} = \begin{cases} \left(1.85 - 0.85 R_\rho^{-1} \right) R_\rho & 0.5 \le R_\rho < 1 \\ 0.15 R_\rho & R_\rho < 0.5, \end{cases} \tag{6.12}$$

gives the diffusivity for salinity and other tracers.

7

KPP SURFACE OCEAN BOUNDARY LAYER

Contents

This chapter summarizes the KPP scheme proposed for the ocean surface boundary layer by Large et al. (1994). Further reference to the material in this chapter include the pedagogical chapters from Large (1998) and Large (2012). The following CVMix Fortran module is directly connected to the material in this chapter:

<div align="center">cvmix_kpp.F90</div>

7.1 Elements of the K-profile parameterization (KPP)

The ocean surface boundary layer (OBL) mediates the exchange of properties between the ocean and other components of the climate system. Hence, parameterization of processes active in the OBL are fundamental to the integrity of a climate simulation. The K-profile parameterization (KPP) is a widely used method for parameterizing boundary layer processes in both the atmosphere and ocean. The paper by Large et al. (1994) introduced this scheme to the ocean community for use in parameterizing processes in the surface ocean boundary layer . The pedagogical lectures by Large (1998) and Large (2012) provide added insight into the scheme that complements some of the material in Large et al. (1994).

The KPP scheme has been used by many ocean climate studies for parameterizing mixing in the OBL, with examples discussed in Large et al. (1997), Holland et al. (1998), Gent et al. (1998), Umlauf et al. (2005), Li et al. (2001), Smyth et al. (2002), Durski et al. (2004), and Chang et al. (2005)). We consider here only the implementation of KPP for the surface ocean boundary layer, as implementations for the bottom do not exist in MOM or POP.

7.1.1 Conventions

We use the following conventions that are consistent with Large et al. (1994) and Large (1998).

- The fluid is assumed to be volume conserving Boussinesq, with extensions to a mass conserving non-Boussinesq fluid trivial.

- The vertical direction, z, increases up with $z = 0$ defining the resting ocean surface. The ocean free surface is defined by $z = \eta(x, y, t)$ and the static ocean bottom is at $z = -H(x, y)$.

- A lowercase λ is used to denote a turbulent fluctuation of an arbitrary field within the surface ocean boundary layer; e.g., a tracer such as potential or conservative temperature θ and salinity s), or a velocity component (u, v, w). Note that x is the notation used in Large et al. (1994) and Large (1998), but we prefer the Greek letter λ to avoid confusion with the horizontal spatial coordinate.

- An uppercase Λ is used to denote the Eulerian mean of a tracer or velocity component within the surface ocean boundary layer; e.g., potential or conservative temperature Θ, salinity S, or velocity component (U, V, W). The Eulerian mean fields are time stepped by an ocean climate model within the boundary layer, and correlations of turbulent variables must be parameterized to close the mean field equations.

- The expression $\overline{w\,\lambda}$ is used to symbolize the Eulerian correlation of the fluctuating turbulent vertical velocity and a fluctuating scalar or vector field. This correlation appears in the mean field time tendency equation for Λ in the Boussinesq primitive ocean equations (see equation (7.2)). KPP provides a parameterization of this vertical turbulent flux within the surface ocean boundary layer.

- The mean and turbulent vertical velocity components, W, w, are positive for upward motion. This sign convention implies that

$$\overline{w\,\lambda} > 0 \implies \text{turbulent flux for } \lambda \text{ transported vertically upward.} \tag{7.1}$$

If λ is the temperature, then a positive correlation at the ocean surface, $\overline{w\,\theta}^{(\eta)} > 0$, corresponds to surface cooling.

7.1.2   General form of the parameterization

Ignoring all terms except vertical advective transport in the prognostic equation for the mean field Λ, its time tendency is determined by

$$\frac{\partial \Lambda}{\partial t} = -\left(\frac{\partial (W\,\Lambda)}{\partial z}\right) - \left(\frac{\partial (\overline{w\,\lambda})}{\partial z}\right). \tag{7.2}$$

The advective flux by the mean vertical velocity, $W\,\Lambda$, is represented via a numerical advection operator. In contrast, the turbulent correlation, $\overline{w\,\lambda}$, is a subgrid scale flux that must be parameterized in order to close the equation for Λ. Here, the overbar signifies an Eulerian averaging operator over unresolved turbulent motions occurring within the OBL.

The KPP scheme provides a first order closure for $\overline{w\,\lambda}$ within the OBL. It does so by introducing two terms in the following manner

$$\overline{w\,\lambda} = -K_\lambda \left(\frac{\partial \Lambda}{\partial z} - \gamma_\lambda\right). \tag{7.3}$$

In effect, the KPP parameterization (7.3) splits the vertical turbulent flux into two terms

$$\overline{w\,\lambda} = \overline{w\,\lambda}^{\text{local}} + \overline{w\,\lambda}^{\text{non-local}}. \tag{7.4}$$

The first term provides for the familiar downgradient vertical diffusion determined by a vertical diffusivity and the local vertical derivative of the mean field. This term is referred to as the local portion of the parameterization

$$\overline{w\,\lambda}^{\text{local}} = -K_\lambda \left(\frac{\partial \Lambda}{\partial z}\right), \tag{7.5}$$

even though the diffusivity is a non-local function of boundary layer properties. The second term, γ_λ, accounts for non-local transport that is not directly associated with local vertical gradients of Λ, in which

$$\overline{w\,\lambda}^{\text{non-local}} = K_\lambda\,\gamma_\lambda. \tag{7.6}$$

We next provide a general discussion of these two contributions to the KPP parameterization.

7.1.3 The vertical diffusivity

The vertical diffusivity arising from KPP in the OBL is determined as a non-local function of boundary layer properties. It is written in the following form

$$K_\lambda(\sigma) = h\, w_\lambda(\sigma)\, G_\lambda(\sigma). \tag{7.7}$$

The diffusivity is a constructed as the product of three terms: the boundary layer thickness h, the vertical turbulent velocity scale $w_\lambda(\sigma)$, and the vertical shape function $G_\lambda(\sigma)$. Note that we introduce a dependence of the shape function on the field diffused. As discussed in Section 7.5.3, this dependence arises from matching to interior diffusivities, which are generally a function of λ.

7.1.3.1 Boundary layer thickness

The boundary layer thickness is denoted by

$$h \geq 0 \quad \text{is the boundary layer thickness.} \tag{7.8}$$

This is the thickness of the OBL prescribed by the KPP scheme, with details given in Section 7.5.5. The direct dependence of the vertical diffusivity in equation (7.7) on the OBL thickness manifests the common property of boundary layers, whereby thicker layers generally arise from stronger eddy motions and are thus associated with more rapid mixing of tracer concentration and momentum.

Figure 7.1 provides a schematic of the KPP boundary layer, the Monin-Obukhov surface layer, and the associated momentum, mass, and buoyancy fluxes impacting these layers. Details of this figure will be explored in the following.

7.1.3.2 Measuring vertical distances within the OBL

When measuring distances within the boundary layer, it is the thickness of the water as measured from the ocean surface that is important. Free surface undulations can be a nontrivial fraction of the boundary layer thickness, particularly under conditions of stable buoyancy forcing. Hence, we make explicit note that the ocean has an undulating free surface at $z = \eta(x, y, t)$, which contrasts to Large et al. (1994) and Large (1998), who assumed that $z = 0$ sets the upper ocean surface.

Following Large et al. (1994), we introduce the non-dimensional depth, σ, given by

$$\sigma = \frac{d}{h}. \tag{7.9}$$

In this definition, $d \geq 0$ is the distance from the ocean surface at $z = \eta$ to a point within the boundary layer

$$d = -z + \eta. \tag{7.10}$$

Likewise, $h \geq 0$ is the distance from the free surface to the bottom of the boundary layer

$$h = h_{\text{obl}} + \eta, \tag{7.11}$$

where h_{obl} is the depth of the boundary layer as measured from $z = 0$. That is, h is the thickness of the OBL, and it is this thickness, not h_{obl}, that is predicted by KPP (Section 7.5.5). Regions within the boundary layer are given by the non-dimensional depth range

$$0 \leq \sigma \leq 1 \quad \text{within boundary layer,} \tag{7.12}$$

with $\sigma = 0$ the ocean surface and $\sigma = 1$ the bottom of the boundary layer.

7.1.3.3 Vertical turbulent velocity scale w_λ

The velocity scale w_λ is a function of depth within the boundary layer, and a function of the field to which it refers. We return to its specification in Section 7.5.1.
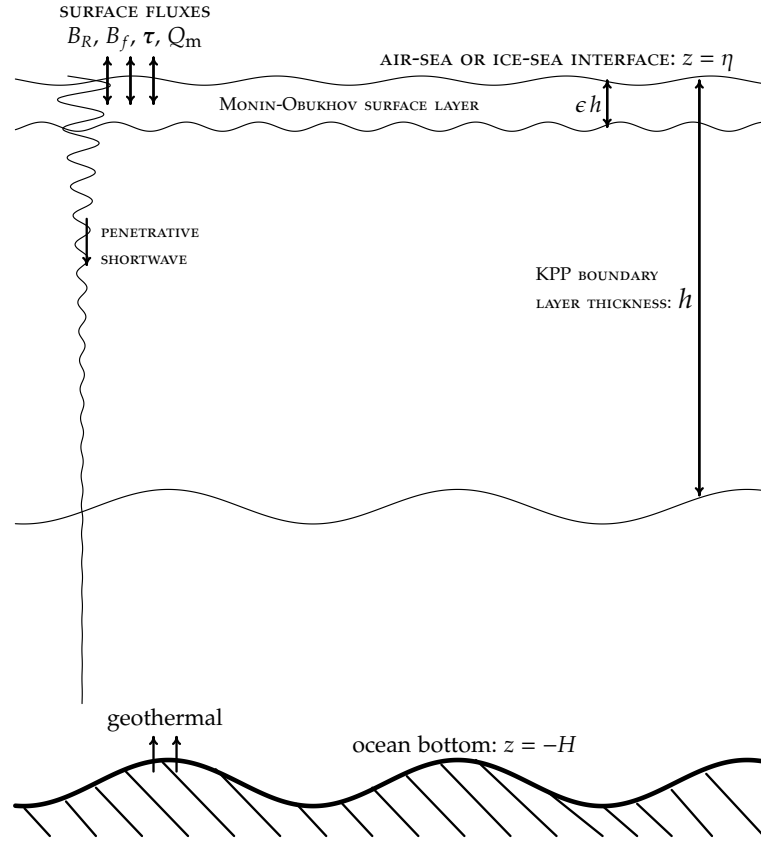
Figure 7.1: Schematic of the upper ocean boundary layer regions associated with the KPP boundary layer parameterization. The upper ocean is exposed to non-penetrative air-sea and ice-sea fluxes of momentum τ (Section 7.2), mass Q_{m}(Section 7.3), and buoyancy B_f (Section 7.3). In addition, there is penetrative shortwave radiation, $-\overline{w\,\theta}_R$ (Section 7.3), indicated by the exponentially decaying vertical sinusoidal. The Monin-Obukhov surface layer (Section 7.4) has a thickness $\epsilon\,h$, with $\epsilon \approx 0.1$. The surface layer is where turbulence delivers fluxes to the molecular skin layer for transfer to the atmosphere or ice. The surface layer starts from just beneath the surface roughness elements at the upper ocean interface. Since neither these roughness elements, nor the molecular viscous sublayer, are resolved in ocean models, we assume in practice that the Monin-Obukhov surface layer extends to the sea surface at $z = \eta(x,y,t)$. The KPP boundary layer includes the surface layer, and it has a thickness $h(x,y,t)$ determined by the KPP parameterization (Section 7.5.5). The ocean bottom at $z = -H(x,y)$ is rigid and is exposed to geothermal heating. Presently, the KPP boundary layer scheme has not been implemented in MOM or POP to parameterize bottom boundary layer physics, though nothing fundamental precludes such. In fact, Durski et al. (2004) provide just such an implementation.

7.1.3.4 Non-dimensional vertical shape function $G_\lambda(\sigma)$

Non-dimensional vertical shape function $G_\lambda(\sigma)$ is used to smoothly transition from the ocean surface to the bottom of the boundary layer. Large et al. (1994) chose a cubic polynomial

$$G_\lambda(\sigma) = a_0 + a_1\,\sigma + a_2\,\sigma^2 + a_3\,\sigma^3. \tag{7.13}$$

Since turbulent eddies do not cross the ocean surface at $\sigma = 0$, we should correspondingly have a vanishing diffusivity at $\sigma = 0$. This constraint is satisfied by setting

$$a_0 = 0. \tag{7.14}$$

We detail in Section 7.5.3 how to specify the remaining expansion coefficients a_1, a_2, a_3. In particular, we simplify the specification of Large et al. (1994), with their approach more complex than justified physically.

7.1.4 The non-local transport γ_λ

Section 2 of Large et al. (1994) notes the presence of many processes in the boundary layer that lead to nonlocal transport. This behaviour leads to a diffusivity K_λ that is a function of the surface fluxes and boundary layer thickness h. Furthermore, under convective forcing (negative surface buoyancy forcing; $B_f < 0$), fluxes can penetrate into stratified interior. This characteristic then motivates the introduction of a non-local transport term γ_λ to the KPP parameterization (equation (7.3)) when $B_f < 0$. To further identify the need for a non-local transport term γ_λ, we reproduce Figure 1 from Large et al. (1994), here shown as Figure 7.2. The caption to Figure 7.2 explores the many facets of this figure used to help justify the non-local term in KPP.

As part of the KPP parameterization, the non-local transport, γ_λ, aims to account for such processes as boundary layer eddies whose transport may be unrelated to the local vertical gradient of the mean field, and whose impacts may penetrate within the stratified ocean interior. In general, Large et al. (1994) prescribe the following characteristics to γ_λ.

- Page 371 of (Large et al., 1994) notes that there is no theory for non-local momentum transport, and so the non-local transport directly affects only the tracer fields:

$$\gamma_\lambda = \begin{cases} 0 & \text{if } \lambda = (u, v, w) \text{ a velocity component} \\ \neq 0 & \text{nonzero if } \lambda = \theta, s \text{ or another tracer.} \end{cases} \tag{7.15}$$

  However, Smyth et al. (2002) consider a non-local term for momentum, thus motivating further research to see whether it is suitable for climate modeling.

- The non-local transport is non-zero only within the OBL:

$$\gamma_\lambda = \begin{cases} 0 & \text{if } \sigma > 1 \\ \neq 0 & \text{if } 0 \leq \sigma \leq 1. \end{cases} \tag{7.16}$$

- The non-local transport is non-zero only in the presence of destabilizing negative surface ocean buoyancy flux, whose presence gives rise to convective mixing:

$$\gamma_\lambda = \begin{cases} 0 & \text{for positive (stabilizing) surface buoyancy forcing} \\ \neq 0 & \text{for negative (destabilizing) surface buoyancy forcing.} \end{cases} \tag{7.17}$$

- The non-local transport can give rise, under certain conditions, to either down-gradient or up-gradient transport of the mean tracer field. Hence, it can either act to smooth gradients of mean fields (down-gradient non-local fluxes) or enhance gradients (upgradient non-local fluxes).

In Section 7.5.4, we provide to the KPP parameterization of γ_λ.

7.2 Surface ocean boundary momentum fluxes

In this section and Section 7.3, we present features of how surface boundary fluxes force the upper ocean, largely following Appendix A of Large et al. (1994). The aim is to identify how surface boundary fluxes impact the upper ocean, with this characterization then used in Section 7.4 to help establish some basic features of ocean boundary layers. These ideas are then used in Section 7.5 to specify the diffusivity and non-local transport from the KPP parameterization.

Vertical exchange of momentum across the atmosphere-ocean or sea-ice-ocean boundary occurs largely through turbulent processes. The resulting horizontal stress vector acting on the ocean, $\boldsymbol{\tau}$, is determined through application of a bulk formula (e.g., see Appendix C of Griffies et al., 2009). For our purposes,
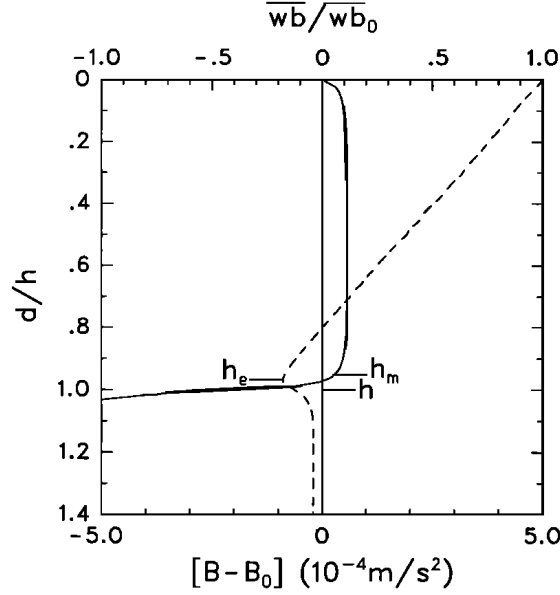
Figure 7.2:   This is a reproduction of Figure 1 from Large et al. (1994). The figure is derived from a one-dimensional simulation after 3 days of convective deepening (zero winds; negative surface buoyancy forcing) into an initially uniformly stratified water column. The vertical axis is vertical distance starting from the ocean surface interface at $z = \eta$ and $d = 0$, extending down to $d = h$ ($h = 13.6$ m at this point of the integration), which is the base of the boundary layer, and finally to $d = 1.4\,h$, which is beneath the boundary layer.

The horizontal axis on the bottom is the mean buoyancy, B, relative to that at the surface, B_0, and the profile is depicted by the solid line. Positive values of $B - B_0$ indicate that the mean buoyancy at a point is larger than at the surface, with $B - B_0 > 0$ expected under negative buoyancy forcing at the ocean surface.

The horizontal axis on the top is the ratio of the local turbulent buoyancy flux $\overline{wb}$ to the surface turbulent flux $\overline{wb}^{\eta}$ (denoted $\overline{wb}_0$ by Large et al. (1994)). The dashed line depicts this ratio. Positive values of $\overline{wb}$ represent upward turbulent buoyancy fluxes; e.g., upward fluxes of heat for the case where buoyancy is determined by temperature, and the thermal expansion coefficient is positive.

Positive values for $\overline{wb}$ in regions between roughly $0.35 < d < 0.8$ represent upward turbulent buoyancy fluxes in a region where the mean vertical gradient of B is nearly zero, thus indicating non-local turbulent transport. In shallower regions with $d < 0.35$, the mean gradient is negative, $\partial_z B < 0$, and the fluxes are positive, $\overline{wb} > 0$, thus representing downgradient turbulent fluxes. Likewise, for $d > 0.8$, the turbulent fluxes are downgradient.

The mixed layer depth is denoted by h_m, though this depth is subject to arbitrary specification of the density difference. The entrainment depth is h_e, with this depth taken where the buoyancy flux reaches a negative extrema. Note that it is an empirical result that under pure convective forcing ($\tau = 0, B_f < 0$), the turbulent entrainment flux is roughly 20% of the surface flux: $\overline{wb}^{d=h_e} = -\beta_T \, \overline{wb}^{d=0}$, where $\beta_T = 0.2$. This situation is depicted in the figure.

we assume τ is given, thus yielding the ocean kinematic fluxes associated with the turbulent transport of momentum across the ocean surface

$$-\overline{w\mathbf{u}}^{\eta} = \left(\frac{\tau}{\rho(\eta)}\right) \approx \left(\frac{\tau}{\rho_0}\right). \tag{7.18}$$

In this equation, $\rho(\eta)$ is the surface ocean density, which is commonly approximated by the constant Boussinesq reference density ρ_0. A positive sign on a component of τ acts to accelerate the flow in the respective

direction, whereas a positive sign to a component of $\overline{w\mathbf{u}}^\eta$ removes momentum from the ocean. These sign conventions give rise to the minus sign in the relation (7.18). In addition to defining the kinematic surface fluxes, knowledge of $\boldsymbol{\tau}$ allows us to compute surface boundary layer velocity scales when working within the Monin-Obukhov similarity theory (Section 7.4.2).

In addition to turbulent momentum transfer, $\boldsymbol{\tau}$ is associated with momentum transported through mass exchange across the ocean surface, since water transported across the ocean generally carries a nonzero momentum. Kantha and Clayson (2000) (see their page 431) point out that this effect can be nontrivial, particularly when resolving strong atmospheric storms. They also make the case for including this effect in computing the Monin-Obukhov length scale defined by equation (7.65)) (see their equation (4.3.11)). Notably, when running a coupled model, the stress from rain is included, since it is part of the momentum convergence acting at the bottom of the atmospheric column. Modifying the stress from a prescribed atmospheric state, such as CORE (Large and Yeager, 2009), requires further considerations.

7.3 Surface ocean boundary buoyancy fluxes

Turbulent and advective fluxes of momentum and buoyancy are transferred across the upper ocean surface boundary, with ocean processes such as advection and mixing then transporting the boundary momentum and buoyancy laterally as well as into the ocean interior. In contrast, penetrative shortwave radiation is absorbed into the ocean absent ocean transport processes, with such absorption a function of ocean optical properties. In the unphysical case of perfectly transparent seawater, shortwave radiation penetrates through the boundary layer and so has no influence on boundary layer processes. In realistic cases, much of the shortwave radiation is absorbed in the boundary layer, with only a fraction leaking through to the interior. In general, such non-turbulent and non-advective transport of buoyancy via penetrative radiation represents a fundamentally novel aspect of ocean boundary layer physics relative to the atmosphere. Namely, for the atmosphere, radiative absorption is far less relevant than in the upper ocean, since the atmosphere is largely transparent to radiation. We therefore consider penetrative shortwave radiation as distinct from other buoyancy fluxes when formulating how boundary fluxes impact the ocean.

7.3.1 General features of buoyancy forcing

The buoyancy of a fluid is commonly defined as (e.g., page 83 of Large (1998))

$$B = g\left(\frac{\rho_0 - \rho}{\rho_0}\right), \tag{7.19}$$

where g is the constant gravitational acceleration, and ρ_0 is a reference density, taken here to equal the Boussinesq reference density. A reduction in density is associated with an increase in buoyancy; that is, the water becomes more *buoyant*. Changes in buoyancy arise through changes in density associated with temperature and salinity changes, since buoyancy changes are computed relative to a fixed pressure level. In this way, buoyancy changes are directly related to processes that impact locally referenced potential density.

Ocean buoyancy is affected through surface ocean heat, salt, and water fluxes.

- Turbulent processes transfer heat through latent and sensible heating.

- Longwave radiation cools the upper ocean, with this radiation affected by the upper ocean skin temperature.

- Penetrative shortwave radiation is absorbed in seawater.

- The transfer of salt occurs when sea ice melts and forms. This transfer is proportional to the water mass flux and the difference in salinity between the liquid ocean and sea ice. More generally, we simply consider this to be a salt flux between sea ice and ocean, with this flux operationally computed as part of a sea ice model.

- Advective processes transfer heat and salt across the ocean surface through the transfer of water mass across the interface.

We further detail these fluxes in the following.

7.3.2 Temperature, salinity, and mass budget for a surface ocean model grid cell

Buoyancy is not a prognostic variable in ocean models. So to develop a quantative understanding of how buoyancy is impacted by surface fluxes, we consider the evolution of temperature, salinity, and mass in an arbitrary top model grid cell, and focus exclusively on evolution arising from surface boundary fluxes. We write these budgets in their finite volume sense as in MOM, which includes density and thickness weighting

$$\partial_t (\rho \, dz \, \Theta) = Q_m \, \Theta_m - Q_\theta^{\text{non-pen}} + \left(Q_\theta^{\text{pen}}(z = \eta) - Q_\theta^{\text{pen}}(z = -\Delta z) \right) \tag{7.20}$$

$$\partial_t (\rho \, dz \, S) = Q_m \, S_m - Q_S \tag{7.21}$$

$$\partial_t (\rho \, dz) = Q_m. \tag{7.22}$$

We now detail the terms appearing in these equations.

- $\rho \, dz$ is the mass per horizontal area of seawater in the grid cell. For a volume conserving Boussinesq fluid, ρ is set to the constant reference density ρ_0.

- Θ is the grid cell potential temperature, or more accurately it is the conservative temperature of McDougall (2003).

- S is the grid cell salinity.

- Q_m is the mass flux ($\text{kg m}^{-2} \text{sec}^{-1}$) of water crossing the ocean surface, with $Q_m > 0$ for water entering the ocean (as when precipitation plus runoff exceeds evaporation).

- Θ_m is the temperature of water crossing the ocean surface, and $C_p \, Q_m \, \Theta_m$ is the associated heat flux (W m^{-2}). We further discuss this heat flux in Section 7.3.4.

- S_m is the salinity of water crossing the ocean surface, and $Q_m \, S_m$ is the associated mass flux. Note that S_m is typically taken to be zero, as for precipitation and evaporation. However, rivers can contain a nonzero salt concentration, so we keep S_m for the following formulation. We further discuss this salt flux in Section 7.3.4.

- C_p is the seawater heat capacity at constant pressure ($\text{J kg}^{-1} \, {}^\circ\text{C}^{-1}$). IOC et al. (2010) provides the most precise value appropriate for an ocean with heat measured through conservative temperature.

- Q_S is the flux of salt ($\text{kg m}^{-2} \text{sec}^{-1}$) that leaves the ocean through the ocean surface. This flux arises in the transfer of salt when sea ice forms and melts. We further discuss this salt flux in Section 7.3.3.

- $C_p \, Q_\theta^{\text{non-pen}}$ is the non-penetrative surface heat flux associated with turbulent processes (latent and sensible) and radiative longwave cooling (W m^{-2}). The sign convention is chosen so that $Q_\theta^{\text{non-pen}} > 0$ for heat leaving the ocean surface (i.e., ocean cooling). We further discuss this heat flux in Section 7.3.5.

- $C_p \, Q_\theta^{\text{pen}}(z = \eta)$ is the radiative shortwave heat flux (W m^{-2}) entering the ocean through its surface at $z = \eta$, with $Q_\theta^{\text{pen}}(\eta) > 0$ warming the ocean surface. Likewise, $C_p \, Q_\theta^{\text{pen}}(z = -\Delta z)$ is the radiative shortwave heat flux leaving the top cell through its bottom face. We further discuss this heat flux in Section 7.3.7.

7.3.3 Salt fluxes from sea ice melt and formation

The mass flux of salt Q_S ($\text{kg m}^{-2} \text{sec}^{-1}$) is positive for salt leaving the ocean surface. There is transport of salt across the ocean surface when sea ice forms and melts, due to the nonzero salt content in sea ice. Otherwise, the surface salt flux is generally zero for the large scale ocean. For ocean models, however, the salt flux can be nonzero when formulating the surface boundary in terms of virtual salt fluxes rather than real water fluxes (Huang, 1993; Griffies et al., 2001). This formulation is not recommended, as it is distinctly unphysical and unnatural, particularly when using an explicit free surface or bottom pressure.

7.3.4 Salt and heat fluxes associated with water transport

In most cases, salinity in the water fluxed across the ocean surface is zero, so that $S_m = 0$. However, there are some cases where rivers have a nonzero salinity so that $S_m \neq 0$ and the product $Q_m S_m$ leads to an advective transport of salt across the ocean surface.

Since water transported across the ocean has a nonzero heat content, this transport in turn affects the net heat content in the upper ocean. One can either prescribe the temperature of this water, Θ_m, or the product $Q_m \Theta_m$. Consider the case where the product is specified for river water entering the ocean, which is the case with the GFDL land model used in the earth system model of Dunne et al. (2012). In this case, the heat flux with respect to $0°C$ (in units of W m^{-2}) of liquid river runoff $\mathcal{H}^{\text{liquid runoff}}$ is given to the ocean from the land model, so that

$$Q_m \Theta_m = \frac{\mathcal{H}^{\text{liquid runoff}}}{C_p^{\text{liquid runoff}}}, \tag{7.23}$$

with $C_p^{\text{liquid runoff}}$ the heat capacity of the water coming in from the river runoff. Likewise, if the heat associated with frozen runoff (e.g., calving land ice) is provided by the land model, then we have

$$Q_m \Theta_m = \frac{\mathcal{H}^{\text{solid runoff}}}{C_p^{\text{solid runoff}}}, \tag{7.24}$$

with $C_p^{\text{solid runoff}}$ the heat capacity of the solid runoff. These two heat capacities are typically provided by the component model (i.e., the land model) used to compute the runoff fields. Similar considerations hold for transfer of water betwen sea ice models and the ocean.

7.3.5 Non-penetrative surface heat fluxes

The heat flux $C_p Q_\theta^{\text{non-pen}}$ (W m^{-2}) is defined with a sign so that it is positive for heat leaving the ocean. This flux is comprised of the following contributions (see page 34 of Gill, 1982)

$$C_p Q_\theta^{\text{non-pen}} = Q_{\text{long}} + Q_{\text{latent}} + Q_{\text{sens}}. \tag{7.25}$$

Longwave, latent, and sensible heat fluxes are typically deposited or withdrawn from the ocean surface layer (Section 7.4). In practice, ocean models assume these fluxes are taken entirely from the surface grid cell.

These fluxes are termed non-penetrative, since they are deposited or withdrawn from the liquid ocean at a particular depth, generally the top model grid cell. Transport of the boundary buoyancy to another depth occurs only through the action of ocean transport processes, such as advection or mixing. This behaviour contrasts to that of penetrative shortwave radiation, which is transferred to depths as a function of seawater optics, so does not depend on ocean transport. We now comment in a bit more detail on the various non-penetrative fluxes.

7.3.5.1 Longwave radiation

Q_{long} is the longwave radiation leaving the ocean in the form of the $\sigma_{\text{SB}} T^4$ Stefan-Boltzmann Law, with T the skin temperature. Q_{long} is positive, thus cooling the ocean surface. There is, however, longwave heating that results from cloud reflection of longwave cooling, thus tempering the cooling impacts on the ocean.

7.3.5.2 Latent heat fluxes

Q_{latent} arises from phase changes whereby liquid seawater either evaporates, or it acts to melt frozen precipitation. When seawater evaporates, the latent heat lost by the ocean is determined by the latent heat of vaporization for fresh water

$$H^{\text{vapor}} = 2.5 \times 10^6 \, \text{J kg}^{-1}, \tag{7.26}$$

so that

$$Q_{\text{evap}} = H^{\text{vapor}} Q_m^{\text{evap}} \tag{7.27}$$

where $Q_{\mathrm{m}}^{\mathrm{evap}}$ is the mass flux ($\mathrm{kg\,m^{-2}\,sec^{-1}}$) of fresh water leaving the ocean due to evaporation. A similar expression holds when seawater melts frozen precipitation (e.g., snow), in which case

$$H^{\mathrm{fusion}} = 3.34 \times 10^5\,\mathrm{J\,kg^{-1}}, \tag{7.28}$$

so that

$$Q_{\mathrm{melt}} = H^{\mathrm{fusion}}\, Q_{\mathrm{m}}^{\mathrm{frozen\ precip}}, \tag{7.29}$$

where $Q_{\mathrm{m}}^{\mathrm{frozen\ precip}}$ is the mass flux ($\mathrm{kg\,m^{-2}\,sec^{-1}}$) of frozen precipitation falling onto the ocean surface. Both Q_{evap} and Q_{melt} are positive, indicating that they act to cool the ocean.

7.3.5.3 Sensible heat fluxes

Q_{sens} is the sensible heat transfer proportional to the difference between atmosphere and ocean temperatures. Sensible heating generally acts to cool the ocean, particularly near western boundary currents such as the Gulf Stream, Kuroshio, and Agulhas.

7.3.6 The case of frazil

As the temperature of seawater cools to the freezing point, sea ice is formed, initially through the production of frazil ice. Frazil can generally form at various levels in the upper ocean, though many ocean models assume frazil production occurs just in the top grid cell. Operationally in an ocean model, liquid water can be supercooled at any particular time step through surface fluxes and transport. An adjustment process is used to heat the liquid water back to the freezing point, with this positive heat flux $Q_{\mathrm{frazil}} > 0$ extracted from the ice model as frazil sea ice is formed. When that adjustment is performed may determine whether to include Q_{frazil} as part of the net heat flux impacting the boundary layer turbulence. We omitted frazil heating in equation (7.25), as that is the approach taken at NCAR. However, others, such as GFDL prior to 2012, include frazil as part of the KPP boundary layer calculation. We summarize the issues here.

- FRAZIL OMITTED FROM B_f: When computing B_f for KPP, the NCAR practice omits frazil heating, as reflected in equation (7.25). In effect, this approach assumes that all the negative buoyancy forcing that occurs in the upper ocean is used to drive convective boundary layer turbulence. After mixing, a portion of the heat, $Q_{\mathrm{frazil}} > 0$, is returned to the liquid ocean to warm the water back to freezing, with this heat taken from the ice model as it forms frazil sea ice.

- FRAZIL INCLUDED IN B_f: Many ocean climate models compute frazil heating just in the top model grid cell. It is thus operationally trivial to include $Q_{\mathrm{frazil}} > 0$ as another term in the non-penetrative heating (equation (7.25)). Physically, this approach adds the amount of heat Q_{frazil} to the buoyancy flux, and so potentially reduces the strength of the otherwise convective turbulence in the upper ocean. This approach has been used at GFDL prior to 2012.

We have no strong argument for one approach versus the other. Tests should be run to consider sensitivity to the choice.

7.3.7 Penetrative shortwave heating

The penetrative shortwave radiative heat flux $C_p\, Q_\theta^{\mathrm{pen}} > 0$ arises from the net shortwave radiation entering through the ocean surface and absorbed by seawater. This heat flux does *not* arise from turbulent or advective processes, which makes it distinct from other heat and salt fluxes impacting the ocean through its upper boundary. This radiation is not generally deposited entirely within the ocean surface layer or the top ocean model grid cell. Instead, a fraction of this radiation can penetrate to beneath the surface ocean grid cell, with the fraction depending on the optical properties of seawater. Hence, we subtract a heat flux $C_p\, Q_\theta^{\mathrm{pen}}(z = -\Delta z)$, which represents the radiative shortwave heat flux passing through the bottom of the surface ocean cell at $z = -\Delta z$. It is the difference,

$$\text{net shortwave heating of surface grid cell} = C_p\left(Q_\theta^{\mathrm{pen}}(z = \eta) - Q_\theta^{\mathrm{pen}}(z = -\Delta z)\right) \tag{7.30}$$

that stays in the surface grid cell. When considering the same budget for the surface ocean boundary layer, we are interested in the shortwave flux that penetrates through the bottom of the boundary layer at $z = -h$.

7.3.8   Buoyancy budget for a surface ocean model grid cell

We now bring the previous fluxes together to form the budget for buoyancy in a surface grid cell due to the impacts of surface fluxes. The resulting expression is then used to derive an expression for the buoyancy forcing that acts on the ocean surface boundary layer. Buoyancy (equation (7.19)) has a time tendency given by

$$-\left(\frac{\rho_0}{g}\right)\frac{\partial B}{\partial t} = \rho_{,\Theta}\,\frac{\partial \Theta}{\partial t} + \rho_{,S}\,\frac{\partial S}{\partial t}, \tag{7.31}$$

where we introduced the shorthand notation

$$\rho_{,\Theta} = \left(\frac{\partial \rho}{\partial \Theta}\right)_{S,p} \tag{7.32}$$

$$\rho_{,S} = \left(\frac{\partial \rho}{\partial S}\right)_{\Theta,p} \tag{7.33}$$

for the partial derivatives of density with respect to conservative temperature and salinity, respectively, each with pressure held constant. We wish to form an evolution equation for buoyancy at the ocean surface grid cell just due to the effects of surface forcing. For this purpose, multiply the temperature equation (7.20) by $\rho_{,\Theta}$ and add to the surface salinity equation (7.21) multiplied by $\rho_{,S}$

$$\rho_{,\Theta}\,(\rho\,dz\,\Theta)_{,t} + \rho_{,S}\,(\rho\,dz\,S)_{,t} = Q_{\mathrm{m}}\,(\rho_{,\Theta}\,\Theta_{\mathrm{m}} + \rho_{,S}\,S_{\mathrm{m}}) + \rho_{,\Theta}\left(-Q_\theta^{\text{non-pen}} + \delta_k\,Q_\theta^{\text{pen}}\right) - \rho_{,S}\,Q_S, \tag{7.34}$$

where we introduced the shorthand

$$\delta_k\,Q_\theta^{\text{pen}} = Q_\theta^{\text{pen}}(z=\eta) - Q_\theta^{\text{pen}}(z=-\Delta z). \tag{7.35}$$

We now use the mass budget (7.22) and introduce the buoyancy tendency according to equation (7.31) to realize an expression for the time tendency of the surface ocean buoyancy

$$(\rho_0/g)\,\rho\,dz\left(\frac{\partial B}{\partial t}\right) = Q_{\mathrm{m}}\left[\rho_{,\Theta}\,(\Theta - \Theta_{\mathrm{m}}) + \rho_{,S}\,(S - S_{\mathrm{m}})\right] + \rho_{,\Theta}\left(Q_\theta^{\text{non-pen}} - \delta_k\,Q_\theta^{\text{pen}}\right) + \rho_{,S}\,Q_S. \tag{7.36}$$

Now introduce the thermal expansion and saline contraction coefficients

$$\alpha = -\frac{1}{\rho}\left(\frac{\partial \rho}{\partial \Theta}\right)_{S,p} \tag{7.37}$$

$$\beta = \frac{1}{\rho}\left(\frac{\partial \rho}{\partial S}\right)_{\Theta,p} \tag{7.38}$$

to render

$$dz\left(\frac{\partial B}{\partial t}\right) = \frac{g}{\rho_0}\left(Q_{\mathrm{m}}\left[-\alpha\,(\Theta - \Theta_{\mathrm{m}}) + \beta\,(S - S_{\mathrm{m}})\right] + \alpha\,(\delta_k\,Q_\theta^{\text{pen}} - Q_\theta^{\text{non-pen}}) + \beta\,Q_S\right). \tag{7.39}$$

7.3.9   Surface boundary terms contributing to ocean buoyancy evolution

We now summarize the various surface boundary terms appearing on the right hand side of the surface buoyancy budget (7.39).

7.3.9.1   Heat carried by water transport

Assuming a positive thermal expansion coefficient, $\alpha > 0$, the term $-Q_{\mathrm{m}}\,\alpha\,(\Theta - \Theta_{\mathrm{m}})$ reduces ocean buoyancy when adding water $Q_{\mathrm{m}} > 0$ to the ocean that is colder than the surface ocean temperature, $\Theta = \Theta_{k=1}$. The opposite occurs in regions of cold fresh waters, such as the Baltic, where $\alpha < 0$. In such cases, adding water to the ocean that is colder than the sea surface temperature increases seawater buoyancy. We now consider in turn the three cases evaporation, precipitation, and liquid river runoff and indicate how they are typically treated in climate models.

- It is quite accurate to assume that evaporating water leaves the ocean at the sea surface temperature, so that

$$\Theta^{\mathrm{evap}} = \Theta_{k=1}, \tag{7.40}$$

in which case there is no change to ocean buoyancy upon transfer of evaporating water across the ocean surface. This is the approach taken by all ocean climate models.

- Precipitating liquid water need not fall on the ocean at the sea surface temperature, so that

$$\Theta^{\mathrm{precip}} \neq \Theta_{k=1} \qquad \text{real world.} \tag{7.41}$$

Kantha and Clayson (2000) (see their page 429) discuss this difference, and the associated transfer of heat across the ocean due to rain events, particularly in the West Pacific. However, we know of no climate modeling application in which the atmospheric model component carries information about the temperature of its condensed water, nor the heat content of that water. Hence, operationally all climate modeling applications assume that

$$\Theta^{\mathrm{precip}} = \Theta_{k=1} \qquad \text{climate models,} \tag{7.42}$$

in which case there is no change in ocean buoyancy upon transfer of precipitating liquid water across the ocean surface.

- Realistic river models carry the heat content of river water and pass this content to the ocean model at river mouths. Following from the discussion surrounding equation (7.23), we may thus write the river contribution to the buoyancy budget in the form

$$-Q_{\mathrm{m}} \, \alpha \, (\Theta - \Theta_{\mathrm{m}}) = \alpha \left(-Q_{\mathrm{m}} \Theta + \frac{\mathcal{H}^{\mathrm{liquid\ runoff}}}{C_p^{\mathrm{liquid\ runoff}}} \right). \tag{7.43}$$

Depending on the heat content of liquid runoff relative to the sea surface, ocean buoyancy may increase or decrease when liquid runoff enters the ocean.

7.3.9.2 Salt carried by water transport

The haline contraction coefficient, β, is generally positive. Hence, the term $Q_{\mathrm{m}} \beta \, (S - S_{\mathrm{m}})$ increases ocean buoyancy for those cases where the sea surface salinity, $S_{k=1}$, is greater than the salinity of the water transferred across the ocean surface. Most applications assume $S_{\mathrm{m}} = 0$, such as for evaporation and precipitation

$$S^{\mathrm{evap}} = 0 \tag{7.44}$$
$$S^{\mathrm{precip}} = 0. \tag{7.45}$$

However, river models sometimes consider a nonzero salinity of the runoff, in which case

$$S^{\mathrm{liquid\ runoff}} \neq 0. \tag{7.46}$$

7.3.9.3 Penetrative radiation

Shortwave radiation is absorbed by seawater as it penetrates from the surface into the upper ocean. Hence, $\delta_k \, Q_\theta^{\mathrm{pen}} > 0$ so that radiation increases the grid cell buoyancy.

7.3.9.4 Non-penetrative heating

Longwave, latent, and sensible heating generally cool the upper ocean, and so lead to a decrease in ocean buoyancy for regions where the thermal expansion coefficient, α, is positive. In those few regions where $\alpha < 0$, such as the Baltic, non-penetrative cooling can stabilize the column.

7.3.9.5 Salt fluxes due to sea ice melt or formation

Salt is exchanged with the ocean when sea ice melts and forms, so that the term $\beta \, Q_S$ can either increase (when salt is removed from the liquid ocean) or decrease (when salt is added to the liquid ocean) buoyancy.

7.3.10 Buoyancy forcing that acts on the OBL

The expression (7.39) for the buoyancy forcing from surface fluxes acting on a surface grid cell is now extended to an expression for the buoyancy forcing on the OBL. The only subtle point concerns the treatment of penetrative shortwave radiation. Rather than consider that radiation leaving the bottom of the surface cell at $z = -\Delta z$, we are now concerned with that leaving the bottom of the boundary layer at $z = -h$. We also multiply this penetrative flux by the thermal expansion coefficient at that depth, rather than the expansion coefficient in the ocean surface cell. In this way we write the buoyancy forcing acting on the boundary layer

$$B_f = \frac{g}{\rho_0} \Big[Q_\mathrm{m} \left[-\alpha \left(\Theta - \Theta_\mathrm{m} \right) + \beta \left(S - S_\mathrm{m} \right) \right] - \alpha \, Q_\theta^{\mathrm{non\text{-}pen}} + \beta \, Q_S \Big] + \Big[\left(\alpha \, Q_\theta^{\mathrm{pen}} \right)_{z=\eta} - \left(\alpha \, Q_\theta^{\mathrm{pen}} \right)_{z=-h} \Big]. \tag{7.47}$$

This expression for the net buoyancy forcing acting on the boundary layer can be written as the sum of two terms

$$B_f = -\overline{w\,b}^{\,\eta} + B_R. \tag{7.48}$$

The first term takes the form of a kinematic turbulent flux at the ocean surface

$$-\overline{w\,b}^{\,\eta} = \frac{g}{\rho_0} \Big[Q_\mathrm{m} \left[-\alpha \left(\Theta - \Theta_\mathrm{m} \right) + \beta \left(S - S_\mathrm{m} \right) \right] - \alpha \, Q_\theta^{\mathrm{non\text{-}pen}} + \beta \, Q_S \Big], \tag{7.49}$$

where the minus sign on the left hand side accounts for the assumption that $w > 0$ for upward velocity. The second term accounts for the penetrative radiation, which is neither a turbulent flux nor advective flux

$$B_R = \left(\alpha \, Q_\theta^{\mathrm{pen}} \right)_{z=\eta} - \left(\alpha \, Q_\theta^{\mathrm{pen}} \right)_{z=-h}. \tag{7.50}$$

The corresponding heat flux convergence onto the boundary layer is given by (see equation (A4) of Large et al. (1994))

$$Q_R = \left(Q_\theta^{\mathrm{pen}} \right)_{z=\eta} - \left(Q_\theta^{\mathrm{pen}} \right)_{z=-h}. \tag{7.51}$$

Notably, B_R, and hence B_f, are two-dimensional functions of the boundary forcing, even though they depend on the depth to which the penetrative radiation extends.

7.4 Surface layer and Monin-Obukhov similarity

The semi-empirical Monin-Obukhov similarity theory has proven quite useful in describing general features of boundary layer turbulence active in the atmospheric planetary boundary layer (see, e.g., Section 3.3 of Kantha and Clayson, 2000). One may thus choose to apply these ideas to the ocean planetary boundary layer, particularly since the atmospheric boundary layer is far better measured than the ocean, and there are certain features that are similar. However, before applying the Monin-Obukhov similarity theory to the ocean, we acknowledge some characteristics of the ocean surface boundary layer that distinguish it from atmospheric boundary layers.

- Surface ocean gravity waves can impact a nontrivial fraction of the ocean surface boundary layer, whereas such waves only impact a small fraction of atmospheric boundary layers.

- The surface ocean velocity is generally the largest velocity in the ocean. In contrast, the surface atmospheric velocity vanishes over land and is relatively small over the ocean.

- The surface ocean absorbs shortwave solar radiation, whereas the atmosphere is nearly transparent to radiation.

Despite these basic distinctions between planetary boundary layers in the atmosphere and ocean, Large et al. (1994) used the Monin-Obukhov similarity theory to introduce scales for turbulent fluctuations and to identify non-dimensional similarity functions in the ocean surface layer.

7.4.1 The surface layer

A molecular layer exists within roughly a millimetre of the upper ocean interface, with this layer dominated by molecular viscous and diffusive effects (Large, 1998). Since it is dominated by molecular viscous effects, this layer is not turbulent and thus leads to negligible mixing of tracer and momentum. It is the molecular layer that ultimately transfers properties between the ocean and atmosphere or ice, including momentum and buoyancy. The more this layer is "corrugated" through wave breaking and other turbulent action, the faster properties are transferred across the surface ocean interface.

The ocean *surface layer* (Figure 7.1) is a turbulent layer whose turbulent fluxes are roughly independent of distance from the upper boundary; i.e., the surface layer is nearly a *constant flux* layer. The surface layer starts just beneath the molecular viscous layer. Turbulence within the surface layer delivers properties to the molecular layer for transfer to the atmosphere or ice (Fairall et al., 1996). Given that no ocean model resolves the molecular sublayer, the upper ocean interface at $z = \eta(x, y, t)$ in an ocean model operationally starts at the top of the surface layer.

7.4.2 Monin-Obukhov similarity theory

The surface turbulent layer is of fundamental importance for determining the rate that properties are transferred across the surface ocean interface. It thus plays a key role in how the ocean is forced. If we needed to model all the details of this layer, then the problem of coupled modeling would perhaps be intractable. Fortunately, the Monin-Obukhov similarity theory has proven to be quite useful in many contexts, particularly for the atmosphere boundary layer. Following Large et al. (1994), we consider its use for the ocean surface boundary layer.

Monin-Obukhov similarity theory assumes that the turbulent surface layer is a constant flux layer that starts just beneath any roughness elements, and certainly beneath the the molecular sublayer. In the absence of breaking surface waves, roughness elements arise from capillary waves that allow the wind to affect the otherwise smooth ocean surface, in which case the roughness length is on the order of centimetres. With breaking surface waves, the roughness length can increase to the order of a metre (e.g., see concluding section to Craig and Banner, 1994). Furthermore, the scalings from Monin-Obukhov are distinctly not correct with surface wave breaking (e.g., Craig and Banner, 1994; Terray et al., 1996). In the formulation of Large et al. (1994), surface gravity waves are ignored, though we have more to say on surface waves in Section 7.6.

Even if the surface layer is not a constant flux layer, the following scalings are relevant so long as the surface fluxes remain the dominant parameters determining properties of this layer (Tennekes, 1973). Within the surface layer, the relevant dimensional quantities are the distance d from the surface interface at $z = \eta$, and the surface kinematic fluxes of momentum, tracer, scalars, and buoyancy

$$\overline{w\mathbf{u}}^{\eta} = \text{surface kinematic momentum flux} \tag{7.52}$$

$$\rho_o\, C_p\, \overline{w\,\theta}^{\eta} = \text{surface kinematic heat flux} \tag{7.53}$$

$$\overline{w\,s}^{\eta} = \text{surface kinematic scalar (e.g., salt) flux} \tag{7.54}$$

$$\overline{w\,b}^{\eta} = \text{surface kinematic buoyancy flux.} \tag{7.55}$$

We now introduce the following dimensional scales.

- FRICTION VELOCITY: From the surface kinematic momentum flux, we introduce the turbulent velocity scale, also known as the *friction velocity* scale

$$u_*^2 \equiv |\overline{w\mathbf{u}}^{\eta}|. \tag{7.56}$$

  Use of the identity (7.18) provides a means to compute the surface friction velocity given the surface momentum stress

$$\rho_0\, u_*^2 = |\boldsymbol{\tau}|. \tag{7.57}$$

- TEMPERATURE SCALE: From the surface kinematic heat flux and the surface kinematic momentum flux, we define a scale for the surface turbulent temperature fluctuations

$$\Theta_* = -\left(\frac{\overline{w\,\theta}^{\eta}}{\sqrt{|\overline{w\,\mathbf{u}}^{\eta}|}}\right) = -\left(\frac{\overline{w\,\theta}^{\eta}}{u_*}\right). \tag{7.58}$$

The sign is chosen so that turbulent fluxes leading to surface ocean cooling, $\overline{w\,\theta}^{\eta} > 0$, correspond to a negative turbulent temperature scale, $\Theta_* < 0$.

- SCALAR SCALE: From the surface kinematic scalar flux and the surface kinematic momentum flux, we define a scale for the surface turbulent scalar fluctuations

$$S_* = -\left(\frac{\overline{w\,s}^{\eta}}{u_*}\right). \tag{7.59}$$

- BUOYANCY SCALE: From the surface kinematic buoyancy flux $-\overline{w\,b}^{\eta}$ (equation (7.49)), and the penetrative buoyancy flux B_R (equation (7.50)), we define a scale for the surface turbulent buoyancy fluctuations

$$B_* = \left(\frac{B_f}{u_*}\right) = \left(\frac{-\overline{w\,b}^{\eta} + B_R}{u_*}\right). \tag{7.60}$$

7.4.3 Similarity functions and length scale

The Monin-Obukhov similarity theory assumes the vertical gradient of any mean field, Λ, within the surface turbulent layer is a function of the scale Λ_* of its turbulent fluctuations, the buoyancy scale B_*, the velocity scale u_*, and the vertical distance from the upper interface, $d = -z + \eta$ (equation (7.10)). In this case, we write

$$\frac{\partial \Lambda}{\partial z} = \Psi(d, u_*, B_*, \Lambda_*), \tag{7.61}$$

where Ψ is an unknown function. Although no exact analytical expression exists for Ψ, Monin-Obukhov theory suggests that progress can be made by fitting data to the following form

$$\frac{\partial \Lambda}{\partial z} = \left(\frac{\Lambda_*}{\kappa\,d}\right)\phi_\Lambda(\zeta). \tag{7.62}$$

In this expression,

$$\kappa \approx 0.4 \tag{7.63}$$

is the von Karman constant, $\phi_\Lambda(\zeta)$ is a dimensionless *similarity function* or flux profile that is dependent only on the scaled distance

$$\zeta \equiv \frac{d}{L}, \tag{7.64}$$

and

$$L = \frac{u_*^2}{\kappa\,B_*} = \frac{u_*^3}{\kappa\,B_f} = \frac{|\tau/\rho_0|^{3/2}}{\kappa\,B_f} \tag{7.65}$$

is the Monin-Obukhov length scale determined by the ratio of the momentum forcing to buoyancy forcing.

The Monin-Obukhov length scale takes on the following values for the suite of available boundary forcing

$$L = \begin{cases} 0 & u_* = 0, B_* \neq 0 \quad \tau = 0, B_f \neq 0 \quad \text{zero winds} \\ \infty & u_* \neq 0, B_* = 0 \quad \tau \neq 0, B_f = 0 \quad \text{zero buoyancy forcing (neutral forcing)} \\ > 0 & u_* \neq 0, B_* > 0 \quad \tau \neq 0, B_f > 0 \quad \text{stabilizing buoyancy forcing} \\ < 0 & u_* \neq 0, B_* < 0 \quad \tau \neq 0, B_f < 0 \quad \text{destabilizing or convective buoyancy forcing.} \end{cases} \tag{7.66}$$

Notably, L is *not* the finite positive thickness of the surface turbulent layer (Figure 7.1), as evident since L can be negative or infinite. Instead, L is the depth scale at which buoyancy production of turbulent kinetic energy is of the same magnitude as shear production. For depths shallower than $L > 0$, shear production dominates due to the effects from mechanical forcing through momentum stress τ. The case $L = \infty$ is trivially dominated by shear production since there is no buoyancy forcing. For depths deeper than L, buoyancy production dominates the turbulence. The case of $L < 0$ (convection) is always dominated by buoyancy production.

The similarity function ϕ_Λ appearing in equation (7.62) satisfies the following limit case under neutral forcing (zero buoyancy forcing)

$$\phi_\Lambda(0) = 1 \qquad \text{arising from } B_f = 0 \text{ so that } L = \infty \text{ and } \zeta = d/L = 0. \tag{7.67}$$

This limit reduces the more general Monin-Obukhov form for the vertical derivative (7.62) to the logarithmic Law of the Wall form

$$\frac{\partial \Lambda}{\partial z} = \left(\frac{\Lambda_*}{\kappa\, d}\right) \qquad \text{neutral forcing so } \phi_\Lambda = 1. \tag{7.68}$$

In the general case of nonzero buoyancy forcing, we integrate the similarity form (7.62) to expose the logrithmic Law of the Wall for neutral forcing, plus a term present with nonzero buoyancy forcing. For this purpose, rewrite equation (7.62) in terms of the scaled Monin-Obukhov distance, ζ, to have

$$\frac{\partial \Lambda}{\partial \zeta} = -\left(\frac{\Lambda_*}{\kappa\, \zeta}\right) \phi_\Lambda(\zeta), \tag{7.69}$$

where we used the relation between vertical increments through

$$\mathrm{d}\zeta = -L\, \mathrm{d}z \tag{7.70}$$

using $d = -z + \eta$ (equation (7.10)). We now vertically integrate equation (7.69) to have

$$\Lambda(\zeta) = \Lambda(Z_\lambda/L) + \left(\frac{\Lambda_*}{L}\right) \int_{Z_\lambda/L}^{\zeta} \left(\frac{(1 - \phi_\Lambda) - 1}{\zeta'}\right) \mathrm{d}\zeta'. \tag{7.71}$$

In this expression,

$$Z_\lambda = \text{roughness length} \tag{7.72}$$

introduced the roughness length associated with each fluctuating field. Within a distance Z_λ or less from the boundary at $z = \eta$, the kinematic fluxes are not expected to be constant due to the impacts from roughness elements. Hence, we expect the Monin-Obukhov similarity theory to breakdown when getting closer than the roughness length to the surface.

Integrating the right hand side of equation (7.71) from the roughness length to an arbitrary point within the surface layer renders[1]

$$\Lambda(\zeta) = \Lambda(Z_\lambda/L) - \left(\frac{\Lambda_*}{L}\right) \ln(\zeta\, L/Z_\lambda) + \left(\frac{\Lambda_*}{L}\right) \int_{Z_\lambda/L}^{\zeta} \left(\frac{(1 - \phi_\Lambda)}{\zeta'}\right) \mathrm{d}\zeta'. \tag{7.73}$$

As expected, the first term exposes the logarithmic Law of the Wall behaviour occurring for neutral forcing conditions ($\phi_\Lambda = 1$). Deviations from Law of the Wall for non-neutral forcing are embodied in the integral on the right hand side. Recall that values $\zeta < Z_\lambda/L$ are within the roughness elements or molecular sublayer, so the theory cannot be applied there.

Large et al. (1994) (see their page 365) use atmospheric boundary layer results from Tennekes (1973) to set the surface layer thickness to (see Figure 7.1)

$$\epsilon = 0.1 \qquad \text{fraction of KPP boundary layer occupied by surface layer.} \tag{7.74}$$

---

[1]The result (7.73) disagrees with equation (4) in Large et al. (1994) by a minus sign, with the origin of the minus sign the relation (7.70) between infinitesimal changes in ζ and infinitesimal changes in z.

Within the surface layer, atmospheric boundary layer studies indicate that turbulent fluxes are within 20% of their surface values when reaching a distance $d = \epsilon h$ from the upper ocean interface at $d = 0$. The value of $\epsilon = 0.1$ has never been observed in the ocean, but there is no reason to believe it is fundamentally incorrect. Hence, this is the value taken for the KPP scheme.

7.5   Specifying the KPP parameterization

We are now ready to determine the KPP boundary layer depth, h, the diffusivity, K_λ, and non-local transport, γ_λ, thus enabling a full parameterization of the turbulent flux $\overline{w\,\lambda}$ according to

$$\overline{w\,\lambda} = -K_\lambda\left(\frac{\partial \Lambda}{\partial z} - \gamma_\lambda\right), \tag{7.75}$$

where the diffusivity is given by equation (7.7), rewritten here as

$$K_\lambda(\sigma) = h\,w_\lambda(\sigma)\,G_\lambda(\sigma). \tag{7.76}$$

Recall that

$$\sigma = d/h \tag{7.77}$$

is the dimensionless distance from the upper surface normalized by the boundary layer thickness, with

$$d = -z + \eta \tag{7.78}$$

the dimensionful distance.

7.5.1   The turbulent vertical velocity scale w_λ

We now determine the turbulent vertical velocity scale w_λ appearing in equation (7.76).

7.5.1.1   Velocity scale with stable buoyancy forcing

Following page 370 of Large et al. (1994), we first specify the velocity scale within the Monin-Obukhov surface layer, where $\sigma = d/h < \epsilon = 0.1$. We also assume stable buoyancy forcing, so that the non-local term, γ_λ, vanishes. We later extend these results to the full boundary layer for arbitrary buoyancy forcing.

The similarity result (7.62) holds in the surface layer, in which

$$\frac{\partial \Lambda}{\partial z} = \left(\frac{\Lambda_*}{\kappa\,d}\right)\phi_\Lambda(\zeta). \tag{7.79}$$

We may eliminate the vertical gradient $\partial\Lambda/\partial z$ using the KPP parameterization (7.75) with a zero non-local term under stable buoyancy forcing

$$\phi_\Lambda = -\frac{\kappa\,d}{\Lambda_*}\left(\frac{\overline{w\,\lambda}}{K_\lambda}\right). \tag{7.80}$$

Substituting the turbulent scale $\Lambda_* = -\overline{w\,\lambda}^\eta/u_*$ from equation (7.59) yields

$$K_\lambda\,\phi_\Lambda = \kappa\,d\,u_*\left(\frac{\overline{w\,\lambda}}{\overline{w\,\lambda}^\eta}\right). \tag{7.81}$$

The KPP diffusivity expression (7.76) then renders

$$w_\lambda(\sigma)\,\sigma^{-1}\,G_\lambda(\sigma) = \left(\frac{\kappa\,u_*}{\phi_\Lambda(\sigma)}\right)\left(\frac{\overline{w\,\lambda}^\sigma}{\overline{w\,\lambda}^\eta}\right). \tag{7.82}$$

Recalling that $\sigma < \epsilon = 0.1$ in the surface layer yields the approximate linear relation

$$\sigma^{-1}\,G_\lambda(\sigma) \approx a_1 + a_2\,\sigma, \tag{7.83}$$

where we used expression (7.13) for the structure function $G_\lambda(\sigma)$. Furthermore, within the surface layer, turbulent fluxes for any fluctuating field, $\overline{w\,\lambda}^\sigma$, are linearly proportional to their surface value, $\overline{w\,\lambda}^\eta$. We may thus use this result to specify a part of the structure function according to

$$a_1 + a_2\,\sigma = \left(\frac{\overline{w\,\lambda}^\sigma}{\overline{w\,\lambda}^\eta}\right). \tag{7.84}$$

Note that as shown in Section 7.5.3, there is generally a dependence of a_2 on the field λ, whereas a_1 is unity for all fields. With the specification (7.84), we are led to an expression for the turbulent velocity scale within the surface layer

$$w_\lambda(\sigma) = \frac{\kappa\,u_*}{\phi_\Lambda(\sigma\,h/L)} \qquad \text{for stable forcing } B_f > 0 \text{ and } 0 < \sigma < \epsilon. \tag{7.85}$$

Troen and Mahrt (1986) assume this expression is valid throughout the stably forced boundary layer for $0 < \sigma < 1$, and Large et al. (1994) also make that assumption.

7.5.1.2 Velocity scale with unstable buoyancy forcing

For unstable buoyancy forcing conditions, $B_f < 0$, the turbulent velocity scales within the surface layer are assumed to be the same as the stable velocity scale (7.85), again within the surface layer. For unstable forcing beneath the surface layer, $\epsilon < \sigma < 1$, Large et al. (1994) cap the velocity scale to that evaluated at the base of the surface layer at $\sigma = \epsilon$.

7.5.1.3 Summarizing properties of the turbulent velocity scale

The net result for all conditions is that the turbulent vertical velocity scale is given by

$$w_\lambda(\sigma) = \kappa\,u_* \begin{cases} \phi_\Lambda^{-1}(\sigma\,h/L) & \text{stable forcing } B_f > 0 & \text{OBL} & 0 < \sigma < 1 \\ \phi_\Lambda^{-1}(\sigma\,h/L) & \text{unstable forcing } B_f < 0 & \text{surface layer} & \sigma < \epsilon \\ \phi_\Lambda^{-1}(\epsilon\,h/L) & \text{unstable forcing } B_f < 0 & \text{OBL beneath surface layer} & \epsilon < \sigma < 1. \end{cases} \tag{7.86}$$

We now summarize various properties of the velocity scale, with these properties reflected in Figure 7.3.

- STABLE FORCING: The similarity functions ϕ_Λ and velocity scales w_λ satisfy the following properties under positive buoyancy forcing, $B_f > 0$.

    - The similarity functions are increased so that the turbulent velocity scales are reduced.
    - The similarity functions are the same for all scalars and momentum, so that the velocity scales w_λ are the same.

- NEUTRAL FORCING: with zero buoyancy forcing, $B_f = 0$, the similarity functions satisfy $\phi_\Lambda = 1$, so that $w_\lambda(\sigma) = \kappa\,u_*$.

- UNSTABLE FORCING: The similarity functions ϕ_Λ and velocity scales w_λ satisfy the following properties under negative buoyancy forcing, $B_f < 0$.

    - The similarity functions ϕ_Λ are reduced so that the turbulent velocity scales w_λ are enhanced.
    - The similarity functions for momentum are larger than those for scalars, so that the velocity scales for momentum are smaller than for scalars: $w_m < w_s$.
    - In the convective limit, for which $u_* \to 0$, the velocity scales behave according to

    $$w_\lambda \sim w_* = (-B_f\,h)^{1/3}. \tag{7.87}$$

    In order to satisfy this scaling, the similarity functions ϕ_Λ must have the form

    $$\phi_\Lambda = (a_\lambda - c_\lambda\,\zeta)^{-1/3} \qquad \text{convective conditions with } u_* \to 0, \tag{7.88}$$

where $\zeta = d/L \ll 0$, and the constants a_λ and c_λ are chosen to match the convective form (7.88) to less unstable forms.

We now use the expression (7.88) within the unstable surface layer ($\sigma < \epsilon$) form in (7.86) to render

$$
\begin{aligned}
w_\lambda &= \kappa \, (a_\lambda \, u_*^3 - c_\lambda \, u_*^3 \, \zeta)^{1/3} \\
&= \kappa \, [a_\lambda \, u_*^3 - c_\lambda \, u_*^3 \, (h\,\sigma/L)]^{1/3} \\
&= \kappa \, (a_\lambda \, u_*^3 - c_\lambda \, \sigma \, \kappa \, h \, B_f)^{1/3} \\
&= \kappa \, (a_\lambda \, u_*^3 + c_\lambda \, \sigma \, \kappa \, w_*^3)^{1/3} \\
&\to \kappa \, w_* \, (c_\lambda \, \sigma \, \kappa)^{1/3},
\end{aligned}
\tag{7.89}
$$

where the final limit case is for the convective limit with $u_* \to 0$. Likewise, outside the surface layer ($\epsilon < \sigma < 1$) we have

$$
w_\lambda = \kappa \, (a_\lambda \, u_*^3 + c_\lambda \, \epsilon \, \kappa \, w_*^3)^{1/3} \to \kappa \, w_* \, (c_\lambda \, \epsilon \, \kappa)^{1/3},
\tag{7.90}
$$

where again the final limit case is for the convective limit with $u_* \to 0$.

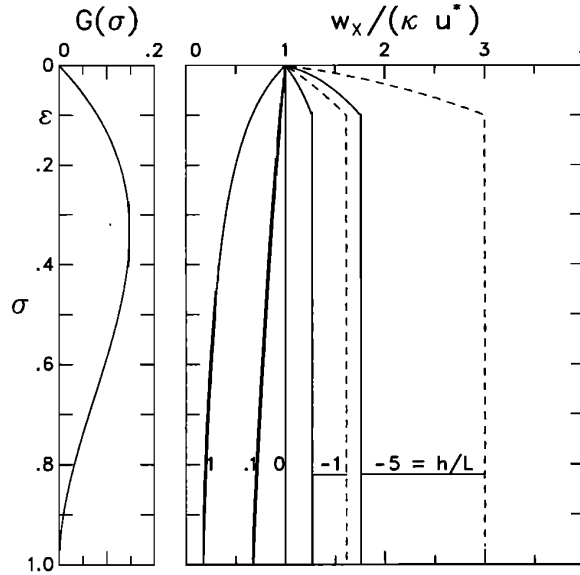
Figure 7.3: This is a reproduction of Figure 2 from Large et al. (1994). The vertical axis is the dimensionless vertical coordinate $\sigma = d/h$ within the KPP boundary layer $0 \le \sigma \le 1$. The left panel shows the vertical profile of the shape or structure function, $G_\lambda(\sigma)$, used to scale the vertical diffusivity via equation (7.76). The analytic form shown here is given by $G_\lambda(\sigma) = \sigma \, (1 - \sigma)^2$, which corresponds to the Troen and Mahrt (1986) form and which is independent of the quantity Λ being diffused. Large et al. (1994) chose a more general form, based on the need to match boundary layer diffusivities to interior diffusivities in which case the shape function becomes a function of λ. We detail this approach in Section 7.5.3. The right panel shows various examples of the normalized turbulent velocity scale w_λ (called w_x in Large et al. (1994)), with the examples differing by the value of the dimensionless ratio h/L between the boundary layer depth, h, and the Monin-Obukhov length scale L. For unstable buoyancy forcing, $L < 0$, the velocity scale for scalars, w_s (dashed lines), is greater than that for momentum, w_m (solid lines). For stable forcing, $L > 0$, and both scalar and momentum have the same turbulent velocity scales, $w_s = w_m$. In general, the turbulent velocity scale is enhanced with unstable surface buoyancy forcing, and reduced with stable buoyancy forcing.

7.5.2   Similarity functions ϕ_Λ

The vertical velocity scales are functions of the similarity functions ϕ_Λ, also called the dimensionless flux profiles. Appendix B of Large et al. (1994) present analytic forms for these functions, based on fits to available data, with their Figure B1 (reproduced here as Figure 7.4) providing a summary of the choices for the momentum function ϕ_m and the scalar function ϕ_s. Both functions agree for stable buoyancy forcing, and they depend linearly on the dimensionless Monin-Obukhov length $\zeta = d/L = \sigma\, h/L$.

7.5.2.1   The Large et al. (1994) choices for unstable buoyancy forcing

For unstable buoyancy forcing, where $L < 0$ and so $\zeta < 0$, there are two regimes. The scalar function ϕ_s is always less than the momentum function ϕ_m. Hence, for unstable forcing there is a larger turbulent velocity scale for the scalars than momentum, and thus a larger vertical diffusivity for scalars. The turbulent Prandtl number, Pr, is given by the ratio of the flux functions

$$Pr = K_m/K_s = w_m/w_s = \phi_m/\phi_s. \tag{7.91}$$

The choices made by Large et al. (1994) lead to a Prandtl number in the convective limit ($\zeta \to -\infty$) of

$$Pr \to (c_m/c_s)^{1/3} = 0.44, \tag{7.92}$$

where c_m and c_s are parameters in the similarity functions ϕ_m and ϕ_s, respectively.

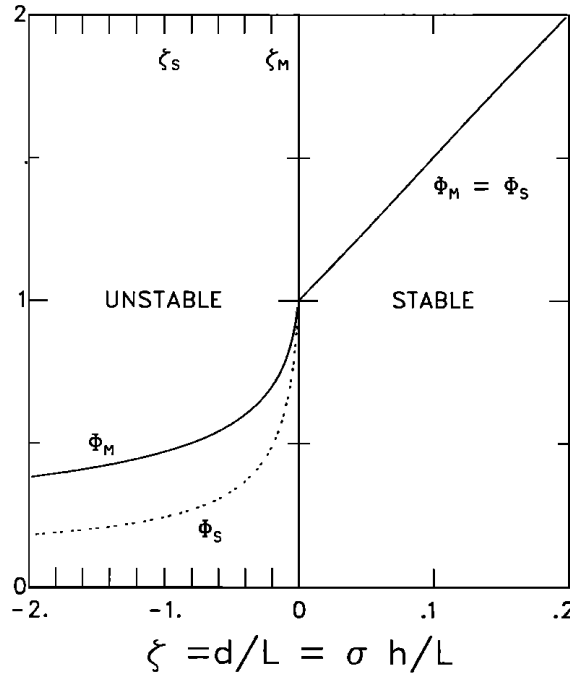Figure 7.4: This is a reproduction of Figure B1 from Large et al. (1994). The vertical axis provides values for the dimensionless flux profiles, ϕ_Λ, for momentum and scalars, and the horizontal axis gives the dimensionless Monin-Obukhov length scale $\zeta = d/L = \sigma\, h/L$. There is a transition across the neutrally forced value of $\zeta = 0$. For stable buoyancy forcing ($\zeta > 0$), both functions are the same, $\phi_s = \phi_m$, and are linear functions of ζ. For unstable buoyancy forcing ($\zeta < 0$), the scalar function is less than momentum, $\phi_s < \phi_m$, with both functions falling off with a negative fractional power. The analytic forms for the functions are given by equations (B1) and (B2) in Large et al. (1994).

7.5.2.2 Alternative choices for unstable buoyancy forcing

Large et al. (1994) chose two regimes for the unstable buoyancy forced range, transitioning from different fractional exponents near $\zeta = 0$, to the same $-1/3$ power for larger negative ζ. The scalar function ϕ_s falls off faster near $\zeta = 0$, with a power $-1/2$, whereas the momentum function ϕ_m falls off with a $-1/4$ power. This initial distinct fractional power falloff sets the scale for the Prandtl number in this portion of ζ in the weakly unstable regime.

Having two regimes for the negative buoyancy forcing adds complexity to the algorithm. We thus consider how well the original two-regime forms for ϕ_m and ϕ_s can be fit using a single regime, using only the fractional power $-1/3$. Tests suggest that the following forms may be suitable

$$\phi_m(\zeta) = \begin{cases} 1 + 5\zeta & \zeta > 0 \\ (1 - 9\zeta)^{-1/3} & \zeta < 0 \end{cases} \tag{7.93}$$

$$\phi_s(\zeta) = \begin{cases} 1 + 5\zeta & \zeta > 0 \\ (1 - 60\zeta)^{-1/3} & \zeta < 0. \end{cases} \tag{7.94}$$

A comparison of the original forms from Large et al. (1994) to the alternative forms is shown in Figure 7.5. Also shown is the ratio of these two functions which yields the turbulent Prandtl number according to equation (7.91). The agreement between the original forms and the new forms is worse when considering the Prandtl number. As discussed in the figure caption, a viable means for simplifying the turbulent functions, without compromising much on the values used in Large et al. (1994), is to maintain original 3-region ϕ_s form, but to simplify ϕ_m to 2-regions according to equation (7.93).

7.5.3 The shape function $G_\lambda(\sigma)$

The vertical shape function $G_\lambda(\sigma)$ is given by the cubic polynomial

$$G_\lambda(\sigma) = a_0 + a_1\,\sigma + a_2\,\sigma^2 + a_3\,\sigma^3. \tag{7.95}$$

As already noted when introducing this cubic expression (equation (7.13)), turbulent eddies do not cross the ocean surface at $\sigma = 0$, so the diffusivity should vanish at $\sigma = 0$. This constraint is satisfied by setting

$$a_0 = 0. \tag{7.96}$$

We now discuss further constraints to specify the remaining coefficients.

We start by rewriting the expression (7.84) that expresses the ratio of turbulent fluxes within the surface layer to those at the surface boundary

$$a_1 + a_2\,\sigma = \left(\frac{\overline{w\,\lambda}^\sigma}{\overline{w\,\lambda}^\eta} \right) \qquad \text{surface layer: } 0 \leq \sigma \leq \epsilon. \tag{7.97}$$

Satisfying this relation at the ocean surface, $\sigma = 0$, requires

$$a_1 = 1, \tag{7.98}$$

so that

$$1 + a_2\,\sigma = \left(\frac{\overline{w\,\lambda}^\sigma}{\overline{w\,\lambda}^\eta} \right) \qquad \text{surface layer: } 0 \leq \sigma \leq \epsilon. \tag{7.99}$$

Now define the ratio

$$\beta_\lambda = \left(\frac{\overline{w\,\lambda}^\epsilon}{\overline{w\,\lambda}^\eta} \right), \tag{7.100}$$

which is the ratio of the turbulent flux at the base of the surface layer, $\sigma = \epsilon$, to the flux at the upper ocean interface, $z = \eta$. For atmospheric boundary layers, Troen and Mahrt (1986) set

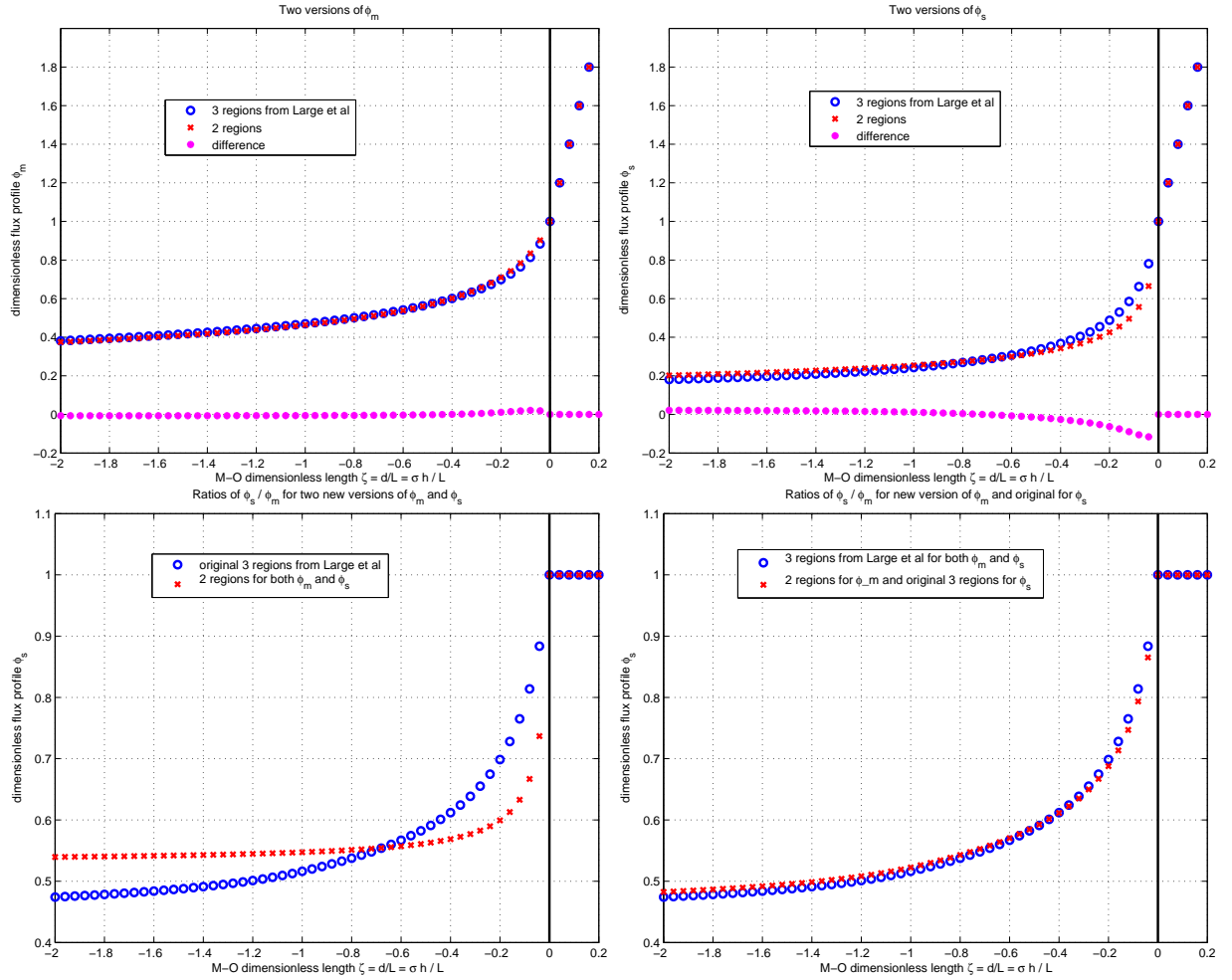$$\beta_\lambda = 2\,\epsilon \qquad \text{atmospheric boundary layers,} \tag{7.101}$$

Figure 7.5: Shown here are 2-region flux profiles given by equations (7.93) and (7.94) as compared to the original 3-region profiles rom Large et al. (1994). We also show the ratio, ϕ_s/ϕ_m, which defines the turbulent Prandtl number or the ratio of the vertical momentum viscosity to vertical tracer diffusivity. The top left panel shows the original 3-region ϕ_m as compared to the 2-region form (7.93). The agreement is quite close. The top right panel shows the comparison for ϕ_s, with the agreement not very good. The lower left panel shows the ratio ϕ_s/ϕ_m for the original 3-region functions and the new 2-region functions. Their ratio amplifies the problems with the new ϕ_s form (7.94). The lower right panel shows the ratio of the original 3-region ϕ_s to the new 2-region form of ϕ_m. These results suggest that to remain consistent with the original Large et al. (1994) results, it is feasible to switch to the 2-region form (7.93) for ϕ_m, but we must maintain the original 3-region form of ϕ_s.

with $\epsilon = 0.1$. Troen and Mahrt (1986) further assume both the shape function and its first derivative vanish at the base of the boundary layer, $\sigma = 1$. These assumptions lead to the cubic expression valid for all fluctuating fields λ

$$G(\sigma) = \sigma\,(1 - \sigma)^2 \qquad \text{atmospheric boundary layers,} \qquad (7.102)$$

with this function exhibited in the left panel of Figure 7.3.

Large et al. (1994) also assume the surface layer is 10% of the boundary layer, so that

$$\epsilon = 0.1 \qquad \text{KPP scheme.} \qquad (7.103)$$

However, they consider a more general approach for the remaining approach to deriving the shape function. The key reason to generalize the atmospheric approach of Troen and Mahrt (1986) is to admit the

possibility of ocean boundary layer turbulence to be impacted by interior mixing, with this mixing parameterized by downgradient vertical diffusion. Such diffusion generally introduces distinct diffusivities for tracers (e.g., double diffusion) as well as for momentum (e.g., non-unit Prandtl number). For these reasons, Large et al. (1994) insist that both the diffusivity and its vertical derivative match across the base of the boundary layer at $\sigma = 1$. This matching condition leads to the constraints (18) given by Large et al. (1994), which in turn leads to shape functions that are dependent on the field being transported.

Matching both the shape function and its vertical derivative across the boundary layer base adds complexity to the KPP algorithm. Furthermore, it is unclear how accurate one can in fact satisfy both matching conditions on a finite grid with potentially coarse vertical grid spacing at the boundary layer base. To simplify the KPP algorithm, we drop the need to match the vertical derivative of the diffusivity. Instead, we assume continuity of the diffusivity with a vanishing derivative at the boundary layer base, $\sigma = 1$. Setting $\partial_\sigma G(\sigma) = 0$ at $\sigma = 1$ leads to the relation

$$3\,a_3 = -(1 + 2\,a_2). \tag{7.104}$$

Matching diffusivities at $\sigma = 1$ between the boundary layer and interior value leads to

$$a_2 = -2 + \left(\frac{3\,K_\lambda(h)}{h\,w_\lambda(h)} \right), \tag{7.105}$$

where the diffusivity $K_\lambda(h)$ is determined by parameterizations of interior mixing. Substituting this expression for a_2 into equation (7.104) for a_3 leads to

$$a_3 = 1 - \left(\frac{2\,K_\lambda(h)}{h\,w_\lambda(h)} \right). \tag{7.106}$$

Allowing for the interior mixing to influence the KPP boundary layer scheme suggests that the KPP calculation should be called *after* the various methods used to compute interior diffusivities.

7.5.4   The non-local transport γ_λ

We now consider the parameterization for the non-local transport (see Section 7.1.4) as suggested by Large et al. (1994). Again, the KPP parameterization takes the form (equation (7.3))

$$\overline{w\,\lambda} = -K_\lambda \left(\frac{\partial \Lambda}{\partial z} - \gamma_\lambda \right), \tag{7.107}$$

so that that non-local portion of the turbulent flux is parameterized according to

$$\overline{w\,\lambda}^{\text{non-local}} = K_\lambda\,\gamma_\lambda, \tag{7.108}$$

where K_λ takes the form in equation (7.76):

$$K_\lambda(\sigma) = h\,w_\lambda(\sigma)\,G_\lambda(\sigma). \tag{7.109}$$

For completeness, we repeat elements of the outline presented in Section 7.1.4.

7.5.4.1   General features of γ_λ with the KPP parameterization

- Smyth et al. (2002) consider a non-local term for momentum. Until their ideas have been fully tested in climate models, we follow recommendations from (Large et al., 1994), who set the non-local momentum transport to zero:

$$\gamma_\lambda = \begin{cases} 0 & \text{if } \lambda = (u, v, w) \text{ a velocity component} \\ \neq 0 & \text{nonzero if } \lambda = \theta, s \text{ or another tracer.} \end{cases} \tag{7.110}$$

- The non-local transport is non-zero only within the OBL:

$$\gamma_\lambda = \begin{cases} 0 & \text{if } \sigma > 1 \\ \neq 0 & \text{if } 0 \leq \sigma \leq 1. \end{cases} \tag{7.111}$$

- The non-local transport is non-zero only in the presence of destabilizing negative surface ocean buoyancy flux:

$$\gamma_\lambda = \begin{cases} 0 & \text{for } B_f > 0 \\ \neq 0 & \text{for } B_f < 0. \end{cases} \tag{7.112}$$

- The non-local transport for temperature and arbitrary scalars is given by the following form for destabilizing negative surface ocean buoyancy fluxes:

$$\gamma_\theta = C_s \left(\frac{\overline{w\theta}^\eta - Q_R/(\rho_0 \, C_p)}{h \, w_\theta(\sigma)} \right) \tag{7.113}$$

$$\gamma_s = C_s \left(\frac{\overline{ws}^\eta}{h \, w_s(\sigma)} \right), \tag{7.114}$$

where

$$C_s = C_* \, \kappa \, (c_s \, \kappa \, \epsilon)^{1/3}, \tag{7.115}$$

with

$$C_* = 10, \tag{7.116}$$

and Q_R is the heat flux from penetrative radiation given by equation (7.51).

Combining the parameterizations (7.113) and (7.114) for the non-local term γ_λ, with that for the vertical diffusivity K_λ in equation (7.109) renders the non-local flux parameterization in the form

$$\overline{w\theta}^{\text{non-local}} = K_\theta \, \gamma_\theta = G_\lambda(\sigma) \, C_s \left(\overline{w\theta}^\eta - Q_R/(\rho_0 \, C_p) \right) \tag{7.117}$$

$$\overline{ws}^{\text{non-local}} = K_s \, \gamma_s = G_s(\sigma) \, C_s \, (\overline{ws}^\eta). \tag{7.118}$$

Notice how explicit dependence on both the turbulent velocity scale, w_λ, and boundary layer depth, h, drop out from the parameterization of the non-local flux.

7.5.4.2 Potential problems with the parameterized non-local transport

Experience has shown that there are cases when the parameteried non-local flux, (7.117) of (7.118), can produce values larger than the surface flux. That is, one may realize cases when

$$G_\lambda(\sigma) \, C_s > 1 \qquad \text{non-local flux greater than surface flux.} \tag{7.119}$$

This situation arises particularly near the boundary layer base, $\sigma = 1$, when the interior diffusivity is large. The matching conditions employed by Large et al. (1994) (Section 7.5.3) then lead to a very large value for the shape function $G(\sigma)$. In this case, one may be exposed to the production of extrema in the tracer field. In the presence of sea-ice, problems may arise particularly in fresh water regions such as the Baltic Sea where the thermal expansion coefficient is negative, $\alpha < 0$ (Martin Schmidt, personal communication).

The following modifications to the original Large et al. (1994) scheme have been found useful to reduce the potential for the non-local term to be problematic.

- INTERIOR GRAVITATIONAL INSTABILITIES: When the vertical stratification is unstable ($N^2 < 0$), vertical diffusivity is enhanced to remove the gravitational instability. Notably, it is *not* appropriate to enhance the diffusivity within the KPP boundary layer, beyond that already computed via the KPP scheme, even when $N^2 < 0$. On those occasions when the instabilities appear beneath the boundary layer, diffusivities are enhanced. If one insisted that such diffusivities should match those in the boundary layer, then the shape function $G(\sigma)$ would indeed become quite large in magnitude. Hence, NCAR recommends that one pull the "convective adjustment" portion of the mixing scheme outside of the KPP portion of the algorithm. That is, the interior convective instability diffusivities are *not* matched to the KPP boundary layer diffusivities.

- SIMPLER MATCHING: As noted in Section 7.5.3, we propose to simplify the matching at the boundary layer base, so that only the diffusivities match across the boundary layer base, rather than also insisting on the derivative of the diffusivities as proposed by Large et al. (1994). The simplified matching condition leads to less problems computing discrete vertical derivatives of the diffusivities, and in turn produces more well regularized diffusivities and shape functions.

7.5.5 Bulk Richardson number and the OBL thickness

Large et al. (1994) define the KPP boundary layer depth to be an interpolation to the depth at which the bulk Richardson number, Ri_b, equals to a critical Richardson number, Ri_c. Smaller values for Ri_b, including negative values, signal that we are still in the boundary layer, whereas larger values are beneath. The critical value Ri_c sets a threshold for upper ocean mixing, with such enabling behaviour that is sensitive to its precise value.

The bulk Richardson number is a non-local version of the gradient Richardson number defined in Section 2.3. It aims to measure the ability of an upper ocean eddy, with buoyancy set by values of temperature and salinity in the surface layer (Figure 7.1), to move downward in the water column, overcoming the resistence from stratification and aided by both resolved and unresolved vertical shear. Presumably at some point, such boundary layer eddies will be suppressed by the reduced shear and increased buoyancy stratification present below the boundary layer.

Using the notation from Large et al. (1994), we may write the bulk Richardson number at a distance d from the ocean surface in the form

$$\mathrm{Ri}_b(d) = \frac{d\,[B_r - B(d)]}{|\mathbf{U}_r - \mathbf{U}(d)|^2 + U_t^2}. \tag{7.120}$$

This calculation makes use of the surface layer averaged buoyancy, B_r, and surface layer averaged horizontal velocity, $\mathbf{U}_r$, where the surface layer is defined by $0 \leq \sigma \leq \epsilon$ (Figure 7.1). The term U_t^2 is associated with parameterized unresolved vertical shears that may act to further reduce the bulk Richardson number.

Using notation introduced in the local gravitational stability calculation from Section 2.2, we write the bulk Richardson number in the form

$$\mathrm{Ri}_b(d) = \left(\frac{d\,g}{\rho_o}\right)\left(\frac{\rho[\Theta(d), S(d), p(d)] - \rho[\Theta_r, S_r, p(d)]}{|\mathbf{U}_r - \mathbf{U}(d)|^2 + U_t^2}\right). \tag{7.121}$$

The density $\rho[\Theta(d), S(d), p(d)]$ is the *in situ* value at a distance d from the surface. The density $\rho[\Theta_r, S_r, p(d)]$ is based on an adiabatic and isohaline displacement from the surface layer to the depth d. Now consider three cases to expose the physics of the bulk Richardson number.

- SURFACE EDDY HAS NEGATIVE RELATIVE BUOYANCY: If the density $\rho[\Theta_r, S_r, p(d)]$ is greater than the *in situ* density, $\rho[\Theta(d), S(d), p(d)]$, then a surface layer parcel can move downwards and the boundary layer based has yet to be reached. That is, the surface layer parcel has negative buoyancy relative to the ambient fluid. This situation leads to a negative bulk Richardson number, in which case the criteria $\mathrm{Ri}_b(d) > \mathrm{Ri}_c$ has not yet been reached.

- SURFACE EDDY HAS POSITIVE RELATIVE BUOYANCY AND AMBIENT FLUID HAS STRONG SHEARS: If the density $\rho[\Theta_r, S_r, p(d)]$ is less than the *in situ* density, a surface layer eddy has positive buoyancy relative to the ambient fluid. However, if the vertical shear is large, then the bulk Richardson number can still be less than the critical value, in which case mechanically induced mixing is still large and the boundary layer base has yet to be reached.

- SURFACE EDDY HAS POSITIVE RELATIVE BUOYANCY AND AMBIENT FLUID HAS WEAK SHEARS: Finally, if a surface eddy has positive relative buoyancy and the ambient fluid has weak shears, then at some point the bulk Richardson number will become larger than the critical value. Interpolating to where that cross-over occurs determines the boundary layer thickness h.

7.5.5.1 Non-local gravitational stability

Section 2.2 presents a general discussion of local gravitational stability. Much of that material is useful for the purpose of determining gravitational stability for parcels that are a finite distance from one another. However, there is one aspect of the discussion in Section 2.2 that differs from the present considerations. Namely, we are here always considering downward displacements of parcels from the surface layer. The reason is that we are concerned with parcels starting from the surface layer moving downwards in an adiabatic and isohaline manner, with the difficulty of such motion determined by the ambient stratification
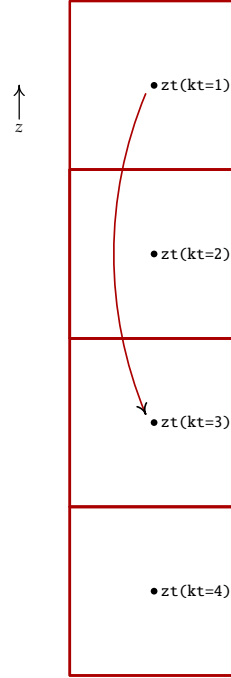
Figure 7.6: Schematic of the adiabatic and isohaline parcel displacement that is used to determine non-local gravitational stability for computing the bulk Richardson number according to equation (7.121). The reference temperature and salinity of this displaced parcel is set according to values determined in the surface layer, here approximated by the value at the top model grid cell with vertical position $\mathtt{zt(kt=1)}$. The density of this parcel is then computed using the surface layer temperature and salinity and the local *in situ* pressure. This displaced parcel's density is then compared to the ambient *in situ* density using the local temperature, salinity, and pressure. We illustrate that process by displacing the parcel to $\mathtt{zt(kt=3)}$. If the resulting bulk Richardson number is larger than the critical value, the base of the KPP boundary layer is at or shallower than $\mathtt{zt(kt=3)}$, with interpolation used to determine the KPP boundary layer thickness h. If the bulk Richarson number is less than the critical value, the boundary layer bottom has yet to be reached, so the downward search continues.

and shear. Figure 7.6 illustrates this situation. We are not interested in the complement movement of a deep parcel towards the surface.

The expression (7.121) presents a direct means for computing the non-local gravitational stability via the computation of the density difference, written here using discrete notation from Figure 7.6

$$\delta\rho[\mathtt{kt},r] = \rho[\Theta(\mathtt{kt}), S(\mathtt{kt}), p(\mathtt{kt}] - \rho[\Theta_r, S_r, p(\mathtt{kt})], \tag{7.122}$$

where the surface layer values Θ_r, S_r are typically approximated by the values as $\mathtt{kt}$ =1. This approximation breaks down for stable boundary layers with vertical grid spacing finer than roughly 2 m, in which case an averaging is required.

There is an alternative method to approximate $\delta\rho[\mathtt{kt},r]$ based on linear truncations of Taylor series expansions. The alternative leads to a sum of squared buoyancy frequencies, analogous to the expression (2.16). There are some advantages offered by the alternative approach, namely there are fewer calculations of the equation of state, assuming we already have the expansion coefficients α and β. However, the deeper the boundary layer, and the more nonlinear the equation of state, the less accurate the approximation becomes. We therefore recommend the more exact calculation based on the density differences in equation (7.122).

For completeness, we develop the alternative approach. For this purpose, consider a displacement from level $\mathtt{kt}$ = 1 to $\mathtt{kt}$ >1, in which we need to compute $\rho[\Theta(\mathtt{kt} = 1), S(\mathtt{kt} = 1), p(\mathtt{kt} > 1)]$. Truncating a Taylor

series at leading order yields

$$\rho[\Theta(1),S(1),p(\mathsf{kt}>1)] \approx \rho[\Theta(1),S(1),p(1)] - \sum_{n=1}^{\mathsf{kt}} \mathsf{dzw}(n+1) \left(\frac{\partial\rho}{\partial p}\frac{\partial p}{\partial z}\right)_{\mathsf{zt}(n)}. \tag{7.123}$$

A similar expression for the *in situ* density $\rho[\Theta(\mathsf{kt}),S(\mathsf{kt}),p(\mathsf{kt})]$

$$\rho[\Theta(\mathsf{kt}),S(\mathsf{kt}),p(\mathsf{kt})] \approx \rho[\Theta(1),S(1),p(1)] - \sum_{n=1}^{\mathsf{kt}} \mathsf{dzw}(n+1)\left(\frac{\partial\rho}{\partial p}\frac{\partial p}{\partial z}+\frac{\partial\rho}{\partial\Theta}\frac{\partial\Theta}{\partial z}+\frac{\partial\rho}{\partial S}\frac{\partial S}{\partial z}\right)_{\mathsf{zt}(n)}. \tag{7.124}$$

These results lead to the approximation

$$\begin{aligned}
\delta\rho[\mathsf{kt},r] &= \rho[\Theta(\mathsf{kt}),S(\mathsf{kt}),p(\mathsf{kt})] - \rho[\Theta_r,S_r,p(\mathsf{kt})]\\
&\approx -\sum_{n=1}^{\mathsf{kt}} \mathsf{dzw}(n+1)\left(\frac{\partial\rho}{\partial\Theta}\frac{\partial\Theta}{\partial z}+\frac{\partial\rho}{\partial S}\frac{\partial S}{\partial z}\right)_{\mathsf{zt}(n)}\\
&= \sum_{n=1}^{\mathsf{kt}} \mathsf{dzw}(n+1)\left(\rho\,\alpha\,\frac{\partial\Theta}{\partial z}-\rho\,\beta\,\frac{\partial S}{\partial z}\right)_{\mathsf{zt}(n)}\\
&= \frac{1}{g}\sum_{n=1}^{\mathsf{kt}} \mathsf{dzw}(n+1)\left(\rho\,N^2\right)_{\mathsf{zt}(n)}.
\end{aligned} \tag{7.125}$$

Again, this result is analogous to the approximate forms given in Section 2.2.3 for the local calculation of gravitational stability. For that calculation, it is sensible to drop the higher order terms in the Taylor series. However, for the non-local calculation considered here, one may in fact be compromising the determination of gravitational stability, particularly in regions of deep mixing in the high latitudes. We may also be compromising the ability of the KPP scheme to include thermobaric convection. We are thus reticent to recommend this approach, and instead prefer the original approach given by equation (7.121).

7.5.5.2 Unresolved shear U_t

The shear, U_t/d, in the bulk Richardson number (7.121) acknowledges the potential presence of unresolved shears that can impact on the boundary layer depth. Large et al. (1994) present an argument on page 372 that focuses on an unresolved shear that reduces to a desired form for the case of pure convection

$$U_t^2(d) = \frac{C_v\,(-\beta_T)^{1/2}}{\mathrm{Ri}_c\,\kappa^2}(c_s\,\epsilon)^{-1/2}\,d\,N\,w_s. \tag{7.126}$$

The constant C_v sets the buoyancy frequency at the entrainment depth, and its value is expected to be

$$1 < C_v < 2. \tag{7.127}$$

The constant c_s is part of the similarity functions discussed in Section 7.4.3. The constant β_T is discussed in the caption to Figure 7.2, and is represents the ratio of the buoyancy flux at the entrainment depth, h_e, to the buoyancy flux at the surface,

$$\overline{w\,b}^{d=h_e} = -\beta_T\,\overline{w\,b}^{d=0}, \tag{7.128}$$

with

$$\beta_T \approx 0.2 \tag{7.129}$$

an empirical result. The critical Richardson number, Ri_c, is used to determine when the boundary layer base is reached, in which case stratification and/or reduced shear lead to a bulk Richardson number larger than the critical value. Large et al. (1994) choose the value

$$\mathrm{Ri}_c = 0.3. \tag{7.130}$$

The dimensionless number ϵ determines the thickness of the surface layer as in Figure 7.1, with

$$\epsilon = 0.1 \tag{7.131}$$

chosen by Large et al. (1994).

It is notable that there are no surface gravity wave parameters in the specification of the unresolved shear. We have more to say on this topic in Section 7.6.

7.5.5.3   Restrictions on h under stable buoyancy forcing

Large et al. (1994) suggest on page 372 that for stable buoyancy forcing, $B_f > 0$, the boundary layer thickness, h, should be no larger than either the Monin-Obukhov length scale, L, or the Ekman length scale,

$$h_E = 0.7\, u_*/f, \tag{7.132}$$

with f the Coriolis parameter. The following reasons are noted to motivate these two restrictions.

- MONIN-OBUKHOV: At depths deeper than L, buoyancy stratification suppresses the mechanically forced turbulence, thus cutting off the boundary layer.

- EKMAN: The Ekman depth is the extent of the boundary layer in neutral stratification ($N^2 = 0$). With stable buoyancy forcing, $B_f > 0$, we then expect the boundary layer depth to be less than the Ekman depth. Note that Large et al. (1994) do not mention the origin of the 0.7 factor in equation (7.132).

As noted in Large et al. (1994) and Large and Gent (1999), the restriction based on the Monin-Obukhov has been dropped in the NCAR implementation of KPP, as it does not lead to favorable effects. Dropping this constraint is also supported by the results from Shchepetkin (2005) and Lemarié et al. (2012). Likewise, the constraint based on the Ekman depth is not used at NCAR, as little sensitivity was seen with its use. Hence, there are no restrictions for the maximum boundary layer depth under stable forcing imposed by the NCAR implementation of KPP. Such is the standard approach used in the CVMix implementation.

The key problem with the Monin-Obukhov length scale, L, relates to the question of how to include penetrative shortwave heating in the calculation of the buoyancy forcing, B_f (Section 7.3.10). Depending on the depth over which the penetrative heating is included (equation (7.50)), one can produce a positive Monin-Obukhov length (if including sufficient shortwave heating) or negative (if including less heating). Since there is no fundamental reason to choose a particular amount of the shortwave when considering the total buoyancy forcing, there is no compelling reason to enforce the L constraint on boundary layer thickness.

7.5.5.4   Noise in the boundary layer thickness

Experience in MOM, POP, and ROMS indicate that the KPP boundary layer thickness, h, can become quite noisy. Noise in the boundary layer thickness can translate into noise in the tracer fields within the boundary layer. Hence, it is common practice to apply a horizontal smoothing operator, such as a Laplacian, to h prior to its use in computing the diffusivity or non-local transport.

The horizontal smoothing of h poses an algorithmic problem for CVMix, since CVMix modules ideally know nothing about the horizontal grid. There are two possible options that may be considered.

- INTERMEDIATE h SENT BACK TO CALLING MODEL: One option is to compute h in CVMix; send it immediately back to the calling model for smoothing; then have the smoothed h used for further KPP computations such as the diffusivity and non-local term.

- USE PREVIOUS h: We compute the new value of h within a particular call to the CMVix-KPP module, and we send this unsmoothed h back to the calling model at the end of the CVMix-KPP module. But for computing the KPP diffusivities and non-local term within CVMix, we use the previous time step value h, with this earlier h having been smoothed by the calling model. This approach requires storing h in restart files, but that is easily handled by the calling model.

7.6 KPP with surface waves

Craig and Banner (1994) considered surface waves in a modification of the Mellor and Yamada (1982) 2.5 order turbulence scheme. Axell (2002) considered also Langmuir turbulence in the $k-\epsilon$ closure scheme. We consider here some issues related to introducing both waves and Langmuir turbulence in the KPP scheme.

The KPP formulation presented by Large et al. (1994) ignores surface waves and the associated breaking waves and Langmuir turbulence. The basis for KPP must be revisited in regions of waves, since waves modify the Monin-Obukhov similarity scalings (see Terray et al. (1996) for the case of breaking waves, and Section 2.2 of Sullivan and McWilliams (2010) for wave-driven winds). In the presence of waves, the ocean surface contains both breaking waves to enhance upper ocean mixing and dissipation; swell, which can modify the the atmospheric planetary boundary layer by providing momentum to lower atmospheric winds; and the coupling of Stokes drift to currents to produce Langmuir cells and associated turbulence (McWilliams et al., 1997a). These processes act in addition to and in interaction with the shear induced eddies and buoyant plumes traditionally considered as part of the KPP scheme. The modifications to KPP with waves represents a research project, with work from Belcher et al. (2012) a step towards this goal, in which they consider the regimes where winds are more or less important than Langmuir turbulence.

In this section, we identify some incremental steps that may be considered for modifying aspects of KPP to incorporate features of surface waves. Even with these more humble aspirations, there are many questions.

7.6.1 Modified budgets with Stokes velocity

Large eddy simulations that incorporate surface waves, such as those from McWilliams et al. (1997b), McWilliams and Sullivan (2001) and Sullivan et al. (2007), include a contribution in the momentum equation from the Stokes velocity on the Coriolis force as well as a vortex force. Additionally, the tracer equation includes advection from the Stokes velocity. Finally, the subgrid scale turbulent kinetic energy equation also includes advection by the Stokes velocity, as well as vertical shear of the Stokes velocity coupled to the subgrid scale stresses, thus acting as a source for turbulent kinetic energy. Mathematically, these terms take the form (see equations (4a), (4b) and (4c) from Sullivan and McWilliams (2010))

$$\frac{\partial \mathbf{v}}{\partial t} = \ldots - f\,\hat{\mathbf{z}} \wedge \mathbf{v}^{\text{stokes}} + \mathbf{v}^{\text{stokes}} \wedge \boldsymbol{\omega} \tag{7.133}$$

$$\frac{\partial C}{\partial t} = \ldots - \mathbf{v}^{\text{stokes}} \cdot \nabla C \tag{7.134}$$

$$\frac{\partial E}{\partial t} = \ldots - \mathbf{v}^{\text{stokes}} \cdot \nabla E - \tau_{i3}\frac{\partial v_i^{\text{stokes}}}{\partial x_3} \tag{7.135}$$

where $\mathbf{v}$ is the velocity field (u, v, w) resolved by the LES, $\boldsymbol{\omega} = \nabla \wedge \mathbf{v}$ is the vorticity, $\mathbf{v}^{\text{stokes}}$ is the Stokes velocity due to wave motions, C is an arbitrary tracer concentration, E is the turbulent kinetic energy, and τ_{ij} is the deviatoric subgrid-scale stress tensor. The dots denote standard terms such as pressure gradients, friction, etc.

The question arises as to whether a hydrostatic primitive equation should also modify the prognostic equations for momentum and tracer in a manner emulating that done for the LES. We offer the following reasons to *not* do so.

- In present applications with hydrostatic primitive equation ocean models, a wave model provides information about the Stokes velocity, or an estimate of this velocity is made based on wind stress (Li and Garrett, 1993). However, there is no feedback to the waves from the circulation. Indeed, there is no such feedback considered in the LES studies from McWilliams et al. (1997b), McWilliams and Sullivan (2001) and Sullivan et al. (2007). For the primitive equation models used for climate research, it would be problematic to have a quiescent Eulerian mean flow impacted by a wave to thus initiate inertial circulations. In fact, it is the Stokes circulation itself that should be impacted.

- The Stokes circulation velocity, $\mathbf{v}^{\text{stokes}}$, is generally considered to have only horizontal components

$$\mathbf{v}^{\text{stokes}} = (u^{\text{stokes}}, v^{\text{stokes}}, 0) \tag{7.136}$$

These components are horizontally divergent. Hence, their presence in the flux-form tracer equation appears both as an advection plus a source term.

- As discussed by Rascle et al. (2006), ensemble averaging of these equations eliminates the added vortex force term.

- There are cases where the large-scale Eulerian mean flow in an LES will compensate for the Stokes flow, leading to a vanishing Lagrangian mean velocity. This balance cannot be represented in a primitive equation ocean model, so the selective introduction of only a piece of the full dynamics can lead to spurious effects.

In conclusion, introduction of the Stokes velocity into the tracer and momentum equations of a hydrostatic primitive equation ocean model is *not* recommended.

7.6.2   Modifications from Stokes velocity and Langmuir turbulence

- It is conjectured that the most important change to KPP may arise from enhanced shear due to Stokes velocity when computing bulk Richardson number (Section 7.5.5). We must be careful to note that in some cases, a piece of the Eulerian and Stokes velocities in fact cancel, leaving only a residual velocity whose vertical shear impacts the bulk Richardson number. However, this result needs some care to distinguish the potential for this effect to occur on the larger scaled represented in a primitive equation model. Note that for some reason, Smyth et al. (2002) do not consider this effect in their modifications to KPP from waves and Langmuir turbulence. Perhaps they assume there is a piece of the unresolved Eulerian velocity that exactly cancels the Stokes velocity, thus leaving no new unresolved term in the bulk Richardson number calculation.

- There are additional changes to the turbulent velocity scale, w_λ, that may arise from Langmuir turbulence. Questions arise regarding the precise calculation of the Langmuir number, the scaling added to the turbulence velocity scale, and the depth dependence of the Langmuir number.

Chapter 8

VERTICAL CONVECTIVE MIXING

Contents

The purpose of this chapter is to present the vertical convective mixing scheme available in CVMix. The following CVMix Fortran module is directly connected to the material in this chapter:

$$\texttt{cvmix\_convection.F90.}$$

8.1 Introduction to convective mixing

The hydrostatic approximation necessitates the use of a parameterization of vertical overturning processes. The original parameterization used by Bryan in the 1960's was motivated largely from ideas then used for modeling convection in stars (Bryan (1969)). Work by Marshall and collaborators (Klinger et al. (1996), **?**) have largely supported the basic ideas of vertical adjustment for purposes of large-scale ocean circulation.

The Cox (1984) implementation of convective adjustment (the "NCON" scheme) may leave columns unstable after completing the code's adjustment loop. Various full convective schemes have come online, with that from Rahmstorf (1993) implemented in MOM. An alternative to the traditional form of convective adjustment is to increase the vertical mixing coefficient to some large value (say $\geq 10\mathrm{m}^2\,\mathrm{s}^{-1}$) in order to quickly diffuse vertically unstable water columns. Indeed, it is this form recommended from the study of Klinger et al. (1996), and it is the approach commonly used in boundary layer schemes such as Pacanowski and Philander (1981) and Large et al. (1994). It is this vertical convective mixing approach that is supported in CVMix.

8.2 Time-implicit vertical mixing

An explicit treatment, especially with fine vertical grid resolution, places an unreasonable limitation on the size of the time step associated with vertical mixing processes. The use of fine vertical resolution with sophisticated mixed layer and/or neutral physics schemes has prompted the near universal time-implicit treatment of vertical mixing in ocean climate models.

Chapter 9

Diffusivity based on a chosen dissipation

Contents

The purpose of this chapter is to summarize a method that is not available in CVMix, yet which may be of interest to modellers using CVMix schemes. This method specifies vertical tracer diffusivities based on setting a floor to the power dissipation. This approach was found to be useful in the ESM2G earth system model documented by Dunne et al. (2012).

9.1 Power dissipation from vertical diffusion

Vertical tracer diffusion is associated with a dissipation of power. Assuming temperature and salinity have the same vertical diffusivities leads to the expression for power dissipation (W m^{-3})

$$
\begin{aligned}
\epsilon &= \rho \, \kappa \, N^2 \\
&= -\kappa \, g \left(\frac{\partial \rho}{\partial \theta} \frac{\partial \theta}{\partial z} + \frac{\partial \rho}{\partial S} \frac{\partial S}{\partial z} \right).
\end{aligned}
\tag{9.1}
$$

In these equations, κ is the vertical tracer diffusivity and g is the gravitational acceleration. When the temperature and salinity diffusivities differ, as occurs with double diffusion (Chapter 6), power dissipation is computed via

$$
\epsilon = -g \, \kappa_{\text{temp}} \left(\frac{\partial \rho}{\partial \theta} \frac{\partial \theta}{\partial z} \right) - g \, \kappa_{\text{salt}} \left(\frac{\partial \rho}{\partial S} \frac{\partial S}{\partial z} \right).
\tag{9.2}
$$

9.2 Setting a floor to the dissipation

We now compute a floor to the dissipation according to

$$
\epsilon_{\text{floor}} = \epsilon_{\text{min}} + B \, |N|,
\tag{9.3}
$$

where

$$
\epsilon_{\text{min}} \sim 10^{-6} \text{ W m}^{-3}
\tag{9.4}
$$

is a specified minimum power dissipation (set according to a namelist), B is another namelist parameter (physical dimensions J m^{-3}) further discussed below, and $|N|$ is the absolute value of the buoyancy frequency. As discussed below (see equation (9.9)), the $B|N|$ contribution to dissipation is motivated by the stratification dependent diffusivity proposed by Gargett (1984).

We establish a floor to the vertical diffusivity according to

$$
\begin{aligned}
\kappa_{\text{floor}} &= \frac{\epsilon_{\text{floor}} \, \Gamma^{\text{regularized}}}{\rho \, N^2} \\
&\approx \frac{\epsilon_{\text{floor}} \, \Gamma_o}{\rho_o \, (N^2 + \Omega^2)}.
\end{aligned}
\tag{9.5}
$$

In this equation,

$$
\Gamma^{\text{regularized}} = \Gamma_o \left(\frac{N^2}{N^2 + \Omega^2} \right)
\tag{9.6}
$$

is a regularized mixing efficiency introduced by **?**,

$$
\Gamma_o = 0.2
\tag{9.7}
$$

is a nominal value for stratified water where $N^2 >> \Omega^2$, and

$$
\Omega = 7.2921 \times 10^{-5} \text{s}^{-1}
\tag{9.8}
$$

is the angular rotation rate of the earth about its axis and around the sun (see also equation (5.15)). In the special case of $N^2 >> \Omega^2$, and $\epsilon_{\text{floor}} \approx B|N|$, then

$$
\kappa_{\text{floor}} \approx \left(\frac{\Gamma_o \, B}{\rho_o} \right) |N|^{-1}.
\tag{9.9}
$$

This scaling with respect to buoyancy frequency was suggested by Gargett (1984), where she recommended in open water to choose

$$
\frac{\Gamma_o \, B}{\rho_o} \approx 10^{-7} \text{ m}^2 \text{ s}^{-2},
\tag{9.10}
$$

so that

$$
B \approx 5 \times 10^{-4} \text{ J m}^{-3}.
\tag{9.11}
$$

This value may in fact be quite large, with the value $B \sim 1.5 \times 10^{-4}$ J m^{-3} used in the isopycnal model of Dunne et al. (2012).

When utilizing this method, the tracer diffusivity used for temperature, salinity, and passive tracers is set to be no smaller than κ_{floor}. The check should be made at the end of the vertical mixing processes for whether the diffusivity satisfies this constraint (see Figure 1.1). If too small, then diffusivity is increased to meet the constraint.

Bibliography

Adcroft, A., Hill, C., Marshall, J., 1999. A new treatment of the coriolis terms in c-grid models at both high and low resolutions. Monthly Weather Review 127, 1928–1936.

Axell, L., 2002. Wind-driven internal waves and Langmuir circulations in a numerical ocean model of the southern Baltic Sea. Journal of Geophysical Research 107, 107(C11), 3204, doi:10.1029/2001JC000922.

Belcher, S., Grant, A., Hanley, K., Fox-Kemper, B., Van Roekel, L., Sullivan, P., Large, W., Brown, A., Hines, A., Calvert, D., Rutgersson, A., Petterson, H., Bidlot, J., Janssen, P., Polton, J. A., 2012. A global perspective on Langmuir turbulence in the ocean surface boundary layer. Geophysical Research Letters 39-L18605, doi:10.1029/2012GL052932.

Bryan, K., 1969. A numerical method for the study of the circulation of the world ocean. Journal of Computational Physics 4, 347–376.

Bryan, K., Lewis, L. J., 1979. A water mass model of the world ocean. Journal of Geophysical Research 84, 2503–2517.

Chang, Y. S., Xu, X., Özgökmen, T. M., Chassignet, E. P., Peters, H., Fischer, P. F., 2005. Comparison of gravity current mixing parameterizations and calibration using a high-resolution 3d nonhydrostatic spectral element model. Ocean Modelling 3-4, 342–368.

Cox, M. D., 1984. A Primitive Equation, 3-Dimensional Model of the Ocean. NOAA/Geophysical Fluid Dynamics Laboratory, Princeton, USA.

Craig, P., Banner, M., 1994. Modeling wave-enhanced turbulence in the surface ocean layer. Journal of Physical Oceanography 24, 2546–2559.

Dunne, J. P., John, J. G., Hallberg, R. W., Griffies, S. M., Shevliakova, E. N., Stouffer, R. J., Krasting, J. P., Sentman, L. A., Milly, P. C. D., Malyshev, S. L., Adcroft, A. J., Cooke, W., Dunne, K. A., Harrison, M. J., Levy, H., Samuels, B. L., Spelman, M., Winton, M., Wittenberg, A. T., Phillips, P. J., Zadeh, N., 2012. GFDLs ESM2 global coupled climate-carbon Earth System Models Part I: Physical formulation and baseline simulation characteristics. Journal of Climate 25, 6646–6665.

Durski, S. M., Glenn, S. M., Haidvogel, D. B., 2004. Vertical mixing schemes in the coastal ocean: Comparison of the level 2.5 Mellor-Yamada scheme with an enhanced version of the K profile parameterization. Journal of Geophysical Research 109, doi:10.1029/2002JC001702.

Fairall, C., Bradley, E., Godfrey, J., Wick, G., Edson, J., Young, G., 1996. Cool-skin and warm-layer effects on sea surface temperature. Journal of Geophysical Research 101, 1295–1308.

Gargett, A. E., 1984. Vertical eddy diffusivity in the ocean interior. Journal of Marine Research 42, 359–393.

Gent, P., Bryan, F., Danabasoglu, G., Doney, S., Holland, W., Large, W., McWilliams, J., 1998. The NCAR climate system model global ocean component 11, 1287–1306.

Gill, A., 1982. Atmosphere-Ocean Dynamics. Vol. 30 of International Geophysics Series. Academic Press, London, 662 + xv pp.

Goosens, M., Mittelbach, F., Samarin, A., 1994. The LATEXCompanion. Addison-Wesley, Reading, Massachusetts, 528 pp.

Gregg, M., Sanford, T., Winkel, D., 2003. Reduced mixing from the breaking of internal waves in equatorial waters. Nature 422, 513–515.

Griffies, S. M., 2004. Fundamentals of Ocean Climate Models. Princeton University Press, Princeton, USA, 518+xxxiv pages.

Griffies, S. M., Biastoch, A., Böning, C. W., Bryan, F., Danabasoglu, G., Chassignet, E., England, M. H., Gerdes, R., Haak, H., Hallberg, R. W., Hazeleger, W., Jungclaus, J., Large, W. G., Madec, G., Pirani, A., Samuels, B. L., Scheinert, M., Gupta, A. S., Severijns, C. A., Simmons, H. L., Treguier, A. M., Winton, M., Yeager, S., Yin, J., 2009. Coordinated Ocean-ice Reference Experiments (COREs). Ocean Modelling 26, 1–46.

Griffies, S. M., Gnanadesikan, A., Dixon, K. W., Dunne, J. P., Gerdes, R., Harrison, M. J., Rosati, A., Russell, J., Samuels, B. L., Spelman, M. J., Winton, M., Zhang, R., 2005. Formulation of an ocean model for global climate simulations. Ocean Science 1, 45–79.

Griffies, S. M., Pacanowski, R., Schmidt, M., Balaji, V., 2001. Tracer conservation with an explicit free surface method for z-coordinate ocean models. Monthly Weather Review 129, 1081–1098.

Henyey, F., Wright, J., Flatte, S. M., 1986. Energy and action flow through the internal wave field: an eikonal approach. Journal of Geophysical Research 91, 8487–8496.

Holland, W., Chow, J., Bryan, F., 1998. Application of a third-order upwind scheme in the NCAR ocean model. Journal of Climate 11, 1487–1493.

Huang, R. X., 1993. Real freshwater flux as a natural boundary condition for the salinity balance and thermohaline circulation forced by evaporation and precipitation. Journal of Physical Oceanography 23, 2428–2446.

IOC, SCOR, IAPSO, 2010. The international thermodynamic equation of seawater-2010: calculation and use of thermodynamic properties. Intergovernmental Oceanographic Commission, Manuals and Guides No. 56, UNESCO, available from http://www.TEOS-10.org, 196pp.

Ivey, G., Imberger, J., 1991. On the nature of turbulence in a stratified fluid. Part I: The energetics of mixing. Journal of Physical Oceanography 25, 650–658.

Jackson, L., Hallberg, R., Legg, S., 2008. A parameterization of shear-driven turbulence for ocean climate models. Journal of Physical Oceanography 38, 1033–1053.

Jayne, S., 2009. The impact of abyssal mixing parameterizations in an ocean general circulation model. Journal of Physical Oceanography 39, 1756–1775.

Jayne, S., St.Laurent, L. C., 2001. Parameterizing tidal dissipation over rough topography. Geophysical Research Letters 28, 811–814.

Jochum, M., 2009. Impact of latitudinal variations in vertical diffusivity on climate simulations. Journal of Geophysical Research 114 C01010, doi:10.1029/2008JC005030.

Kantha, L. H., Clayson, C. A., 2000. Small Scale Processes in Geophysical Fluid Flows. Academic Press, New York, USA, 883 pp.

Killworth, P. D., Stainforth, D., Webb, D. J., Paterson, S. M., 1991. The development of a free-surface Bryan-Cox-Semtner ocean model. Journal of Physical Oceanography 21, 1333–1348.

Klinger, B. A., Marshall, J., Send, U., 1996. Representation of convective plumes by vertical adjustment. Journal of Geophysical Research 101, 18175–18182.

Klymak, J., Moum, J., Nash, J., Kunze, E., Girton, J., Carter, G., Lee, C., Sanford, T., Gregg, M., 2005. An estimate of tidal energy lost to turbulence at the hawaiian ridge. Journal of Physical Oceanography submitted.

Lamport, L., 1994. LaTeX: A Documentation Preparation System User's Guide and Reference Manual. Addison-Wesley, Reading, Massachusetts, 272 pp.

Large, W., 1998. Modeling the oceanic boundary layer. In: Chassignet, E. P., Verron, J. (Eds.), Ocean Modeling and Parameterization. Vol. 516 of NATO ASI Mathematical and Physical Sciences Series. Kluwer, pp. 81–120.

Large, W., Gent, P., 1999. Validation of vertical mixing in an equatorial ocean model using large eddy simulations and observations. Journal of Physical Oceanography 29, 449–464.

Large, W., McWilliams, J., Doney, S., 1994. Oceanic vertical mixing: a review and a model with a nonlocal boundary layer parameterization. Reviews of Geophysics 32, 363–403.

Large, W. G., 2012. An ocean climate modeling perspective on buoyancy-driven flows. In: Chassignet, E. P., Cenedese, C., Verron, J. (Eds.), Buoyancy-driven flows. Cambrideg, pp. 240–280.

Large, W. G., Danabasoglu, G., Doney, S. C., McWilliams, J. C., 1997. Sensitivity to surface forcing and boundary layer mixing in a global ocean model: annual-mean climatology. Journal of Physical Oceanography 27, 2418–2447.

Large, W. G., Yeager, S., 2009. The global climatology of an interannually varying air-sea flux data set. Climate Dynamics 33, 341–364.

Laurent, L. C. S., Schmitt, R., 1999. The contribution of salt fingers to vertical mixing in the north atlantic tracer release experiment. Journal of Physical Oceanography 29, 1404–1424.

Ledwell, J. R., Watson, A. J., Law, C. S., 1993. Evidence for slow mixing across the pycnocline from an open-ocean tracer-release experiment. Nature 364, 701–703.

Legg, S., Hallberg, R., Girton, J., 2006. Comparison of entrainment in overflows simulated by z-coordinate, isopycnal and non-hydrostatic models. Ocean Modelling 11, 69–97.

Lemarié, F., Kurian, J., Shchepetkin, A. F., Molemaker, M. J., Colas, F., McWilliams, J. C., 2012. Are there inescapable issues prohibiting the use of terrain-following coordinates in climate models? Ocean Modelling 42, 57–79.

Li, M., Garrett, C., 1993. Cell merging and the jet/downwelling ratio in Langmuir circulation. Journal of Marine Research 51, 737–769.

Li, X., Chao, Y., McWilliams, J. C., Fu, L. L., 2001. A comparison of two vertical-mixing schemes in a Pacific ocean general circulation model. Journal of Climate 14, 1377–1398.

McDougall, T. J., 1987. Neutral surfaces. Journal of Physical Oceanography 17, 1950–1967.

McDougall, T. J., 2003. Potential enthalpy: a conservative oceanic variable for evaluating heat content and heat fluxes. Journal of Physical Oceanography 33, 945–963.

McWilliams, J. C., Sullivan, P., 2001. Vertical mixing by Langmuir circulations. Spill Science and Technology Bulletin 6, 225–237.

McWilliams, J. C., Sullivan, P., Moeng, C.-H., 1997a. Langmuir turbulence in the ocean. Journal of Fluid Mechanics 334, 1–30.

McWilliams, J. C., Sullivan, P., Moeng, C.-H., 1997b. Langmuir turbulence in the ocean. Journal of Fluid Mechanics 334, 1–30.

Melet, A., Hallberg, R., Legg, S., Polzin, K., 2013. Sensitivity of the Pacific Ocean state to the vertical distribution of internal-tide driven mixing. Journal of Physical Oceanography, doi:10.1175/JPO–D–12–055.1.

Mellor, G. L., Yamada, T., 1982. Development of a turbulent closure model for geophysical fluid problems. Reviews of Geophysics 20, 851–875.

Mesinger, F., 1973. A method for construction of second-order accurate difference schemes permitting no false two-grid-interval waves in the height field. Tellus 25, 444–457.

Miles, J., 1961. On the stability of heterogeneous shear flows. Journal of Fluid Mechanics 10, 496–508.

Moum, J., Caldwell, D., Nash, J., Gunderson, G., 2002. Observations of boundary mixing over the continental slope. Journal of Physical Oceanography 32, 2113–2130.

Munk, W., Wunsch, C., 1998. Abyssal recipes II: Energetics of tidal and wind mixing. Deep-Sea Research 45, 1977–2010.

Osborn, T. R., 1980. Estimates of the local rate of vertical diffusion from dissipation measurements. Journal of Physical Oceanography 10, 83–89.

Pacanowski, R. C., Griffies, S. M., 1999. The MOM3 Manual. NOAA/Geophysical Fluid Dynamics Laboratory, Princeton, USA, 680 pp.

Pacanowski, R. C., Philander, G., 1981. Parameterization of vertical mixing in numerical models of the tropical ocean. Journal of Physical Oceanography 11, 1442–1451.

Polzin, K., 2009. An abyssal recipe. Ocean Modelling 30, 298–309.

Polzin, K. L., 2004. Idealized solutions for the energy balance of the finescale internal wave field. Journal of Physical Oceanography 34, 231–246.

Polzin, K. L., Toole, J. M., Ledwell, J. R., Schmitt, R. W., 1997. Spatial variability of turbulent mixing in the abyssal ocean. Science 276, 93–96.

Rahmstorf, S., 1993. A fast and complete convection scheme for ocean models. Ocean Modelling 101, 9–11.

Rascle, N., Ardhuin, F., Terray, F., 2006. Drift and mixing under the ocean surface: a coherent one-dimensional description with application to unstratified conditions. Journal of Geophysical Research 111: C03016.

Schmitt, R. W., 1994. Double diffusion in oceanography. Annual Review of Fluid Mechanics 26, 255–285.

Shchepetkin, A. F., 2005. If-less kpp. ROMS/TOMS Workshop: Adjoint Modeling and Applications.

Simmons, H. L., Jayne, S. R., St.Laurent, L. C., Weaver, A. J., 2004. Tidally driven mixing in a numerical model of the ocean general circulation. Ocean Modelling 6, 245–263.

Smyth, G. C. W. D., Skyllingstad, E. D., Wijesekera, H., 2002. Nonlocal fluxes and Stokes drift effects in the K-profile parameterization. Ocean Dynamics 52, 104–115.

St.Laurent, L. C., Simmons, H., Jayne, S., 2002. Estimating tidally driven energy in the deep ocean. Geophysical Research Letters 29, 2106–2110.

St.Laurent, L. C., Stringer, S., Garrett, C., Perrault-Joncas, D., 2003. The generation of internal tides at abrupt topography. Deep-Sea Research 50, 987–1003.

St.Laurent, L. C., Toole, J., Schmitt, R., 2001. Buoyancy forcing by turbulence above rough topography in the abyssal brazil basin. Journal of Physical Oceanography 31, 3476–3495.

Sullivan, P. P., McWilliams, J. C., 2010. Dynamics of winds and currents coupled to surface waves. Annual Review of Fluid Mechanics 42, 19–42.

Sullivan, P. P., McWilliams, J. C., Melville, W. K., 2007. Surface gravity wave effects in the oceanic boundary layer: large-eddy simulation with vortex force and stochastic breakers. Journal of Fluid Mechanics 593, 405–452.

Tennekes, H., 1973. The logarithmic wind profile. Journal of Atmospheric Sciences 30, 558–567.

Terray, E., Donelan, M., Agrawal, Y., Drennan, W., Kahma, K., Williams, A., Hwang, P., Kitaigorodskii, S., 1996. Estimates of kinetic energy dissipation under breaking waves. Journal of Physical Oceanography 26, 792–807.

Troen, I. B., Mahrt, L., 1986. A simple model of the atmospheric boundary layer: sensitivity to surface evaporation. Boundary Layer Meteorology 37, 129–148.

Umlauf, L., Burchard, H., Bolding, K., 2005. GOTM: source code and test case documentation: version 3.2. 231pp.

Webb, D. J., Coward, A. C., de Cuevas, B. A., Gwilliam, C. S., 1998. The first main run of the OCCAM global ocean model. Internal Document No. 34. Southampton Oceanography Centre, Southampton, England.

Index